Dynamic Modelling and Stability Controller Development for Articulated Steer Vehicles

by

Nasser Lashgarian Azad

A thesis

presented to the University of Waterloo

in fulfillment of the

thesis requirement for the degree of

Doctor of Philosophy

in

Mechanical Engineering

Waterloo, Ontario, Canada 2006

I hereby declare that I am the sole author of this thesis. This is a true copy of the thesis, including any required final revisions, as accepted by my examiners.

I understand that my thesis may be made electronically available to the public.

Abstract

In this study, various stability control systems are developed to remove the lateral instability of a conventional articulated steer vehicle (ASV) during the oscillatory yaw motion or "snaking mode". First, to identify the nature of the instability, some analyses are performed using several simplified models. These investigations are mainly focused on analyzing the effects of forward speed and of two main subsystems of the vehicle, the steering system and tires, on the stability. The basic insights into the stability behavior of the vehicle obtained from the stability analyses of the simplified models are verified by conducting some simulations with a virtual prototype of the vehicle in ADAMS.

To determine the most critical operating condition with regard to the lateral stability and to identify the effects of vehicle parameters on the stability, various studies are performed by introducing some modifications to the simplified models. Based on these studies, the disturbed straight-line on-highway motion with constant forward speed is recognized as the most critical driving condition. Also, the examinations show that when the vehicle is traveling with differentials locked, the vehicle is less prone to the instability. The examinations show that when the vehicle is carrying a rear-mounted load having interaction with ground, the instability may happen if the vehicle moves on a relatively good off-road surface. Again, the results gained from the analyses related to the effects of the vehicle parameters and operating conditions on the stability are verified using simulations in ADAMS by making some changes in the virtual prototype for any case.

To stabilize the vehicle during its most critical driving condition, some studies are directed to indicate the shortcomings of passive methods. Alternative solutions, including design of different types of stability control systems, are proposed to generate a stabilizing yaw moment. The proposed solutions include an active steering system with a classical controller, an active torque vectoring device with a robust full state feedback controller, and a differential braking system with a robust variable structure controller. The robust controllers are designed by using simplified models, which are also used to evaluate the ability to deal with the uncertainties of the vehicle parameters and its variable operating conditions. These controllers are also incorporated into the virtual prototype, and their capabilities to stabilize the vehicle in different operating conditions and while traveling on different surfaces during the snaking mode are shown.

Acknowledgements

In the name of God, Most Gracious, Most Merciful

I would like to take this opportunity to express my deep gratitude and appreciation to those people who have helped me to complete my PhD program, and to individuals to whom I am very much indebted and who, without their support, this achievement would not have been possible. First of all, special thanks to my supervisors, Professor Amir Khajepour and Professor John McPhee for their great guidance, advice and encouragement. Also, I wish to express my thanks for the thoughtful review and many helpful suggestions of Dr. Esmailzadeh as the external examiner. I would like to thank the reading committee members, Dr. Jan Huissoon, Dr. Steve Lambert and Dr. Krzysztof Czarnecki for their valuable comments and suggestions. Thanks go to all of my colleagues at the University of Waterloo who have contributed to make it such an enjoyable place to work. Moreover, the financial support of this work by the Auto21 Network of Centres of Excellence, Materials and Manufacturing Ontario (MMO) and Timberjack (a John Deere company) is gratefully acknowledged.

Many thanks to my friends with whom I have shared so much fun and so many good times over the past few years in the Kitchener-Waterloo region. Although I cannot mention them all by name, I am grateful to all of them and wish them the best. Many thanks to all the members of my family for the warmth and kindness they always offer, with special gratitude to my dearest wife, Nasim. Without her continuous support, encouragement and love, my study would have never been done properly. Finally, my greatest appreciations and thanks are dedicated to my parents from whom I have taken the lesson of life. I am very proud of them.

Contents

List of Tables

List of Figures

Nomenclature

α_2 Average of left and right tire slip angles at rear axle

c Distance from articulation point to rear body center of mass

k_t Vertical stiffness of tire

m_w Wheel mass

α Tire slip angle

α_1 Average of left and right tire slip angles at front axle

β_e Effective bulk modulus

δ_t Tire vertical deflection

δW_l Virtual work done by tire tractive forces on ψ and θ

δW_S Virtual work by steering torque

γ Wheel camber

$\hat{P}_L$ Dimensionless pressure difference

λ Eigenvalue of system

μ Friction coefficient

$\mu_{\max}$ Maximum friction coefficient

μ_s Sliding friction coefficient when longitudinal slip is 100 percent

Φ Boundary layer thickness

ϕ Articulation angle

ψ Front body yaw angle

$\mathbf{A}$ System matrix

$\mathbf{B}$ Input matrix

$\mathbf{K}$ Feedback matrix

$\mathbf{q}$ Generalized coordinates

$\mathbf{X}$ State variables

θ Rear body yaw angle

θ_f Spin rotation angle of front wheels

θ_i Wheel rotation angle

θ_r Spin rotation angle of rear wheels

ϖ Wheel angular velocity

$\varpi_\circ$ Free rolling wheel angular velocity

ξ Damping ratio

a Distance from front body center of mass to front wheels

b Distance from articulation point to front body center of mass

b_t Tire width

$C_{\alpha\,\mathrm{max}}$ Off-road tire model coefficient for lateral force

C_α Tire lateral force coefficient

$C_{F\alpha}$ Tire cornering stiffness

C_{Fs} Tire longitudinal slip stiffness

C_g Torsional damping at grapple joint

C_I Cone index

C_l Tire contact length coefficient

$C_{M\alpha}$ Tire aligning moment coefficient

C_{rr} Coefficient of tire rolling resistance

C_R Equivalent torsional damping at articulation joint

$C_{s\,\text{max}}$ Off-road tire model coefficient for longitudinal force

C_{sf} Longitudinal slip stiffness of front tires

C_{sr} Longitudinal slip stiffness of rear tires

C_s Tire longitudinal force coefficient

$C_{T\alpha}$ Tire aligning stiffness

C_{tp} Valve leakage coefficient

c_t Vertical damping coefficient of tire

d Distance from rear wheels to rear body center of mass

d_j Perpendicular distance from articulation point to steering cylinder

d_p Piston diameter

d_r Rod diameter

d_t Tire overall diameter

e Distance from grapple joint to rear wheels

f Distance from grapple joint to log center of mass

F_{fx} Longitudinal contact force on log

F_{fy} Lateral contact force on log

F_l Longitudinal contact force on log

F_r Tire rolling resistance force

F_{t1} Resultant tractive force at front

F_x Tire longitudinal force

F_{y1} Resultant lateral force at front axle

F_{y2} Resultant lateral force at rear axle

F_y Lateral tire force

F_{ZT} Rated tire load

F_z Tire normal force

h Distance from log center of mass to log contact point

H_g Height of grapple lateral axis joint above ground

h_t Tire section height

I_1 Front part yaw moment of inertia

I_2 Rear part yaw moment of inertia

I_3 Log yaw moment of inertia

k_1 Off-road tire model coefficient

k_2 Off-road tire model coefficient

K_{cr} Critical torsional stiffness

K_c Valve flow-pressure coefficient

K_R Equivalent torsional stiffness of hydraulic cylinders

K_S Equivalent torsional stiffness of steering system

L Lyapunov function

l_r Tire relaxation length

l_t Tire contact length

m_1 Front part mass

m_2 Rear part mass

m_3 Log mass

M_x Tire overturning moment

M_y Tire rolling resistance moment

M_{z1} Resultant aligning moment at front axle

M_{z2} Resultant self-aligning moment at rear axle

M_z Tire self-aligning moment

MOB Tire mobility number

N_1 Vertical load at front axle

N_2 Vertical load at rear axle

N_3 Vertical contact force on log

P Vertical reaction force at grapple lateral axis joint

P_1 Pressure of forward chamber

P_2 Pressure of return chamber

P_L Cylinder pressure difference

Q Longitudinal reaction force at grapple lateral axis joint

R Dissipation function

r_e Tire effective rolling radius

S*   Modified definition of wheel longitudinal slip

T_1 Kinetic energy of front body

T_2 Kinetic energy of rear body

T_3 Kinetic energy of log

T_d Wheel driving torque

t_p Pneumatic trail

T_R Resistant torque at articulation joint

T_S Steering system torque

u vehicle forward speed

u_{cr} Critical speed

v Front body lateral velocity

V_1 Fluid volume of chamber with increasing volume

V_2 Fluid volume of chamber with decreasing volume

$V_\circ$ Free rolling wheel angular velocity

V_{cx} Velocity of tire contact patch in x direction

V_{cy} Velocity of tire contact patch in y direction

V_x Wheel center velocity in x direction

w_t Wheel track

S   Wheel longitudinal slip according to SAE definition

Chapter 1

Introduction

Both maneuverability and traction of off-road vehicles are important for better performance in applications on unprepared, unpredictable and changing terrains. However, the combination of these two important features is technically difficult because high traction requires driving effort on the front wheels in addition to the rear wheels, as well as large tires, which limit the steer angles, and thus the maneuverability, of front wheel steer vehicles. For this reason, various steering layouts for off-road vehicles have been designed. Typical off-road vehicle steering layouts are illustrated in Figure 1-1. Types 1, 2, 3, and 5 are most commonly used, type 4 is less common and is sometimes adopted for earth-moving and agricultural vehicles. Type 6 is a combination of types 4 and 5 and may be used for farm transportation and load carrying purposes. Type 7, skid-steer system, has been introduced for enabling off-road vehicles to maneuver effectively in confined spaces. In this design, all of the wheels are non-steerable, and those on one side turn together independently of those on the opposite side. If all of the wheels on both sides are driven forward with the same speed, the vehicle moves forward, but if the two wheels on one side are driven in the opposite direction, the vehicle will turn on itself.

The low speed turning behavior (with a constant angle and without considering tire side slip) of off-road vehicles with the steering layouts of type 1 to 6 has been compared in [1]. The single steered axle layouts (types 1 and 2) create four wheel trajectories, but types 3, 4 and 5 result in superior tracking where the rear wheels follow the exact trajectory of the front wheels. Also, type 6 can be designed, in a complicated way, for perfect tracking if the ratio between the body and axle steer angles is appropriate. Perfect tracking can increase the traction force that
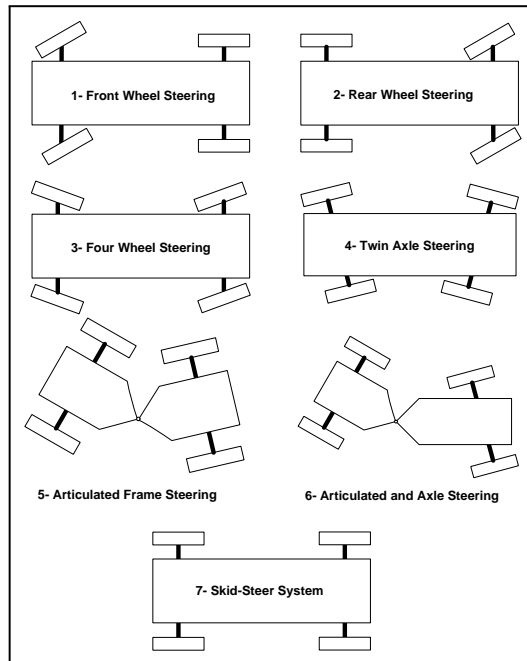
Figure 1-1: Typical steering layouts of off-road vehicles.

is available from the rear tire and removes the need for a longitudinal differential in four-wheel drive vehicles, as the front and rear wheels travel at the same speed. This will also reduce driving resistance forces, and thus, decrease the tire wear.

Type 3 includes twice as many moving parts in the axles as those in types 1 and 2, resulting in high manufacturing and servicing costs. Therefore, for both technical and economical reasons, type 5, articulated frame steering, has become popular and an increasing number of manufacturers choose this simple but efficient steering system. Articulated frame steering is a type of powered steering system by which the relative yaw angle of two parts of the vehicle is changed, usually by two hydraulic actuators. The introduction of articulated frame steering was a landmark in the development of off-road vehicles, especially for loading and earth-moving applications. This design significantly improved the level of maneuverability and turning abilities of off-road vehicles, which led to more efficient performance. The concept of articulated frame steering was first proposed in the early 20th century by a number of manufacturers [2], such as Pavesi-Toloti (Italy), Pavesi-Wilson (England), Leturno (France), Krupp (Germany), and Lockheed (USA). However, for many years, this idea was not commonly used. It was not

until the development of drive systems, such as hydraulic systems, that the applications of articulated frame steering were increased.

Articulated steer vehicles (ASVs) with articulated frame steering layout, such as scrapers, loaders and forestry skidders, fall into the category of articulated vehicles with two separate and rigid segments. In general, articulated vehicles are defined as vehicles with two or more sections joined together (multiple-units), while each section may have one or more axles. Also, each axle can be equipped with single or dual tires on the left and right sides. An articulated vehicle, for instance a tractor-trailer combination, can be designed with different steering layouts. However, to take full advantage of the articulation principle, articulated vehicles are equipped with articulated frame steering layout, and become ASVs. Owing to their specific steering layout, ASVs have great maneuverability in confined areas. The operator can even make steering corrections in stationary conditions. In addition, the steering layout of ASVs results in a larger wheelbase, which gives the advantage of less pitch motion on rough surfaces. ASVs usually have large, wide tires, which provide remarkable mobility even during travel on rough terrain (i.e. due to reduced ground pressure and minimum sinking into soft ground). For this reason, ASVs are utilized on rough surfaces and muddy terrains, where a single frame vehicle can lose traction and become bogged down.

Mostly, ASVs have rigid suspension systems, and dynamic loads from the ground on the cab are damped by their flexible tires and a spring-mounted operator seat. Currently, the use of suspension systems on ASVs to enhance driver comfort has been considered by some manufacturers. In an ASV, a torque converter may be placed between the engine and drive wheels to prevent the engine from going into a stall, although some ASVs have a direct drive design in which the engine is coupled directly to the transmission. ASVs generally have a permanent four-wheel drive configuration. This drive configuration permits traveling on various surfaces, even muddy ground conditions. The front and rear axles have transverse differential gears to transfer power to the left and right wheels that can be locked. A longitudinal differential may also be used between front and rear axles, which can be locked during travel on soft or icy surfaces by a differential lock. In some ASVs (typically for load-carrying applications), the front and rear axles can be also decoupled to transfer power to one of the axles. In these vehicles, the drive configuration can be selected during motion by the operator.

In the most commonly used ASVs (conventional ASVs), the articulation joint is placed near the centre of the wheelbase. However, for ASVs with a rear load-carrying platform, the halfway located joint is not suitable because it divides the loading area. Therefore, for load-carrying ASVs, the articulation joint is located near the front axle. To keep constant ground contact on all wheels during travel on different terrains, a joint is added to allow rolling of one of the axles relative to its frame (pendulum axle). In general, the axle with the smaller load will be the pinned axle (rear or front). Typically, the roll freedom is $\pm15°$, whereas the yaw articulation angles are $\pm45°$. ASVs include considerably larger inertias than wheel steer vehicles, and these must be displaced during the steering process; therefore, ASVs generally have a higher power requirement for the steering process. Typically, ASVs require 3.5 times as much as energy as a similar wheel steer vehicle for an equivalent lock-to-lock turn [3].

Despite the above-mentioned advantages, the articulated frame steering layout introduces some problems to ASVs, including both roll and lateral instabilities in different situations. To obtain a preliminary insight into these problems, the previous work on the roll and lateral stability of ASVs is reviewed in the following sections.

1.1 Research Literature on Stability of ASVs

In articulated vehicles, the front and rear sections affect one another due to the inner forces at the articulation joints. Therefore, the stability analysis of these vehicles is much more complex than that of single frame vehicles. Based on practical reports, both roll instability at low speeds and lateral instability at high speeds can occur for ASVs. Roll instability is related to the possibility that the vehicle will roll over. Lateral stability requires that the vehicle remains in a state of equilibrium when it is subjected to a small disturbance, such as small movements of the steering wheel by the operator. The disturbing factor causes a perturbation of the vehicle lateral or yaw motion, and as a result, the vehicle may become unstable.

1.1.1 Roll Stability

During operation on inclined grounds and banked roads at low speeds, an ASV typically has a lower roll stability than that of a single frame vehicle [4]. This is the case as the vehicle
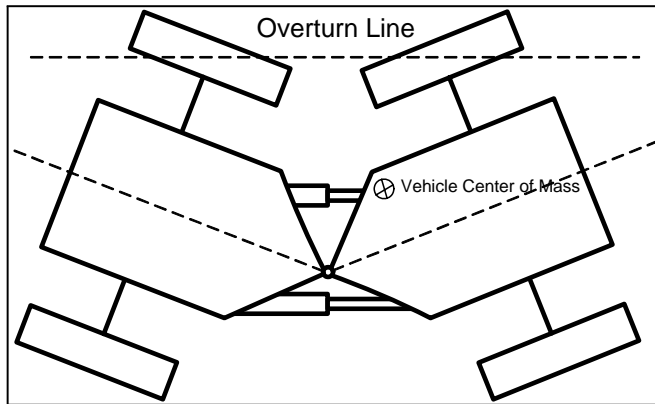
Figure 1-2: Center of mass position for an ASV during the vehicle turning.

center of gravity moves towards the line of overturn when the articulation angle increases [5], as shown in Figure 1-2. Gibson et al. [4, 6] investigated tipping of four-wheel drive logging machines (articulated steer skidders and forwarders) with a pinned front axle during operation on inclined grounds at low speeds. In this study, they defined a stability triangle for the vehicle by using three supporting points (i.e. rear tires' contact points and front axle pin). The tipping begins when the weight vector of the vehicle intersects the line forming a side of the defined stability triangle. Based on this criterion, for any given articulation angle and orientation of the vehicle on the slope, they computed the slope angle at which tipping occurs. They also determined the minimum stability point (i.e. the lowest slope when tipping occurs) for a given articulation angle. They also compared their results with those from the tipping tests of a scale model of the vehicle. Gibson et al. later developed an early warning device for the vehicle based on their previous studies [7]. To develop this device, they also took into account the pulling effects of the load on the tipping, for instance, a rear-mounted log for skidders. Some sensors (i.e. load cells) were used to send the information about the resultant tipping forces applied to the vehicle by the load to the warning device. This information was utilized to modify the shape of the stability triangle of the vehicle, and load-correction computations.

In addition, Wray et al. [8] developed two different types of early warning devices for a specific type of ASVs, a front-end loader. The first device was developed based on the concept of the stability triangle by including the effects of some factors, such as the vehicle pitch

angle and load. The inputs from five sensors were used to calculate the angle at which the vehicle would roll over. The difference between the resulting angle and the actual roll angle was indicated by a voltage that was sensed by four level detectors. Each level detector was connected to one of the four indicator lights with different colors (one green, two amber, and one red). This system was installed on three vehicles in a rock quarry operation during a 12-month test period, and was recognized as very useful by the operators of the vehicles. To build a simpler and cheaper system, they designed a second device based on sensing the normal load on wheels to trigger the system. They utilized some strain gauges to determine the bending stress on the axles, and this information was used to measure the wheel normal load by canceling out the effects due to the tire side force. This system consisted of a simpler electronic package, and the required computational operations were reduced. Inertia effects (i.e. acceleration, deceleration and centripetal forces) were also considered by incorporating a differentiator circuit into the system. The field testing of this system was also positive [8].

1.1.2 Lateral Stability

The effects of higher speeds on the lateral stability of ASVs are more remarkable than those for wheel steer vehicles, which produces one of the main disadvantages of ASVs: the lateral instability while driving straight at higher speeds. During travel on roads at high speeds, two types of lateral instability are possible: a diverging mode in which the front section of the vehicle tends to fold around the rear section [9], and a weaving mode in which the two sections of the vehicle oscillate, relative to each other at a frequency of approximately 1 Hz [10]. These two modes are similar to the classic jackknifing and snaking instabilities of wheel steer articulated vehicles, such as tractor-semitrailers and car-caravan combinations, which are explained briefly. For tractor-semitrailers, there are two common modes of jackknifing, as shown schematically in Figure 1-3. The first mode is a tractor jackknife and occurs when the trailer is stable on the road, but the tractor turns around the articulation joint in a highly unstable manner. The second is a trailer swing and is the reverse phenomenon; the tractor remains stable and the semitrailer can no longer be controlled around the articulation joint. For ASVs, jackknifing usually occurs in load-carrying vehicles, for instance dumpers, with an articulation joint near the front axle, especially when the vehicle is fully loaded [11]. This problem typically occurs
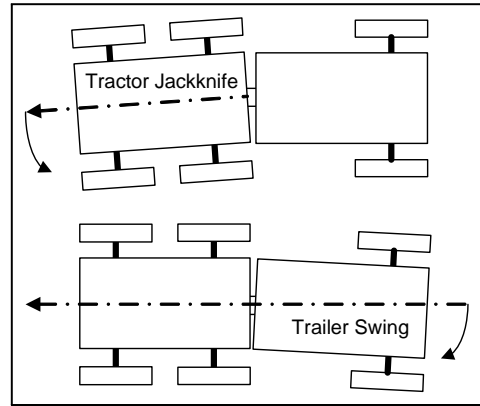
Figure 1-3: A schematic of jackknifing modes for tractor-semitrailers.

when the steering wheel is turned by the driver, but the rear part of the vehicle keeps traveling straight, which may lead to a complete failure of the hydraulic cylinders.

The most common problem encountered in the use of a car-caravan combination is oscillatory yaw motion [12], or snaking, shown schematically in Figure 1-4. This undesirable behavior is generated at moderate to high road speeds [13]. The oscillations occur at a typical frequency of 0.6 Hz, and become stronger as the speed or the trailer to car mass ratio increases. The result is a considerable number of loss-of-control accidents. New trends in the automotive industry, such as weight reduction in cars and equipment installation in caravans, can intensify snaking due to a greater caravan to car mass ratio. The most commonly used anti-snaking device is the operator-adjustable friction damper at the connection joint. The operator can arbitrarily preload friction material pads within the joint. However, it is possible for the operator to choose a friction level that is sufficient to stabilize low amplitude oscillations but insufficient to stabilize high amplitude oscillations. As a result, the combination can become unstable following a small perturbation. Therefore, new alternatives, such as a caravan active braking system to reduce the snaking motions, have been proposed [14, 15].

For the most widely used design of ASVs, with the articulation joint at the halfway point of the vehicle, a similar problem is common. During on-highway travel in a straight line at higher speeds, the two segments of the vehicle oscillate with different phases relative to each other, as shown schematically in Figure 1-5. "The problems are expressed qualitatively by drivers as
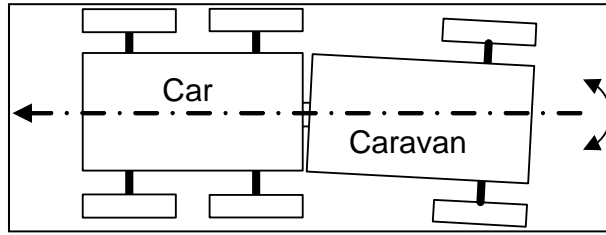
Figure 1-4: A schematic of snaking mode for car-caravan systems.
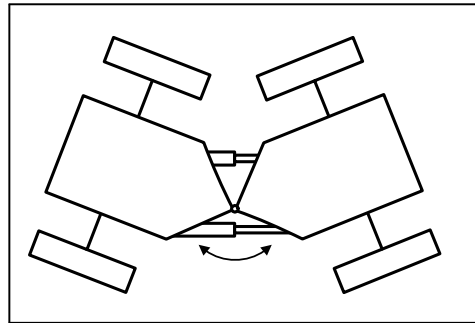
Figure 1-5: A schematic of snaking mode for conventional ASVs.

weaving, wandering or snaking" [10].

Crolla and Horton [3] first investigated the lateral stability of an ASV traveling in a straight line at a constant forward speed, based on the results from a planar linearized three degrees of freedom (DOF) model. They used a torsional spring and damper at the articulation joint to represent the hydraulic cylinders between the front and rear parts. The authors identified two common lateral stability problems related to this type of vehicle at higher speeds, the diverging and weaving instabilities. During the diverging instability, or jackknifing, the front part of the vehicle folds around the rear part. During the weaving instability, or snaking, the two parts of the vehicle oscillate relative to each other, typically at a frequency of 1 Hz. Their investigations showed that these modes may occur when there is a low value of effective torsional stiffness at the joint. An amount of entrapped air and flexible pipes in the hydraulic system are the factors that can result in low stiffness at the articulation joint. In addition, the important effect of the center of mass position of the rear part of the ASV on the type of unstable mode was revealed by their work. An undesirable oscillatory mode, or snaking, takes place when the center of

8

mass of the rear part is placed behind the rear axle; however, if it is placed in front of the rear axle, only diverging instability or jackknifing is possible. Crolla and Horton's results were qualitatively similar to the problems reported by the different manufacturers.

Later, these authors published their numerical results, based on a model that consisted of the vehicle model and the hydraulic steering system model [10]. The combined model was generated from their previous 3-DOF model, with the inclusion of the normalized equations of the steering valve and hydraulic cylinder. The characteristics of the steering system were identified to be the most sensitive design features for the lateral stability of the vehicle. In addition to the two types of instabilities discussed previously, which occur when there is low torsional stiffness at the joint, a third type of instability was also identified; a slowly diverging mode similar to the oversteer mode of a single frame vehicle. The corrective attempts of the steering system to return the vehicle to its nominal path during this mode results in a low frequency weaving mode. Most importantly, their work showed that introduction of leakage across the hydraulic cylinders can be utilized to stabilize the snaking oscillations. Stabilization could be also achieved by increasing the structural damping of the system, for instance introducing friction at the articulation joint.

He et al. [16] devised a similar linearized combined mechanical and hydraulic model of an ASV, as shown in Figure 1-6. Their work was intended to further investigate the effects of the steering system on lateral stability of ASVs. The model of the hydraulic steering system in their work was the type that is common in passenger cars, including the torsion bar and mechanical rack and pinion. The sliding valve in the previous combined model, developed by Horton and Crolla in [10], was replaced with a rotary valve. Their results showed that, with the introduction of fluid leakage either in the rotary valve or in the hydraulic cylinder, the stability of the oversteer mode was degraded. However, in the case of snaking mode, the introduction of the fluid leakage improves the stability of the vehicle.

1.2 Problem Statement

Over the past decades, high-power engines and new powertrains have created a continuous increase in operational speeds of ASVs [5]. Also, there is a growing demand for transport-oriented ASVs in applications such as agriculture and forestry, which results in considerably
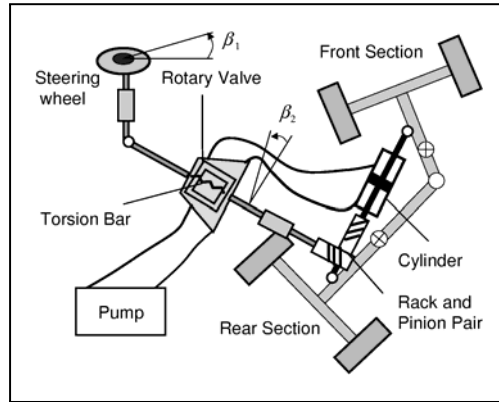
Figure 1-6: A combined model of an ASV [16].

higher speeds [17]. In view of the continual increase in operational speeds of ASVs on public roads and highways, a high level of technical safety should be provided for these vehicles [5], as there is no guarantee of the driver behavior being sympathetic during critical conditions. However, ASVs have received surprisingly little attention in this area. This may be due to the fact that, traditionally, these vehicles have been relegated to low-speed applications, such as in agriculture, forestry and construction, whereas the safety problems of road vehicles are due to their instability and dynamic behavior at high speeds.

An articulated steer logging tractor, produced by Timberjack[1], is a practical example of a conventional ASV that is subject to safety problems. This vehicle, commonly called a forestry skidder, can be used for performing various types of tasks on various terrains. It is usually used to transport logs from one place (e.g. where the trees are cut) to another place (e.g. where the logs are loaded onto trucks for further transportation). In addition, it may be equipped with different front-mounted and rear-mounted attachments for various applications. A grapple-type forestry skidder (illustrated in Figure 1-7) pushes and stacks logs with its front dozer, and drags and lifts the logs with its rear grapple. Road experience has indicated that some problems can occur when these vehicles, which are mainly designed for working on off-road surfaces, travel at higher speeds on roads and highways. Based on practical reports by the manufacturer, these vehicles are most prone to the snaking oscillations at forward speeds of approximately 40 km/h

---

[1]A John Deere Company

10
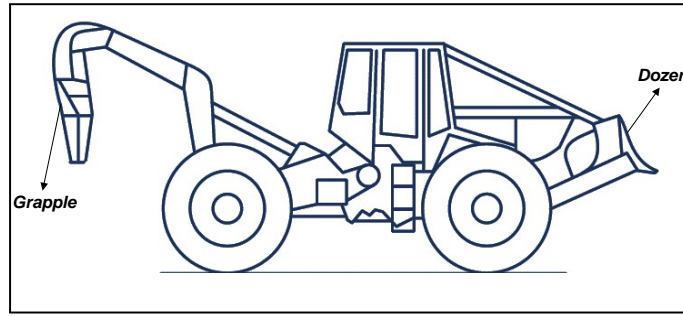
Figure 1-7: A schematic of a forestry skidder.

and higher. During this motion, the two parts of the vehicle oscillate relative to each other at low frequency.

Referring to the research literature, it is obvious that previous studies on the stability of ASVs at higher speeds are limited. For instance, regarding the snaking mode, they are mainly concerned with the analysis of the effects of the steering system characteristics [10]. These analyses suggested some changes in the steering system properties to decrease the snaking oscillations. The snaking mode may be alleviated by using passive methods, such as increasing friction at the articulation joint or introducing leakage flow across the hydraulic cylinders. Although these methods may be applicable to improve the lateral stability during the snaking mode for some cases, they are not effective and reliable methods for this purpose in many cases, as will be shown later. Moreover, they result in loss of power and the introduction of nonlinearity to the steering system operation, which are not acceptable. Therefore, attention must be paid to the development of some effective methods to remove the lateral instability of ASVs during the snaking mode.

Active safety devices for a better control of wheel steer vehicles were first introduced to the market two decades ago [18]. These systems help drivers to control the vehicle in critical situations. Nowadays, many light-duty vehicles, for instance passenger cars, have been equipped with such systems. In these systems, the required yaw moment to control the vehicle may be produced by different strategies. The most common strategies are active steering, torque vectoring and differential braking. The controller design is critical for these devices due to the fact that the control system must be developed with regard to existing uncertainties of the

vehicle parameters and its driving conditions. For instance, tire-road contact parameters may change very rapidly and in an unknown pattern when the vehicle is traveling. Similar active devices may be designed to remove the instability of ASVs during the snaking mode. Based on the knowledge of the author, no attempt has been made to apply the above-mentioned systems to prevent the snaking mode of ASVs. The development of such systems is not possible without extending the previous work by more detailed analyses. More insights into the causes of the instability must be examined, and the effects of various vehicle parameters and operating conditions on the stability must be also examined sufficiently. In addition, the previous studies have been limited to analyses of simplified models, and neglect some effects, for instance, tire rolling resistance. Therefore, no process has been conducted to verify the results from these simplified models or to analyze the effects of the parameters ignored in the development of these models. In order to do this, an experimental test of a real vehicle or a simulation of the dynamic behavior in an environment similar to which the actual system will experience is essential.

1.3   Contributions of the Dissertation

This study is intended to cover the lack of research for ASVs by developing several active strategies to stabilize the snaking oscillations of a conventional ASV, specifically, a forestry skidder manufactured by Timberjack. These developments are based on a comprehensive study of the causes of the instability and of the effects of the vehicle parameters and operating conditions on the stability during the snaking mode. In brief, the main contributions of this work are as follows:

- Analysis of the lateral stability of the vehicle with a rear-mounted load having interaction with ground

- Analysis of the lateral stability of the vehicle with front and rear differentials locked

- Design of an active torque vectoring device with robust full state feedback controller based on the Lyapunov method

- Design of a differential braking system with robust variable structure controller

1.4　Outline of the Dissertation

In Chapter 2, the causes of the lateral instability of the baseline vehicle (i.e. the forestry skidder) during the snaking mode are determined. The investigations are mainly concentrated on examining the effects of forward speed and parameters of two main subsystems of the vehicle, the steering system and tire. The preliminary analyses are conducted using various models of the vehicle developed by simplifying assumptions. Several on-road and off-road tire models, including linear, Fiala, mobility number-based and Metz models are detailed. Moreover, two types of steering systems, including hydrostatic and hydraulic-mechanical systems, are explained. Based on the pressure-flow equation for a hydraulic-mechanical steering system, a model for the steering system characteristics is proposed. Two linearized models of the baseline vehicle, including 1-DOF and 3-DOF models, are built. They are used for the lateral stability analysis in travelling with different forward speeds by the eigenvalues of the system. The eigenvalue results from the 3-DOF model analysis are validated by using the data for an ASV introduced in [3]. This model is also utilized for identifying the effects of the steering system characteristics on the lateral stability. To verify the results from the 3-DOF model, a virtual prototype of the baseline vehicle in ADAMS[2] is developed. The response of the vehicle is simulated for different situations, and the results are compared with those from the 3-DOF model analysis. Moreover, based on the simulations, the crucial effects of the resultant lateral force produced at the front and rear axles on the stability are investigated.

In Chapter 3, the effects of different parameters and operating conditions on the lateral stability of the baseline vehicle during the snaking mode are studied. Regarding the operation of the vehicle for doing different tasks, such as for load-carrying at the front or rear, it is equipped with several front and rear-mounted attachments. Therefore, the vehicle parameters such as mass properties and center of mass positions for both the rear and front parts can change. The operating conditions may also vary for the vehicle, owing to travel on different soft and hard surfaces, such as soils, gravel and highway, to travel in a straight-line or a steady-state turning, with constant forward speed or forward acceleration. Also, the vehicle usually has differential locks on the front and rear axles, which are locked for making more

---

[2]ADAMS is a trademark and product of MSC Software.

traction or carrying loads. In addition, the vehicle may be utilized to pull a rear-mounted load or attachment having interaction with the ground. A change in the vehicle parameters or its operating condition affects the lateral stability during the snaking mode. The effects of these changes on the stability of the baseline vehicle are analyzed by using the eigenvalue results, critical speed, and critical torsional stiffness of the vehicle. Although some of these studies are conducted using the 3-DOF model, to study the effects of locking differentials and carrying a load having interaction with the ground, the 3-DOF model is extended to 5-DOF and 4-DOF models, respectively. To verify all of the results from the above conducted analyses, some simulations are done using the virtual prototype of the vehicle in ADAMS. The virtual prototype is also modified for the operating conditions.

In Chapter 4, some studies are conducted to show the shortcomings of passive methods and then, the use of stability control systems to remove the instability during the snaking mode of the baseline vehicle is examined. Two common techniques that are available for yaw moment control of wheel steer vehicles are proposed for the stability control of the baseline vehicle. These include making a change in the steering or articulation angle (i.e. active steering) and producing a yaw moment by producing different values of driving or braking force on the two sides of the vehicle (i.e. torque vectoring or differential braking, respectively). However, regarding the effectiveness of these techniques, the focus of the studies will be on using the different values of driving or braking force for stabilization of the vehicle. The main issue for developing these systems is the controller design, owing to the existing uncertainties. Some of the parameters, for instance tire parameters, may change rapidly during operation, and are identified as uncertain time-varying parameters. Other parameters, such mass properties, are constant during operation; however, they can take different values for different operations and are identified as unknown constant parameters. For each stability control strategy, active steering, torque vectoring and differential braking, a different controller is designed. These include classical, robust full-state feedback and robust variable structure controllers. The performance of the resulting systems is examined for different situations. For designing the controller for any strategy, the 3-DOF model is extended to include the important effects in an appropriate way. For developing the active steering system, the extended model consists of the steering system equation. For designing the torque vectoring device and differential braking system, the extended model includes the wheel

rotational dynamics. The robust controllers are also incorporated into the virtual prototype of the vehicle, and the performance is evaluated for different conditions.

In Chapter 5, a summary of the results is presented. Finally, some research topics are introduced as potential future work on the subject of stability of ASVs.

Chapter 2

Vehicle Dynamic Modeling and Stability Analysis

As mentioned before, the most common problem encountered in the use of an ASV with the articulation joint in the middle is the emergence of a snaking mode at high speeds. Following a small perturbation in traveling in a straight line, either by the steering input or by an external disturbance, a weaving change in the articulation angle will occur. This chapter is intended to analyze the causes of the lateral instability of the baseline vehicle during this undesirable behavior. The effects of forward speed and properties of two main subsystems of the vehicle, the steering system and tires, are pivotal for these analyses. Several models of the baseline vehicle are developed, and a lateral stability analysis is conducted in terms of the forward speed of the vehicle. These models are built based on the models of vehicle subsystems, including tire and steering system. First, the modeling aspects of the force and moment generation at the tire-ground contact area are detailed. Various on-road and off-road tire models, including linear, Fiala, mobility number-based and Metz models are introduced. Then, two types of steering systems that are commonly used for ASVs, including hydrostatic and hydraulic-mechanical systems, are described. The pressure-flow equation for a hydraulic-mechanical steering system is reviewed, and, in view of this equation, a model for the steering system characteristics is introduced. By using the models representing the vehicle subsystems, two simplified models of the baseline vehicle, including 1-DOF and 3-DOF models, are developed. These models are used

to analyze the lateral stability of the baseline vehicle during the snaking mode in travelling with different forward speeds, based on the eigenvalues of the system. The eigenvalue results from the 3-DOF model analysis are first validated based on results presented in the previous work for an articulated steer tractor. The effects of the steering system characteristics on the stability are also investigated using the 3-DOF model. A virtual prototype of the baseline vehicle is built in ADAMS, and the change in the articulation angle is simulated during the snaking mode. The results from the 3-DOF model and the simulations in ADAMS are compared for different conditions. Finally, based on the simulations, the interaction of the resultant lateral force produced at the front and rear axles as an important factor for the stability of the vehicle is studied. Most of the materials of this chapter were previously published in [19, 20].

2.1 Modeling of Tires

Knowledge of forces and moments generated at the tire-terrain contact area is essential to any study of road vehicle dynamics. The external forces that can cause longitudinal or lateral motion of a road vehicle are mainly generated at the tires. Research on the forces and moments generated by tires has been conducted by using different analyses and measurements. The reader can refer to [21], a definitive book about tire mechanics and modeling, for comprehensive information. In general, the interaction between a tire and the terrain is dominated by the deformations of these bodies in the contact area. Depending on the values of the deformations, four different conditions can be assumed: (i) a rigid tire on a deformable surface, (ii) a flexible tire on a hard surface, (iii) a flexible tire on a deformable surface, and (iv) a rigid tire on a hard surface. The last case is assumed for the study of dynamics of railway vehicles. The second case is assumed for the study of motion of road vehicles on hard surfaces, and the third case is commonly assumed for the study of off-road vehicle motion on deformable terrains. Also, the first case may be used to study the motion of a high pressure tire on a soft soil.

Various moments and forces are generated at the tire-road contact area. To describe these forces and moments, a tire coordinate system must be defined. The SAE tire coordinate system is shown in Figure 2-1. The SAE coordinate system is the one defined by the Society of Automotive Engineering, and ISO provides another alternative. The origin of the SAE coordinate
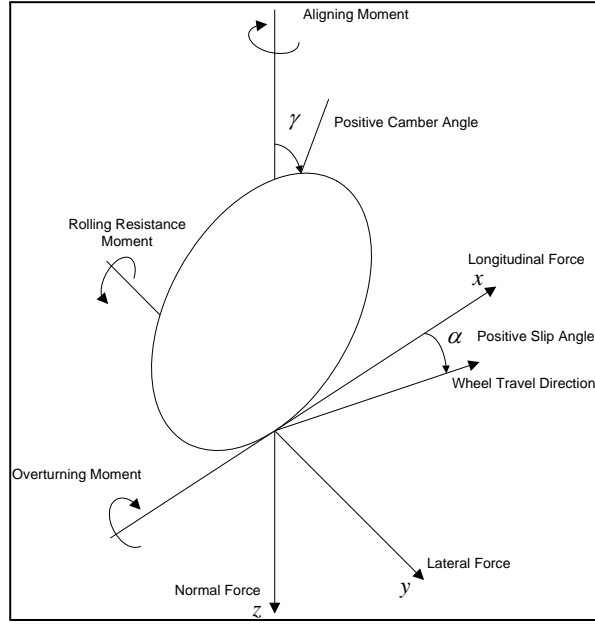
Figure 2-1: The SAE tire coordinate system.

system is the center of the contact area. The x axis is the intersection of the wheel plane and the ground plane with a positive direction forward. The z axis is perpendicular to the ground plane with a positive direction downward. The y axis is in the ground plane, and its direction is chosen to make the coordinate system right hand. In the ISO axis system, the x axis has the same direction as in the SAE axis system. However, the y and z axes have opposite directions.

There are three forces and three moments generated at the contact area. The longitudinal tire force F_x is produced at the contact area due to the wheel longitudinal slip S when a torque is applied about the wheel spin axis. The wheel longitudinal slip may be defined in different ways, such as the following suggested by the SAE:

$$S = -\frac{V_x - r_e \varpi}{V_x} \tag{2.1}$$

where ϖ represents the wheel angular velocity, V_x is the wheel center velocity in the x direction and r_e is effective rolling radius, which is slightly different from the tire undeflected radius. For the freely rolling wheel, the forward wheel speed $V_\circ$ and the angular velocity $\varpi_\circ$ can be measured to find r_e by the following equation:

$$r_e = \frac{V_{\circ}}{\varpi_{\circ}} \tag{2.2}$$

During forward acceleration, the wheel angular velocity ϖ is increased, and thus the wheel slip becomes positive. However, during braking, the wheel slip becomes negative.

The lateral force generated at the tire F_y is very important for steering, side slope operation and also lateral stability of road vehicles. On hard surfaces, F_y depends on the slip angle α, the vertical tire load F_z and also the friction coefficient μ. Typical tire-ground friction coefficients for different surfaces are given in Table 2.1 from [22]. The maximum value of this coefficient μ_{max} determines the peak value of the tire force when the saturation is reached. The sliding value of this coefficient μ_s is related to the conditions in which the whole contact area is dominated by sliding and the longitudinal slip is 100 percent [23].

The slip angle α is defined as the angle between the direction of the tire centre line and the direction in which it is actually traveling, as shown in Figure 2-1. This definition is used for both a steered and non-steered wheel, based on the following equation [21] (suggested by the SAE):

$$\tan\alpha = \frac{V_{cy}}{V_{cx}} \tag{2.3}$$

where V_{cx} and V_{cy} represent the components of the velocity of the tire contact patch center in the x and y directions. In addition to α, tire camber angle γ, the angle formed between the xz plane and the wheel plane, produces lateral tire deformation and thus, tire lateral force. In general, this lateral force and that due to α are additive. Usually, F_y acts behind the center of the contact area which causes the self-aligning moment M_z, a restoring effect that attempts to return the tire to a zero slip angle state. The moment arm t_p is known as pneumatic trail. The aligning moment M_z also depends on the slip angle α at which the tire is traveling, and also the tire vertical load F_z.

In addition to the aligning moment, two other moments are also produced at the tire contact area: overturning moment M_x and rolling resistance moment M_y. The overturning moment is caused by a lateral shift of the vertical load during cornering. The rolling resistance of tires on hard surfaces is mainly produced by the hysteresis in tire materials. Other factors, such as

Surface	$\mu_{\max}$	μ_s
Asphalt and concrete (dry)	0.8-0.9	0.75
Asphalt (wet)	0.5-0.7	0.45-0.6
Concrete (wet)	0.8	0.77
Gravel	0.6	0.55
Earth road (dry)	0.68	0.65
Earth road (wet)	0.55	0.4-0.5
Snow (hard-packet)	0.1	0.07
Ice	0.1	0.07

Table 2.1: Friction coefficients for different surfaces [22].

friction at the contact area due to sliding, the air resistance inside the tire, and the fan effect of the spinning tire, have less effects. When the carcass is deformed during rolling, the normal pressure in the leading half of the contact area is higher than that in the trailing half. Thus, the center of normal pressure is displaced in the direction of rolling, which generates a moment about the axis of rotation of the tire, called the rolling resistance moment. In a free-rolling tire with constant angular speed, a horizontal force at the contact area must exist to maintain equilibrium. This horizontal force is called the rolling resistance F_r, and the ratio of the rolling resistance to the normal tire force is described as the coefficient of rolling resistance C_{rr}:

$$F_r = C_{rr}F_z \tag{2.4}$$

When a tire is traveling with a longitudinal slip S or slip angle α on a hard surface, the contact area is deformed. The lateral and longitudinal deformation of the tire is dominated by both adhesion and sliding phenomena. At a part of the contact area, the tread elements adhere to the surface and the deformation increases proportional to distance from the initial contact point between the surface and the tire. At a point where the tire-ground friction cannot support further tire deformation, the tread elements slide laterally or longitudinally. When S or α increases, a greater part of the contact area is involved in the sliding, and at higher values of S or α, a maximum force F_x or F_y is reached and saturation occurs. However, the pneumatic trail t_p decreases once sliding begins and approaches zero at higher slip angles. In this case, the aligning moment M_z is reduced to near zero and may even reverse sign.

Moreover, for any change in S or α, tires have a finite response time related to the time taken

for the contact area to achieve a new deformed shape. This dynamic effect can be represented by the following equation [17]:

$$F = F_{st}(1 - e^{\frac{-x}{l_r}}) \tag{2.5}$$

where:

F : Tire force (lateral or longitudinal)

F_{st} : Steady-state value of force

x : Distance rolled by tire following a perturbation

l_r : Relaxation length

For the lateral force generation, l_r is approximately equal to the rolling radius of the tire. Equation (2.5) indicates a first order lag when it is written in the time domain, with break frequency $\frac{u}{l_r}$, where u is the vehicle forward speed. When u is low and l_r is large, the tire transient response will be important. Large and soft tires have a higher tire relaxation length l_r. For the steady-state conditions, F_x, F_y and M_z are functions of S, α , F_z and γ:

$$F_x = F_x(S, \alpha, F_z, \gamma), F_y = F_y(S, \alpha, F_z, \gamma), M_z = M_z(S, \alpha, F_z, \gamma) \tag{2.6}$$

The functions $F_x(S, \alpha, F_z, \gamma)$, $F_y(S, \alpha, F_z, \gamma)$ and $M_z(S, \alpha, F_z, \gamma)$ can be obtained from experimental measurements for a given speed and road condition (experimental models). Figure 2-2 shows typical lateral tire force and aligning moment characteristic curves on hard surfaces [21].

2.1.1   Linear Tire Model

Pure slip is a condition when either tire longitudinal slip or lateral slip occurs in isolation. For the pure slip conditions, the slope of the tire characteristics curves at zero slip is expressed as the longitudinal slip stiffness C_{Fs}, lateral slip stiffness or cornering stiffness $C_{F\alpha}$ and aligning stiffness $C_{T\alpha}$, respectively:

$$C_{Fs} = (\frac{\partial F_x}{\partial S})_{S=0} \tag{2.7}$$

$$C_{F\alpha} = (\frac{\partial F_y}{\partial \alpha})_{\alpha=0} \tag{2.8}$$
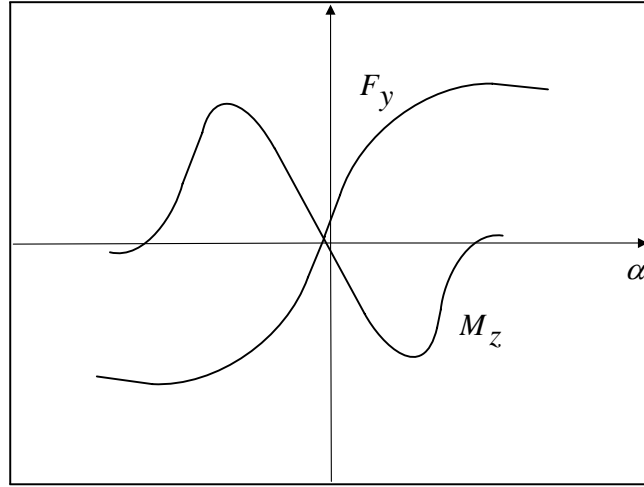
Figure 2-2: Lateral tire force and aligning moment characteristic curves on hard surfaces.

$$C_{T\alpha} = -(\frac{\partial M_z}{\partial \alpha})_{\alpha=0} \tag{2.9}$$

The longitudinal slip stiffness C_{Fs} is typically higher than the cornering stiffness $C_{F\alpha}$, but for equal lateral and longitudinal tire stiffness, C_{Fs} and $C_{F\alpha}$ will be equal [21]. For small levels of slip, the linearized functions for tire forces and moment can be represented by the following expressions:

$$F_x = C_{Fs}S \tag{2.10}$$

$$F_y = C_{F\alpha}\alpha \tag{2.11}$$

$$M_z = -C_{T\alpha}\alpha \tag{2.12}$$

2.1.2 Fiala Tire Model

In addition to experimental measurements, analytical functions are used to compute tire forces and moments. For instance, Fiala developed a tire model based on the deformation parameters at the contact area. The analytical functions to compute the tire forces and moments based on this model can be found in [21]. For small levels of slips, these analytical functions can be linearized and take the same form as the equations for the linear tire model. In addition, based

on this model, $C_{T\alpha}$ can be related to $C_{F\alpha}$ by the following equation [21]:

$$C_{T\alpha} = \frac{C_{F\alpha}l_t}{6} \qquad (2.13)$$

where l_t is the tire contact length, and can be computed by the following expression for off-road tires [24]:

$$l_t = C_l\sqrt{\delta_t(d_t - \delta_t)} \qquad (2.14)$$

where δ_t is the tire vertical deflection under its vertical load on a rigid surface and d_t is the overall tire diameter. The coefficient of C_l (dimensionless) can be computed by using the following empirical equation [24]:

$$C_l = \frac{23}{\left(\left|\frac{d_t}{b_t} - 3.5\right| + 11.9\right)} \qquad (2.15)$$

where b_t is the tire width.

2.1.3 Mobility Number-Based Off-road Tire Model

During motion of vehicles on deformable surfaces, the tire tread penetration into the ground is also important, and thus, the forces which can be generated at the tire contact area depend on the strength of the soil in shear and on tire-soil friction. When a tire is travelling with lateral or longitudinal slip on a deformable surface, tread distortion occurs at the contact area. The tire elastic deformation occurs in a part of the contact area. However, at some point, the shear force due to tire deformations equals the soil shear strength and there is no further tire deformation and soil shear occurs. Soil shear strength is typically less than tire-ground friction on hard surfaces, hence the maximum tire force produced on deformable surfaces is reduced. There are more problems related to the measurements of tire force characteristics on deformable surfaces. For instance, on field surfaces, many repeated tests must be conducted to reach a suitable statistical accuracy. A summary of data measurements on deformable surfaces was reported in [17]. Based on the measured data, the relation between F_x and wheel slip S^*

can be represented by the following equation [17]:

$$F_x = F_z C_{s\,\text{max}}(1 - e^{-k_1 S^*}) \tag{2.16}$$

where $C_{s\,\text{max}}$ and k_1 are constants for particular conditions. In Equation (2.16), S^* is defined as follows:

$$S^* = 1 - \frac{V_x}{r_e \varpi} \tag{2.17}$$

The generation of F_y with wheel slip α can be approximated by a similar equation to the longitudinal force generation:

$$F_y = F_z C_{\alpha\,\text{max}}(1 - e^{-k_2 \alpha}) \tag{2.18}$$

where $C_{\alpha\,\text{max}}$ and k_2 refer to a specific set of tire parameters and terrain conditions. Different forms of this empirical equation, for instance, polynomials of different orders, have been also suggested, but the exponential form is both accurate and simple. This equation is analogous to soil shear behavior (shear-displacement curve), which dominates the tire force generation on deformable surfaces. Different methods to obtain coefficients of $C_{\alpha\,\text{max}}$ and k_2 have been suggested. These methods are commonly based on different forms of mobility number. The mobility number was first defined by using dimensional analysis to model the tire forces, and consists of effects of tire size, load and soil conditions [25]. One of the most important forms of the mobility number MOB (dimensionless) is computed for any F_z by using [17]:

$$MOB = \frac{\sqrt{\frac{\delta_t}{h_t}}(C_I b_t d_t)}{F_z(1 + (\frac{b_t}{2d_t}))} \tag{2.19}$$

where the soil cone index C_I is a parameter to describe the strength of soil in terms of its resistance to the penetration of a standard size cone, and h_t is the tire section height (distance from the bottom of the bead to the top of the tread). The soil penetration resistance depends on moisture content, specific weight and soil type. Typically, cone index readings of 200 kPa, 700 kPa and 1500 kPa represent loose, average and firm field conditions, respectively [26]. Tire deflection δ_t is measured statically on a hard surface. The value of $\frac{\delta_t}{h_t}$ at a manufacturer's

recommended load and inflation pressure is about 0.2 for off-road tires. For bias-ply tires, coefficients of $C_{\alpha\max}$ and k_2 can be computed by using [17]:

$$C_{\alpha\max} = \frac{0.69}{MOB} + 0.61 \qquad (2.20)$$

$$k_2 C_{\alpha\max} = 2.34 + 0.088 MOB \qquad (2.21)$$

For small slip angles ($\leq 10°$), Equation (2.18) can be reasonably linearized:

$$F_y = F_z C_\alpha \alpha \qquad (2.22)$$

where α is in radian, C_α is the lateral force coefficient and:

$$C_\alpha = k_2 C_{\alpha\max} \qquad (2.23)$$

Similarly, the tire aligning moment for small slip angles can be described by:

$$M_z = -F_z C_{M\alpha} \alpha \qquad (2.24)$$

where $C_{M\alpha}$ is the tire aligning moment coefficient. There is a relation similar to Equation (2.13) between C_α and $C_{M\alpha}$. The similar relations for $C_{s\max}$ and k_1 in terms of MOB are [17]:

$$C_{s\max} = 0.796 - \frac{0.92}{MOB} \qquad (2.25)$$

$$k_1 C_{s\max} = 4.838 + 0.061 MOB \qquad (2.26)$$

Similarly, for small longitudinal slip:

$$F_x = F_z C_s S^* \qquad (2.27)$$

where C_s is the longitudinal force coefficient and:

$$C_s = k_1 C_{s\max} \qquad (2.28)$$

In addition, the coefficient of rolling resistance C_{rr} can be also predicted by MOB as follows [27]:

$$C_{rr} = 0.049 + \frac{0.287}{MOB} \tag{2.29}$$

In order to model tire forces in the pure longitudinal or lateral slip, Equations (2.16) and (2.18) can be used. However, when both forces are generated in combination and at the same time, the modified equations described in [17] offer an approximate representation of the real behavior. Under this condition, the lateral force characteristic curve is assumed to be controlled by generated longitudinal force (friction ellipse model), and $C_{\alpha\max}$ is computed by [17]:

$$\left(\frac{C_{\alpha\max}}{C'_{\alpha\max}}\right)^2 + \left(\frac{F_x}{F_z C_{s\max}}\right)^2 = 1 \tag{2.30}$$

where $C'_{\alpha\max}$ is related to the pure lateral slip conditions when $F_x = 0$.

2.1.4 Metz Tire Model

Metz has introduced an empirical tire model to predict the lateral force during motion on different surfaces [28]. This model has been developed for pure cornering, when both camber and longitudinal wheel slip are negligible. This model relates F_y and α by using an exponential function as follows:

$$F_y = AF_z(1 - e^{-B\alpha}) \tag{2.31}$$

where A is given in Table 2.2 for different surfaces, and B (with unit of 1/deg) is determined for a specific conditions of the tire and surface by the following equation:

$$B = \frac{C}{A}\left(\frac{F_{ZT}}{F_z}\right)^m + \left(\frac{D}{A}\right) \tag{2.32}$$

where F_{ZT} is the tire design load at operation pressure and m is an exponent equal to 0.14. The coefficients of C and D are also given in Table 2.2 for different surfaces.

Based on Equation (2.31) and Equation (2.8), the cornering stiffness $C_{F\alpha}$ can be computed as follows:

26

Surface	A	C	D
Highway	0.67	0.677	-0.563
Plowed Field	0.65	0.267	-0.222
Gravel	0.52	0.588	-0.489
Corn Field	0.53	0.440	-0.365
Meadow	0.88	0.784	-0.652

Table 2.2: Metz tire model coefficients for different surfaces [28].

$$C_{F\alpha} = ABF_z \tag{2.33}$$

Then, F_y for the small slip angles becomes:

$$F_y = ABF_z\alpha \tag{2.34}$$

In general, the cornering stiffness of tires on a highway surface is higher than that for off-road surfaces. However, owing to the interaction of tire tread and rooted plants in the meadow, it is high in the meadow, as well [28]. Moreover, comparing Equations (2.34) and (2.22) shows that:

$$C_\alpha = AB \tag{2.35}$$

2.2 Modeling of Steering Systems

Both hydrostatic and hydraulic-mechanical steering systems are adopted for ASVs [9]. The steering control can be either an open loop or a closed loop, depending on the application. In the following sections, the construction and operation of the steering systems are described, and a model for representing the steering system characteristics is introduced.

2.2.1 Hydrostatic Steering Systems

Hydrostatic steering systems are used to control off-road trucks, earth-moving machines, and tractors that require high steering forces. In the past, hydrostatic steering systems used a pilot valve with a small displacement to control a directional valve. However, today, hydrostatic steering systems include a gerotor as an oil meter element. In this system (i.e. metered flow),
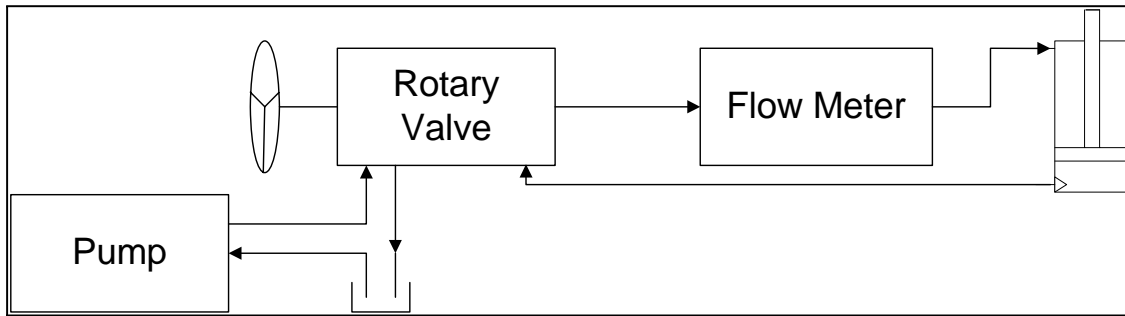
Figure 2-3: A schematic of a hydrostatic steering system.

the oil volume sent to the hydraulic cylinders is proportional to the input turning angle of the steering wheel, as shown schematically in Figure 2-3, and there is usually no feedback from the articulation angle (open-loop steering system). The steering valve is usually similar to the type described in [29], which consists of a rotary valve with a spool inside a sleeve within a housing. When the steering wheel is turned, the spool rotates relative to the sleeve, and opens paths that permit oil flow through the spool and sleeve combination. Oil flows to a gerotor set and causes the gerotor to rotate. The gerotor functions as an oil flow meter, and when the rotation of the steering wheel stops, the gerotor gear continues to rotate until the sleeve stops the flow to the gerotor.

The pressure-flow equation for such a steering system has been developed for both a closed-loop and an open-loop control in [10]. In the closed-loop system, the difference between the desirable articulation angle and the actual angle was used to regulate the valve displacement by proportional control. The resulting equations representing the steering system characteristics for both open- and closed-loop control is similar to that for a hydraulic-mechanical system, which is introduced in the next section. Moreover, Horton and Crolla's work [10] showed that the closed-loop control has no important benefit over the open-loop control in terms of the lateral stability.

2.2.2 Hydraulic-Mechanical Steering Systems

In hydraulic-mechanical steering systems, a hydraulic valve is activated by a mechanical input, for instance by turning a steering wheel. The connection between the steering wheel and the

28
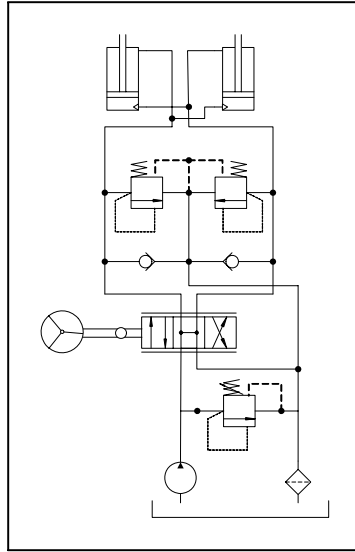
Figure 2-4: A schematic of hydraulic-mechanical steering systems.

hydraulic valve is mechanical. The most commonly used hydraulic valve is a sliding valve with spool type construction. This valve controls the flow of hydraulic fluid from a pump to the cylinders, as shown schematically in Figure 2-4 by standard hydraulic symbols. A closed-loop control may also be used for hydraulic-mechanical steering systems. In this case, there is a mechanical feedback unit, for instance a four-bar linkage [30].

2.2.3 Pressure-Flow Equation for Steering System

In this section, an equation that describes the pressure-flow relationship for an open-loop hydraulic-mechanical steering system is presented. A hydraulic-mechanical steering system includes two cross-connected steering cylinders, as depicted in Figure 2-5. They can be represented by a single double-acting cylinder with the following effective area:

$$A_e = \frac{\pi}{4}[(d_p^2 - d_r^2) + d_p^2] \tag{2.36}$$

where d_p and d_r are the piston and rod diameters for each steering cylinder, respectively.

Therefore, a hydraulic-mechanical steering system can be represented by a combination of a sliding valve and a hydraulic cylinder, as illustrated in Figure 2-6. For a sliding valve with

29
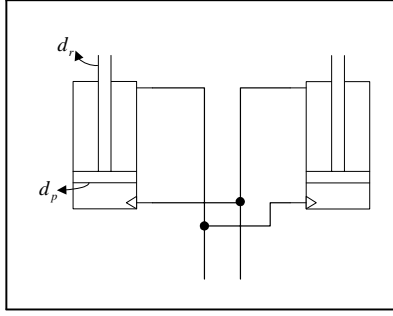
Figure 2-5: A schematic of cross-connected hydraulic cylinders.

matched and symmetrical orifices, an explanation for deriving the linearized equation around the origin point of the pressure-flow curve is given in [31]. In summary, based on the equations governing the piston motion and the flow in the chambers and some simplifying assumptions, the pressure-flow equation is described as follows [31]:

$$K_q x_v = A_e \frac{dx_p}{dt} + (C_{tp} + K_c)P_L + \frac{V_t}{4\beta_e} \frac{dP_L}{dt} \tag{2.37}$$

where,

V_t : Total volume of chambers

K_q : Valve flow gain

K_c : Valve flow-pressure coefficient

C_{tp} : Total leakage coefficient (internal and external)

P_L : Pressure difference

x_v : Displacement of spool

x_p : Displacement of piston

A_e : Effective area of hydraulic cylinders

β_e : Effective bulk modulus of system (including oil, entrapped air, and mechanical compliance of system)

The pressure difference P_L is defined as:

$$P_L = P_1 - P_2 \tag{2.38}$$
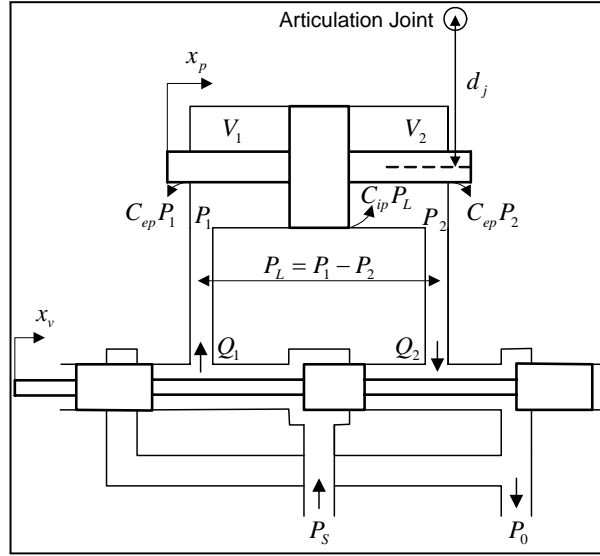
Figure 2-6: A model of an open-loop hydraulic-mechanical steering system.

where P_1 and P_2 represent pressure of the forward and return chamber of the cylinder, respectively. For small values of articulation angle ϕ, the following equation can be used:

$$x_p = \phi d_j \qquad (2.39)$$

where d_j is the perpendicular distance from the articulation point to the steering cylinder, as shown in Figure 2-6. Therefore, Equation (2.37) can be rewritten as:

$$K_q x_v = A_e d_j \frac{d\phi}{dt} + (C_{tp} + K_c)P_L + \frac{V_t}{4\beta_e}\frac{dP_L}{dt} \qquad (2.40)$$

It is easy to see that this equation is similar to those derived for both a closed-loop and an open-loop hydrostatic steering system by Horton and Crolla [10], which are in the normalized form. The torque T_S generated by the steering system can be computed by the following equation:

$$T_S = P_L A_e d_j \qquad (2.41)$$

For a critically closed center valve and by assuming negligible leakage across the cylinder, K_c and C_{tp} can be ignored. Therefore, when the valve is in the neutral position ($x_v = 0$), P_L can

31

be found from Equation (2.40) in terms of ϕ. Under this condition, by using Equation (2.41), T_S is:

$$T_S = -\frac{4A_e^2 d_j^2}{V_t}\beta_e\phi \tag{2.42}$$

Therefore, the steering system is equivalent to a torsional spring at the articulation joint with the following stiffness:

$$K_S = \frac{4A_e^2 d_j^2}{V_t}\beta_e \tag{2.43}$$

where K_S is equivalent torsional stiffness of the steering system, and is dependent on β_e. This equation agrees with that shown by Horton and Crolla [10] for a hydrostatic steering system; the compressibility effect of the trapped oil in the cylinders corresponds to a combination of two torsional springs at the articulation joint with the stiffness K_R as follows:

$$K_R = (\frac{1}{V_1} + \frac{1}{V_2})A_e^2 d_j^2\beta_e \tag{2.44}$$

where, V_1 and V_2 are the fluid volume of the chambers with increasing and decreasing volumes, respectively. In the neutral position with $V_1 = V_2 = \frac{V_t}{2}$, Equations (2.43) and (2.44) will be the same ($K_S = K_R$). From the manufacturer's data, the parameters of the hydraulic system for the baseline vehicle are given in Table 2.3. In the absence of entrapped air and flexible pipes, the effective bulk modulus β_e is equal to the bulk modulus of the hydraulic fluid alone, which is about 1.5×10^9 Pa. For this value of β_e and the given parameters of the hydraulic system, K_S is about 1.5×10^7 Nm/rad, based on Equation (2.43). However, a small amount of the entrapped air can reduce β_e substantially [31]. The value of β_e may be decreased by a factor of up to 100 by inclusion of the effects of the entrapped air and mechanical compliance of the flexible pipes [10].

Owing to friction in the cylinders and articulation joint, torsional damping can be considered at the joint (i.e. structural damping). In general, the structural damping is a constant value. Horton and Crolla [10] showed that introducing leakage across the cylinders in a steering system with a typical closed center valve ($C_{tp}+K_c \neq 0$) is equivalent to increasing the torsional damping at the articulation joint in terms of the lateral stability. Therefore, an equivalent torsional

32

Parameter	Unit	Value
A_e	m^2	0.01
K_q	m^2/s	5
d_j	m	0.5
V_1	m^3	0.005
V_2	m^3	0.005

Table 2.3: Parameters of steering system for baseline vehicle.

damping C_R at the articulation joint can be used to show the effects of friction and leakage. In summary, the steering system of the vehicle can be modeled as a combination of torsional spring K_R and a torsional damping C_R at the articulation joint.

2.3   1-DOF Vehicle Model and Stability Analysis during Snaking Mode

One important nominal motion of an ASV, or of any other road vehicle, is constant speed operation in a straight-line. It is desirable that this motion be stable. To study this motion, a linear analysis of the lateral stability is conducted. Such analyses have been presented by several authors [3, 10, 32, 16]. The general approach to these analyses is to derive the linear differential equations that govern the disturbed motion. Next, from the resulting set of the linear equations, the characteristic equation is obtained. Finally, the stability of the system is investigated by considering the coefficients or roots of this equation. This approach can be applied to the different models of the baseline vehicle.

The simplest model of the vehicle with 1-DOF is illustrated in Figure 2-7. This planar model consists of front and rear parts, which are connected to each other by an articulation joint. No input from the steering system is assumed. Therefore, the two parts of the vehicle should be in a locked position. However, due to the compressibility effects in the hydraulic cylinders, some small changes in the articulation angle can occur after disturbing the motion. As mentioned before, a torsional spring K_R and a torsional damper C_R at the articulation joint can be considered. Therefore, when there is no steering input, a resistant torque T_R at the joint represents the hydraulic cylinders. If it is assumed that the front part of the vehicle is not affected by the changes in the articulation angle, the only result is the yawing motion
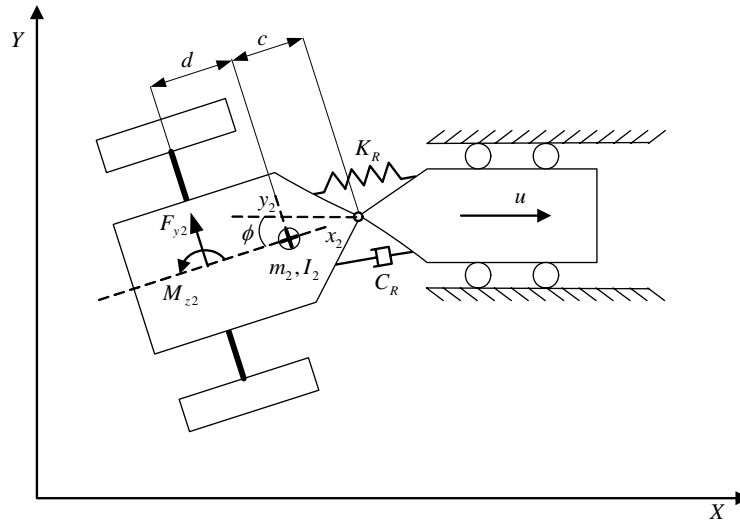
Figure 2-7: A 1-DOF model of an ASV.

of the the rear part. In addition, it is assumed that the tire rolling resistance is very small, and thus, it is neglected. Moreover, the aerodynamic resistance is neglected and a flat road is assumed. Owing to the yaw motion of the rear part, the longitudinal velocity of the rear tires will change. This produces a longitudinal slip, and thus, a longitudinal force at the tires. These forces are much smaller than the lateral force generated at the tires, and thus, they are ignored in the preliminary stage. Also, it is assumed that the vehicle is traveling on a surface with constant tire-road contact parameters. The ISO axis system is used to describe the rear tires lateral forces and aligning moments. The resultant lateral force and moment of the rear tires are assumed to act at the centre of the rear axle. The transient response of the tires is neglected, as this does not affect the main results of the analysis; Horton and Crolla [10] showed that introducing the transient response of the tires to the equations of motion for an ASV is equivalent to increasing the torsional damping C_R slightly, in view of the lateral stability during the snaking mode.

2.3.1 Equation for Perturbed Motion

Assuming that $X - Y$ frame is the global coordinate system fixed to the ground, an equation for the yawing motion of the rear part can be derived with regard to the model shown in Figure

34

2-7. In the following, the subscripts 1 and f refer to the front and 2 and r refer to rear. To derive the equations of motion, the gyroscopic effects are neglected and the axles and wheels are assumed lumped with their respective parts. As mentioned before, the lateral force and aligning moment at each tire are functions of the slip angle, vertical tire load, surface friction properties and camber angle. For small articulation angles ϕ, the average of the left and right tire slip angles at the rear axle α_2 can be described as:

$$\alpha_2 = - \left[\frac{(c+d)\dot{\phi}}{u} + \phi \right] \tag{2.45}$$

As shown in Figure 2-7, c and d are the distance from the articulation point to the rear body center of mass, and the distance from the rear wheels to the rear body center of mass, respectively. As the camber effects for the baseline vehicle with rigid suspension would be negligibly small [28], the resultant lateral force F_{y2} (described in $x_2 - y_2$ frame attached to the rear part center of mass) is a function of α_2, and by using the mobility number-based tire model can be described as:

$$F_{y2} = -N_2 C_{\alpha2}\alpha_2 \tag{2.46}$$

where $C_{\alpha2}$ is the rear tire lateral force coefficient, and it is the same for the left and right tires. In terms of the cornering stiffness, this equation is as follows:

$$F_{y2} = -C_{\alpha r}\alpha_2 \tag{2.47}$$

where $C_{\alpha r}$ is the effective cornering stiffness for the rear axle. The vertical loads at the front and rear axles N_1 and N_2, shown in Figure 2-8, are assumed constant during the motion. They can be computed using static equilibrium equations, as follows:

$$N_1 = \frac{m_1 g(b+c+d) + m_2 g d}{a+b+c+d} \tag{2.48}$$

$$N_2 = (m_1 + m_2)g - N_1 \tag{2.49}$$

where a is the distance from the front body center of mass to the front wheels and b is the distance from the articulation point to the front body center of mass, respectively.
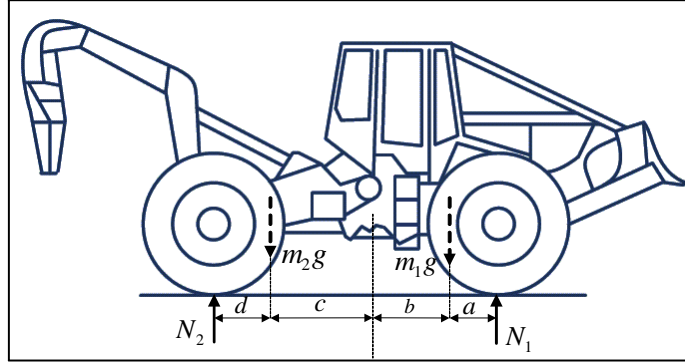
Figure 2-8: Vertical tire loads before perturbed motion.

Also, by using the mobility number-based tire model, the resultant self-aligning moment M_{z2} is:

$$M_{z2} = N_2 C_{M\alpha2} \alpha_2 \qquad (2.50)$$

where $C_{M\alpha2}$ is the rear tire aligning moment coefficient, and it is the same for the left and right tires. In terms of the aligning stiffness, this equation is as follows:

$$M_{z2} = C_{Tr} \alpha_2 \qquad (2.51)$$

where C_{Tr} is the effective aligning stiffness for the rear axle. By using Equation (2.45), F_{y2} is:

$$F_{y2} = N_2 C_{\alpha2} \left[\frac{(c+d)\dot{\phi}}{u} + \phi \right] \qquad (2.52)$$

In addition, M_{z2} is:

$$M_{z2} = -N_2 C_{M\alpha2} \left[\frac{(c+d)\dot{\phi}}{u} + \phi \right] \qquad (2.53)$$

The equation of the moments about the articulation point can be written as:

36

$$(I_2 + m_2c^2)\ddot{\phi} + [N_2C_{\alpha 2}\frac{(c+d)^2}{u} + N_2C_{M\alpha 2}\frac{(c+d)}{u} + C_R]\dot{\phi} + [K_R + N_2C_{M\alpha 2} + (c+d)N_2C_{\alpha 2}]\phi = 0$$
$$(2.54)$$

where m_2 and I_2 are the rear body mass and moment of inertia about its center of mass, respectively. The result is an equation that is analogous to that for a rotational inertia-spring-damper system. If the coefficients of the motion variable (ϕ) and its derivatives ($\dot{\phi}$ and $\ddot{\phi}$) are assumed to be constant in the resulting equation, then, the system can be regarded as Linear Time Invariant (LTI). For the stability analysis, this equation can be transformed into the Laplace notation to obtain the characteristic equation:

$$a_2s^2 + a_1s + a_0 = 0 \qquad (2.55)$$

The coefficients of a_0, a_1, and a_2 are expressions that include the parameters of the vehicle and its subsystems. It is easy to see that the coefficients of the characteristic equation are positive, and thus, based on the Routh criteria, the vehicle is consistently stable. The roots of Equation (2.55), λ_1 and λ_2, are the eigenvalues of the system. In general, the eigenvalues of a system are complex numbers, and provide some information on the natural frequencies and mode shapes of the system. For instance, the imaginary part indicates the damped natural frequency, and the real parts of the eigenvalues reveal the stability of the system. A large negative value indicates a well-damped system, whereas a positive number shows an unstable system. Two types of instability are possible: exponential and oscillatory for zero and non-zero imaginary parts, respectively.

2.3.2 Effects of Forward Speed

Table 2.4 shows the rear part parameters of the baseline vehicle. ASVs are typically designed in such a way that the front and rear part center of mass positions are located near their respective axles ($a = 0$ and $d = 0$). This is to reduce the vertical force applied to the articulation joint. In practice, various changeable rear-mounted and front-mounted attachments can be installed on an ASV, which results in different rear and front center of mass positions. The previous work shows that the snaking mode occurs if the rear center of mass is located behind the rear

Parameter	Unit	Value
m_2	kg	7280
I_2	kgm^2	7280
c	m	1.827
d	m	-0.1
N_2	N	74030
$C_{\alpha 2}$	rad^{-1}	5
$C_{M\alpha 2}$	m/rad	0.4

Table 2.4: Rear part parameters of baseline vehicle.

axle [3]. Therefore, the value of d is set to -0.1 m for a typical position of a rear-mounted grapple of the baseline vehicle. In addition, a set of typical tire parameters ($C_{\alpha 2}$ and $C_{M\alpha 2}$) for traveling on roads and tracks is considered based on [10]. The previous work shows that the snaking oscillations are stronger if K_R and C_R take lower values [10]. Therefore, K_R is given a low value about 1×10^5 Nm/rad, resulting from entrapped air and flexible pipes. The value of C_R is also dependent on the properties of the steering system and articulation joint.

In some cases, C_R can be negligibly small, which has resulted in some practical problems for the steering process of ASVs, such as oil mass resonance. Scholl and Klein [33] showed both practically and theoretically the fluctuations of the steering response of an ASV, which are produced due to very low values of the torsional damping. To overcome this problem, they suggested some compensation methods from [34], which are commonly used to improve response of lightly damped hydraulic drives. For $C_R = 0$, the real parts of λ_1 and λ_2 versus the forward speed u are plotted in Figure 2-9 for the vehicle parameters. For the forward speeds lower than 3.7 m/s, there is a pair of negative distinct real roots, that shows an overdamped yaw motion for the rear part. However, for the higher speeds, there is a negative complex conjugate pair of roots with the same real part that shows an underdamped yaw motion. Equation (2.55) is rearranged to the following well-known form:

$$s^2 + 2\xi \varpi_n s + \varpi_n^2 = 0 \tag{2.56}$$

where ξ and ϖ_n are the damping ratio and natural frequency of the system, respectively. As an example, for the forward velocity $u = 34$ km/h (9.5 m/s), if the parameters of the baseline vehicle are substituted into the frequency and damping ratio expressions, then $\varpi_n = 0.8$ Hz
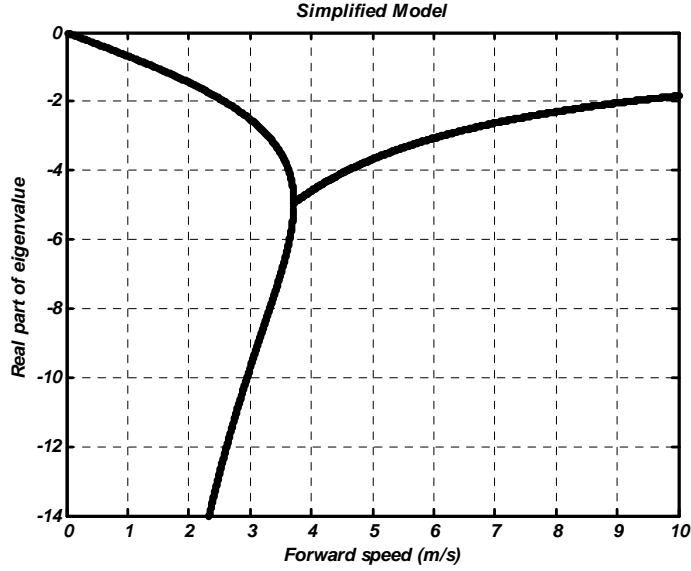
Figure 2-9: Eigenvalue results for a 1-DOF model.

and $\xi = 0.4$. The plot reveals that the real parts of the eigenvalues are negative, and thus, the system is stable. Although Figure 2-9 does not directly reveal any instability, it does indicate that high speeds reduce the damping ratio, an undesirable effect for this system.

2.4 3-DOF Vehicle Model and Stability Analysis during Snaking Mode

The preceding analysis of the 1-DOF model for an ASV does not reveal any oscillatory yaw instability, although it can occur for a real vehicle. Now, the analysis is extended by using a 3-DOF model of an ASV, depicted in Figure 2-10. For this model, ψ is the yaw angle between the front part centreline and X axis. In addition, θ is the angle between the rear part centreline and X axis. Also, u and v represent the local components of the front part center of mass velocity in $x_1 - y_1$ frame attached to the front part center of mass and:

$$u = \dot{X}_1 \cos \psi + \dot{Y}_1 \sin \psi \tag{2.57}$$

39
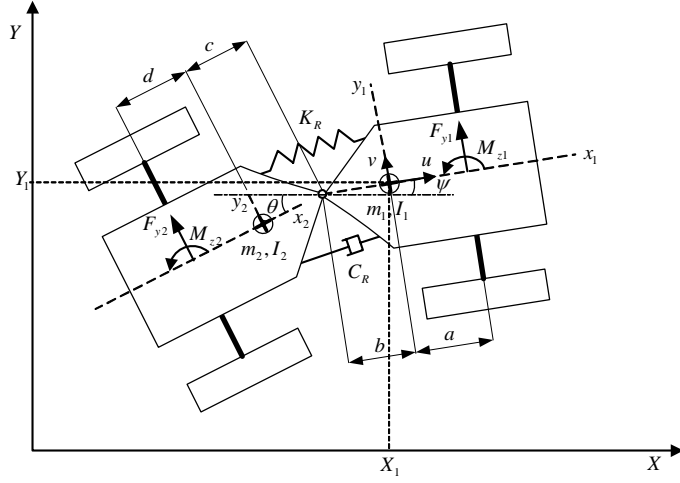
Figure 2-10: A 3-DOF model of an ASV.

$$v = -\dot{X}_1 \sin\psi + \dot{Y}_1 \cos\psi \tag{2.58}$$

The lateral and yaw motions of the front part provide the additional two degrees of freedom; the forward speed u is again assumed constant. The general assumptions are also the same as the 1-DOF model. The devised 3-DOF model is similar to the model presented in [3], except the equations of motion are derived in [3] without considering the tire self-aligning moment. As shown later, the consideration of the tire self-aligning moment can effectively change the predicted behavior in the case where the center of mass positions are near the axles.

2.4.1   Equations for Perturbed Motion

With regard to the model shown in Figure 2-10, the independent coordinates $\mathbf{q}$ to describe the configuration of the system are:

$$\mathbf{q} = [X_1, Y_1, \psi, \theta] \tag{2.59}$$

where X_1 and Y_1 are the absolute coordinates of the front part center of mass. The following form of Lagrange's Equations, including the dissipation function R, will be used to derive the equations of motion:

$$\frac{d}{dt}\left(\frac{\partial T}{\partial \dot{q}_i}\right) - \frac{\partial T}{\partial q_i} + \frac{\partial V}{\partial q_i} + \frac{\partial R}{\partial \dot{q}_i} = Q_i \tag{2.60}$$

The total kinetic energy of the system is:

$$T = T_1 + T_2 \tag{2.61}$$

where T_1 and T_2 are the kinetic energy of the front and rear parts, respectively, and T_1 is:

$$T_1 = \frac{1}{2}m_1(\dot{X}_1^2 + \dot{Y}_1^2) + \frac{1}{2}I_1\dot{\psi}^2 \tag{2.62}$$

where m_1 and I_1 represent front part mass and moment of inertia, respectively. Assuming small values for θ and ψ, T_2 is:

$$T_2 = \frac{1}{2}m_2[\dot{X}_1^2 + (\dot{Y}_1 - b\dot{\psi} - c\dot{\theta})^2] + \frac{1}{2}I_2\dot{\theta}^2 \tag{2.63}$$

The potential energy of the system V is due to the torsional spring at the articulation joint:

$$V = \frac{1}{2}K_R(\psi - \theta)^2 \tag{2.64}$$

and the dissipation function of the system R is for representing the torsional damper at the articulation joint:

$$R = \frac{1}{2}C_R(\dot{\psi} - \dot{\theta})^2 \tag{2.65}$$

The system is subject to the lateral forces and aligning moments at the tires. For small values of θ and ψ, the total virtual work done by the external forces and moments is:

$$\delta W = F_{y1}\delta(Y_1 + a\psi) + F_{y2}\delta[Y_1 - b\psi - (c+d)\theta] + M_{z1}\delta\psi + M_{z2}\delta\theta \tag{2.66}$$

where F_{y1} and M_{z1} are resultant lateral force (described in $x_1 - y_1$ frame attached to the front part center of mass) and resultant aligning moment at the front, respectively. Therefore, the

41

generalized forces and moments are:

$$Q_Y = F_{y1} + F_{y2} \tag{2.67}$$

$$Q_\psi = aF_{y1} - bF_{y2} + M_{z1} \tag{2.68}$$

$$Q_\theta = -(c+d)F_{y2} + M_{z2} \tag{2.69}$$

Also, regarding the large mass of the vehicle (about 14500 kg), the change in the forward speed due to the longitudinal components of the tire lateral forces can be ignored ($u \approx Const.$). Equation (2.60) can be used to derive the linearized equations of motion (for small deviations) in terms of the defined motion variables. However, a simpler form of these equations with reduced order can be achieved if they are written in terms of the coordinates v, ψ and ϕ, by applying the following equations:

$$\dot{Y}_1 = u\psi + v \tag{2.70}$$

$$\phi = \psi - \theta \tag{2.71}$$

The average slip angle for the front and rear tires, α_1 and α_2, respectively, can be described as:

$$\alpha_1 = -\frac{v + a\dot{\psi}}{u} \tag{2.72}$$

$$\alpha_2 = -\left[\frac{v - b\dot{\psi} - (c+d)(\dot{\psi} - \dot{\phi})}{u} + \phi \right] \tag{2.73}$$

Two variables y_c (lateral coordinate of the front part center of mass in $x_1 - y_1$ frame) and ψ do not appear in the resulting equations of motion, which results in two eigenvalues with zero value (rigid body modes). The following state variables $\mathbf{X}$ can be used to derive the final equations of motion:

$$\mathbf{X} = [v, \dot{\psi}, \dot{\phi}, \phi]^T \tag{2.74}$$

The final form of the equations in terms of the state variables can be considered as a LTI system described by:

$$\dot{\mathbf{X}} = \mathbf{A}\mathbf{X} \tag{2.75}$$

The entries for matrix $\mathbf{A}$ are found in Appendix A. The following solution is assumed for Equation (2.75):

$$\mathbf{X} = [x_1, x_2, x_3, x_4]^T e^{st} \tag{2.76}$$

Therefore, to find the characteristic equation of the system:

$$\det(s\mathbf{I} - \mathbf{A}) = 0 \tag{2.77}$$

then, the resulting characteristic equation is:

$$a_4 s^4 + a_3 s^3 + a_2 s^2 + a_1 s + a_0 = 0 \tag{2.78}$$

Based on the Routh criteria, if the coefficients of this equation meet some specific conditions, the system will be stable. In addition, the real parts of the four eigenvalues of the system (λ_1, λ_2, λ_3 and λ_4) can be plotted in terms of u to reveal the stability. To validate the resulting equations for the 3-DOF model, they are first used to analyze the lateral stability of an articulated steer tractor, which was previously analyzed in [3].

2.4.2 Model Validation

The data for a typical articulated steer tractor is given in Table 2.5. This data was presented in [3], and is used for the stability analysis of this vehicle through the 3-DOF model. The given C_α is an intermediate value, which is computed by the mobility number-based tire model, and represents both a good off-road surface (firm and dry) and a poor road surface (gritty track).

The real parts of the eigenvalues of the system (λ_1, λ_2, λ_3 and λ_4) in terms of the forward speed are shown in Figures 2-11(a) and 2-11(b). The resulting graphs are similar to those shown in [3]. In other words, the equations for the 3-DOF model and those for that model

Parameter	Unit	Value
m_1	kg	1500
I_1	kgm^2	1500
m_2	kg	1500
I_2	kgm^2	1500
a	m	-0.1
b	m	1.3
c	m	1.3
d	m	-0.1
$C_{\alpha 1}$	rad^{-1}	3.4
$C_{\alpha 2}$	rad^{-1}	3.4
$C_{M\alpha}$	m/rad	0
K_R	Nm/rad	5×10^4
C_R	Nms/rad	0

Table 2.5: Parameters of an articulated steer tractor [3].

developed in [3] produce the same eigenvalue results when the aligning moments of the tires are neglected ($C_{M\alpha} = 0$). The real parts of λ_3, λ_4 are negative in the whole range of the operating speeds, according to Figure 2-11(b); however, as shown in Figure 2-11(a), the real parts of λ_1, λ_2, which are complex conjugate numbers with the same real part, are positive for the forward speeds higher than u_{cr} =2.5 m/s, the so-called critical speed. This corresponds to an unstable oscillatory yaw motion or snaking mode for these forward speeds. However, the consideration of the tire aligning moment can effectively change these results because the center of mass positions for the vehicle are near their axles ($a = d = -0.1$ m). For instance, if the aligning moment coefficient $C_{M\alpha}$ increases from 0 to 0.4, the unstable snaking mode of the vehicle will be removed, as illustrated in Figure 2-12. In this case, the real parts of λ_1 and λ_2 are negative in the whole range of the operating speeds, according to Figure 2-12(a).

2.4.3 Effects of Forward Speed

Now, the lateral stability of the baseline vehicle is analyzed in terms of u, based on data given in Table 2.6. To compute the tire forces and moments, instead of the off-road mobility number-based tire model, the Metz tire model is used that has the capability to predict the tire lateral forces for both off-road and on-highway surfaces. To compute the cornering stiffness $C_{F\alpha}$ in Equation (2.11) for finding the front and rear lateral tire forces, two coefficients A and B are required according to Equation (2.33). The coefficient A is given in Table 2.2, and to calculate

44
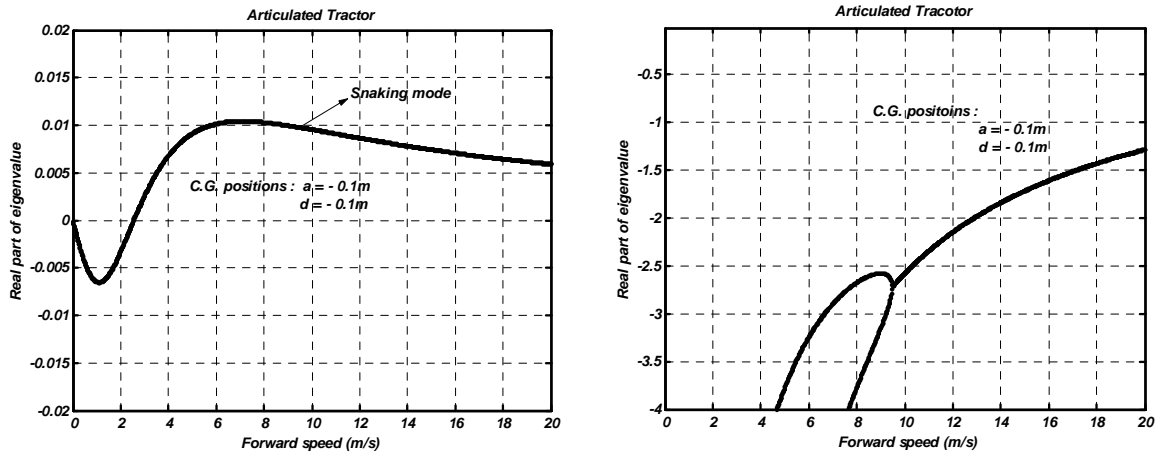
Figure 2-11: Eigenvalue results for articulated steer tractor: (a) λ_1, λ_2 (left graph) and (b) λ_3, λ_4 (right graph) .
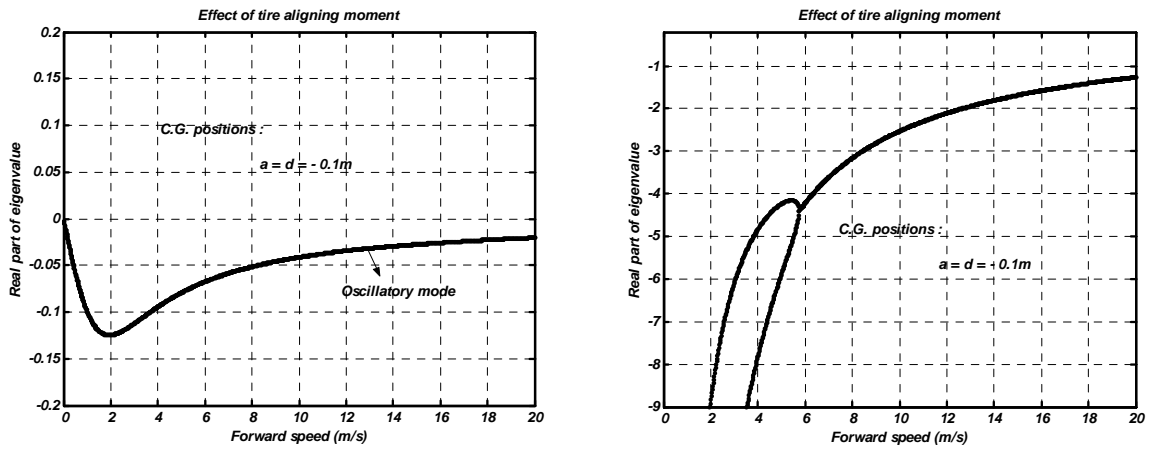
Figure 2-12: Effect of tire self-aligning moment: (a) λ_1, λ_2 (left graph) and (b) λ_3, λ_4 (right graph).

Parameter	Unit	Value	Parameter	Unit	Value
m_1	kg	7280	B_2	1/deg	0.2697
m_2	kg	7280	a	m	0.03
I_1	kgm^2	7280	b	m	1.697
I_2	kgm^2	7280	c	m	1.823
B_1	1/deg	0.2834	d	m	-0.12

Table 2.6: Parameters of baseline vehicle.

B, the coefficients C and D are also given in Table 2.2, and m is equal to 0.14. Based on the manufacturer's data, the tire design load for the baseline vehicle's tires is $F_{ZT} = 72971$ N, which can be used to compute B. The given values of B for the front and rear tires (B_1 and B_2) are computed for an on-highway surface. Then, to compute the aligning stiffness $C_{T\alpha}$ in Equation (2.12), the tire contact length l_t is required according to Equation (2.13). To find l_t, the tire deflection δ_t is required according to Equation (2.14), which can be computed by using the tire vertical stiffness $k_t = 682200$ N/m [35]. To find l_t, in addition to δ_t, the coefficient C_l is required that can be calculated according to Equation (2.15) by using the tire dimensions $d_t = 1.88$ m and $b_t = 0.775$ m. In summary, the computations result in a cornering stiffness of 371050 N/rad and 385435 N/rad for the front and rear tires, respectively, and respective aligning moment stiffnesses of 33163 Nm/rad and 35945 Nm/rad. The center of mass positions are set based on a typical rear-mounted and front-mounted attachment.

For a value of $K_R = 1.1 \times 10^5$ Nm/rad and $C_R = 0$, the real parts of eigenvalues of the system versus forward speed are shown in Figure 2-13. There is a pair of complex conjugate roots with very small real part that dominate the response as depicted in Figure 2-13(a). At lower speeds, the real part of these eigenvalues is negative, and thus, the vehicle is stable. However, the dominant oscillatory roots have a positive real part at forward velocities higher than $u_{cr} =36$ km/h (10 m/s). This means the vehicle will show an undamped oscillatory yaw motion or unstable snaking mode at these speeds. Therefore, the behavior predicted by the 3-DOF model is very close to that observed in practice. As the forward speed u increases, the amplitude of the unstable snaking mode grows at a higher rate. The frequency of this undesirable behavior is 0.9 Hz at $u_{cr} =36$ km/h. When the forward speed increases, this frequency does not increase significantly. There are also two other eigenvalues that have large negative real parts, as plotted in Figure 2-13(b). Although the critical speed of the baseline vehicle and the articulated steer
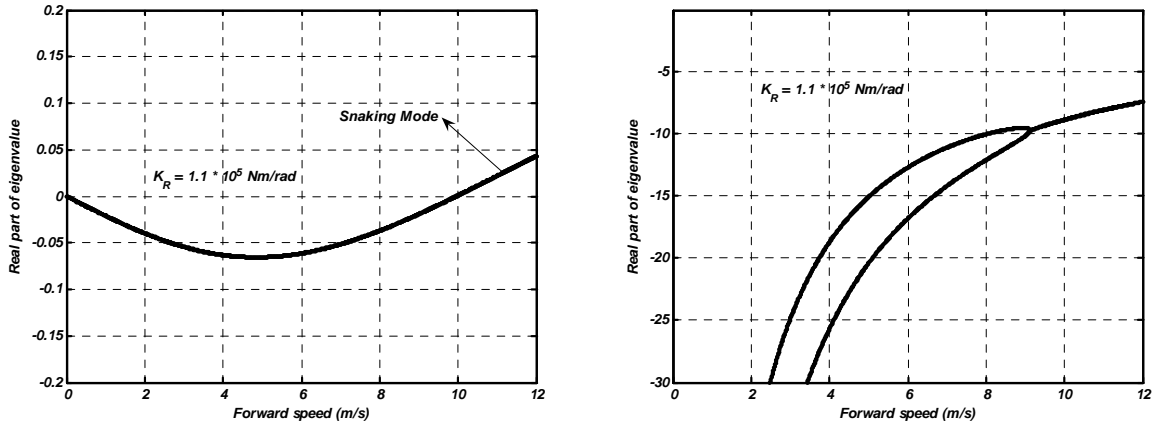
Figure 2-13: Eigenvalue results for baseline vehicle: (a) λ_1, λ_2 (left graph) and (b) λ_3, λ_4 (right graph).

tractor (10 m/s and 2.5 m/s) are different, the eigenvalue results for the two vehicles are similar.

2.4.4   Effects of Steering System Properties

Now, if K_R is increased to 3×10^5 Nm/rad for the baseline vehicle, the real part of the dominant complex roots (λ_1, λ_2) will be negative, as shown in Figure 2-14, which indicates a stable oscillatory yaw motion. The other eigenvalues of the system (λ_3, λ_4) have negative real parts and similar patterns to their previous ones. Also, for $K_R = 1.1 \times 10^5$ Nm/rad, if the torsional damping at the articulation joint is increased to $C_R = 350$ Nms/rad, the vehicle will be stable up to 12 m/s, as plotted in Figure 2-15.

2.5   Simulation of Snaking Mode in ADAMS (12-DOF Model)

To verify the results from the 3-DOF model analysis, the straight-line motion is simulated by using a virtual prototype of the baseline vehicle in ADAMS. ADAMS is a commercial software package used to model and simulate a multi-body system and test the model in an environment similar to that which the actual system will experience [36]. Figure 2-16 shows the virtual prototype built according to the dimensional description and mass properties of the baseline vehicle. The front and rear parts are connected to each other by an articulation joint between
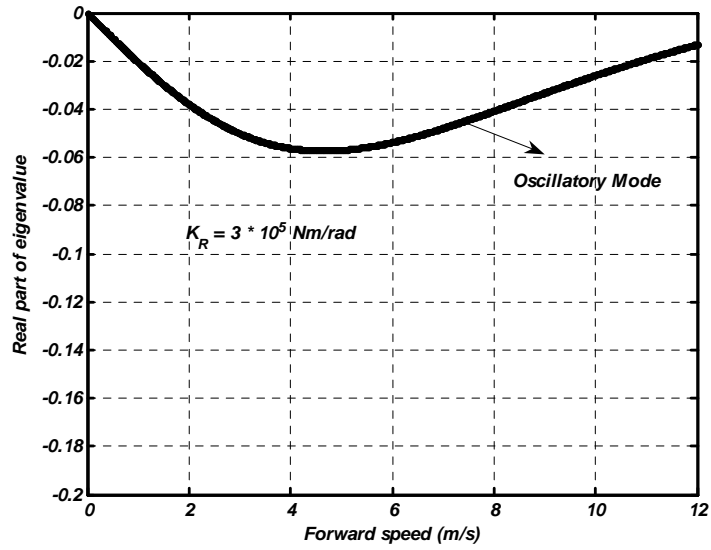
Figure 2-14: Real part of λ_1 and λ_2 for $K_R = 3 \times 10^5$ Nm/rad.
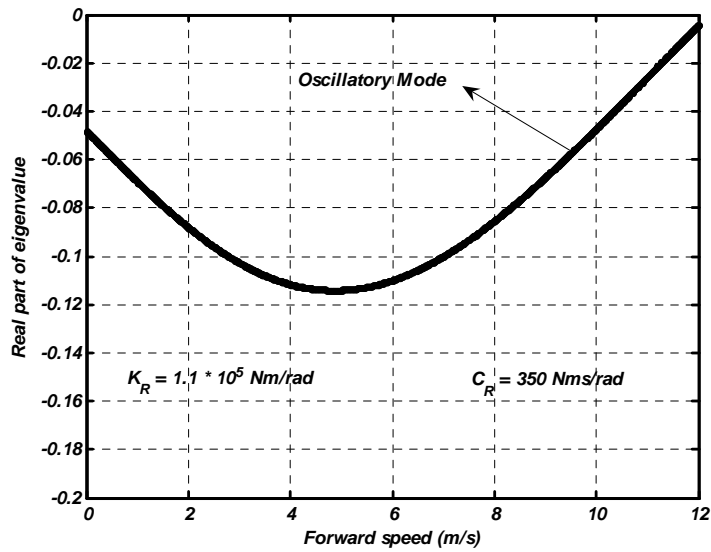
Figure 2-15: Real part of λ_1 and λ_2 for $C_R = 350$ Nms/rad.

them with allowable steering angles of ±45°, by using the two-sided BISTOP contact function of ADAMS. Each part has two wheels rotating on its axle with the wheel mass $m_w = 557$ kg. The front axle is allowed to roll ±15° relative to the front part. The hydraulic cylinders at the articulation joint are represented by a torsional spring and damper, similar to the 3-DOF model. The SAE tire coordinate system is used by default to describe the tire forces and moments in ADAMS. The tire rolling resistance, lateral force, longitudinal force and aligning moment are computed by the Fiala tire model. The Fiala tire model can generate accurate values for lateral force, longitudinal force and aligning moment in response to slip angle and longitudinal slip for different types of tires without the need for tire tests or large storage requirements for look-up tables. In addition, if the equations describing tire forces and moments based on the Fiala tire model are linearized for small deviations, they take the forms similar to those used for the 3-DOF model. For simplicity, the tire longitudinal slip stiffness C_{Fs} and cornering stiffness $C_{F\alpha}$ are assumed to be equal, and the same value as $C_{F\alpha}$ for the 3-DOF model. The value of $\mu_{\max}$ and μ_s are considered for a concrete highway from Table 2.1 ($\mu_{\max} = 0.9$ and $\mu_s = 0.75$). Moreover, the tire vertical load F_z is computed based on the normal deflection of the tire, as follows:

$$F_z = k_t \delta_t + c_t \dot{\delta}_t \tag{2.79}$$

where c_t denotes the tire vertical damping coefficient, which is about 4800 N.s/m [35].

An equal driving torque T_d is applied to the four wheels of the vehicle. The value of T_d is adjusted using a tuned PID (Proportional+Integral+Derivative) control law to move the vehicle with a constant forward speed u. To examine the perturbed motion, after the straight-line motion with constant forward speed begins, a pulsed external torque T_e is applied to the articulation joint, which changes the articulation angle slightly, and then it vanishes. Finally, the articulation angle in response to this disturbing element, which can typically be generated from the movements of the steering wheel by the operator, is plotted.

2.5.1 Effects of Steering System Properties

For the first step, the rolling resistance is neglected similar to the 3-DOF model. Therefore, the driving torque T_d will be zero at the steady-state. The perturbed motion of the vehicle with the
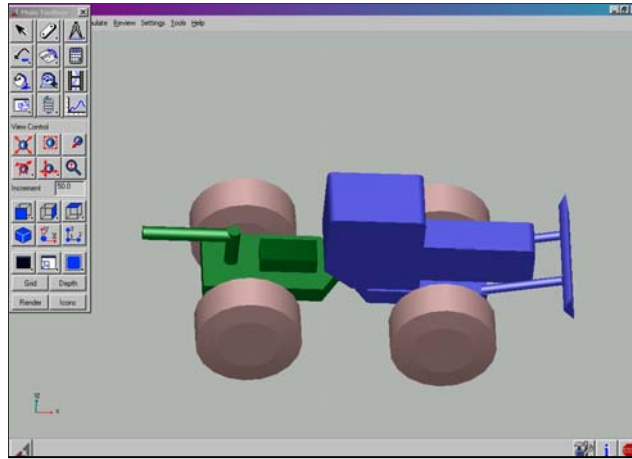
Figure 2-16: Virtual prototype of baseline vehicle in ADAMS.

critical speed predicted by the 3-DOF mode ($u_{cr} = 10$ m/s, see Figure 2-13), $C_R = 0$ and $K_R = 1.1 \times 10^5$ is simulated. As shown in Figure 2-17, the response is an undamped oscillatory yaw motion, or snaking mode, as predicted by the 3-DOF model. The frequency of the resulting oscillatory motion is 0.8 Hz at $u_{cr} = 36$ km/h, which is very close to that predicted by the 3-DOF model (0.9 Hz). For $K_R = 3 \times 10^5$ Nm/rad, the vehicle is stable at this forward speed, as depicted in Figure 2-18. The response is a damped oscillatory mode, as predicted by the 3-DOF model for this value of K_R (see Figure 2-14). Figure 2-19 shows the articulation angle for the perturbed motion with $u = 10$ m/s, $K_R = 1.1 \times 10^5$ Nm/rad and $C_R = 350$ Nms/rad. The response is a damped oscillatory mode, as predicted by the 3-DOF model and the vehicle is stable at this velocity (see Figure 2-15). Therefore, for the negligible rolling resistance and small deviations, the results from the simulations and the 3-DOF model are reasonably consistent.

Now, a typical value of 0.017 is considered for the tire rolling resistance coefficient C_{rr} on concrete. In this case, the driving torque T_d will be non-zero at the steady-state. The response of the system is again shown in Figure 2-20 for $K_R = 1.1 \times 10^5$ Nm/rad and $C_R = 0$. The response is a damped oscillatory yaw motion, which is different from that shown in Figure 2-17. This difference is due to the fact that the change in v during the perturbed motion leads to a small change in the roll motions of the rear and front parts. Therefore, the normal load F_z at the left and right wheels of a given axle will be slightly different. This leads to the different
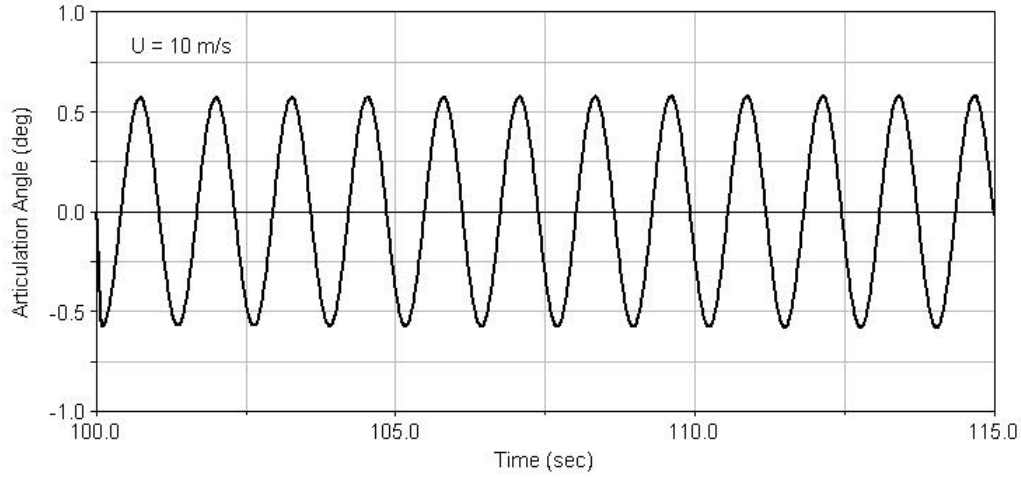
Figure 2-17: Change in articulation angle for $K_R = 1.1 \times 10^5$ Nm/rad.

rolling resistance F_r at the left and right wheels because F_r is dependent on F_z. Therefore, the resulting moment produced by these different rolling resistances will introduce a stabilizing effect similar to increasing the torsional damping.

2.5.2 Effects of Front and Rear Tire Properties

The dynamic behavior of the virtual prototype in ADAMS is nonlinear, and thus, for the larger deviations, the response may be slightly different from that predicted by the 3-DOF model. For instance, as shown in Figure 2-14, the baseline vehicle is stable at $u = 12$ m/s, for the torsional stiffness $K_R = 3 \times 10^5$ Nm/rad and $C_R = 0$, based on the 3-DOF model analysis. Although the real part of the dominant eigenvalues is very close to zero, it is still negative, indicating a very slowly-damped oscillatory yaw motion. However, for the virtual prototype of the vehicle for the larger perturbation, the response is an undamped oscillatory yaw motion, as plotted in Figure 2-21. The undamped oscillations start because the external torque T_e makes a larger change in the articulation angle as the initial condition for this simulation. Therefore, the nonlinear effects, for instance due to tire forces and moments, appear and lead to the undamped oscillations, instead of very slowly-damped oscillations.

To obtain insight into the dynamic behavior during the snaking mode, some results are
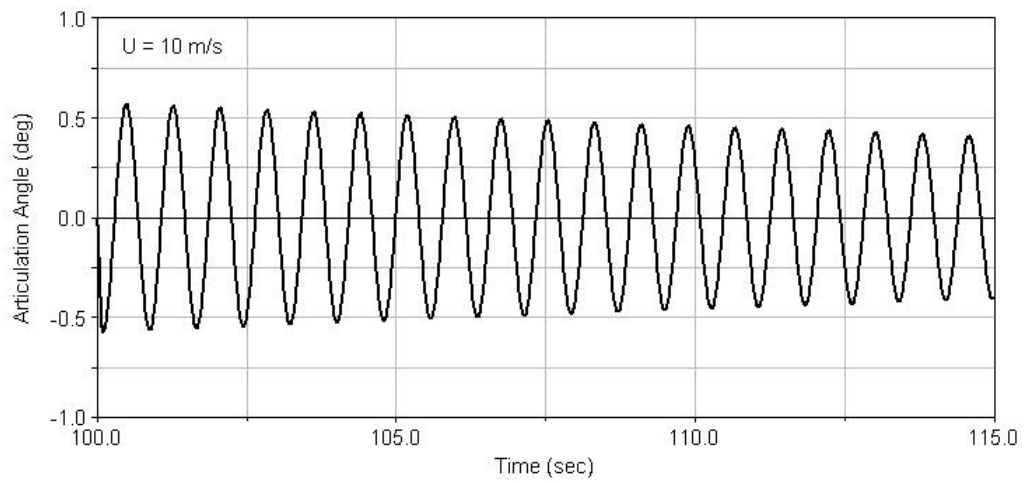
Figure 2-18: Change in articulation angle for $K_R = 3 \times 10^5$ Nm/rad.
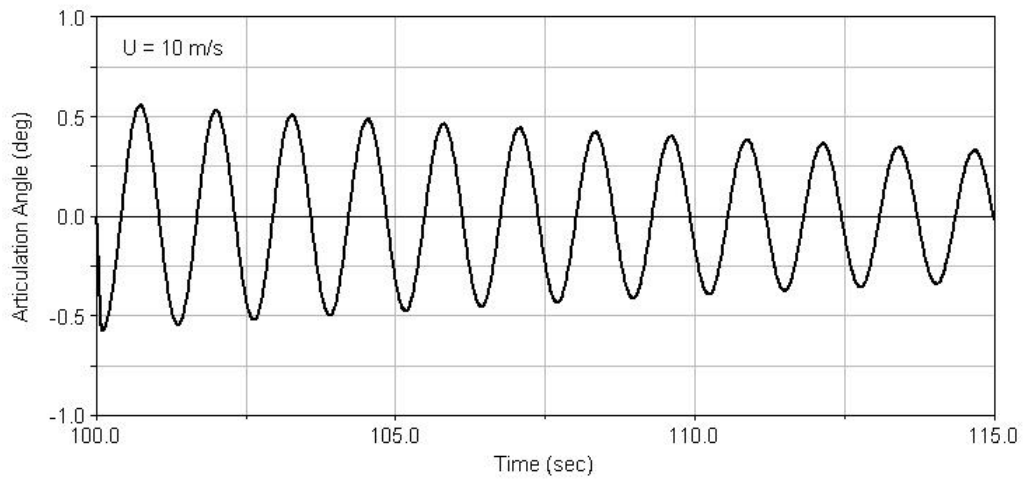
Figure 2-19: Change in articulation angle for $K_R = 1.1 \times 10^5$ Nm/rad and $C_R = 350$ Nms/rad.
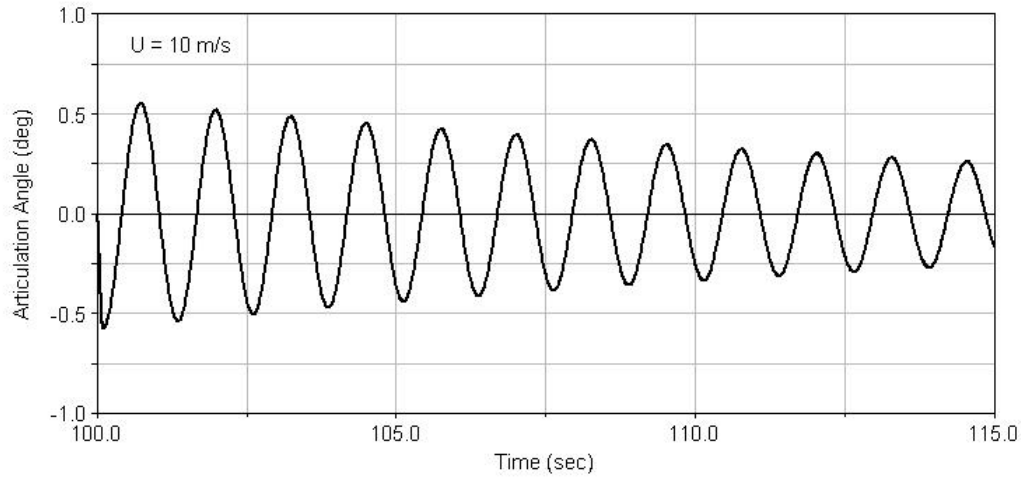
Figure 2-20: Change in articulation angle for $K_R = 1.1 \times 10^5$ Nm/rad and $C_R = 0$ with considering rolling resistance.

examined for this simulation. The slip angles of the left and right front tires are plotted in Figure 2-22. These angles are very similar for the left and right tires (solid and dotted lines). The slip angles are also close to each other for the left and right rear tires (solid and dotted lines), as illustrated in Figure 2-23. However, the magnitude and sign of the slip angles at the rear tires and front tires are different. This will result in different lateral tire forces at the front and rear. The lateral tire force of the left front and left rear tires are graphed in Figure 2-24. These forces are different, as expected. The longitudinal forces of these tires are also plotted in Figure 2-25, which shows that the longitudinal tire forces are much smaller than the lateral tire forces. The aligning moment of the left front tire is also shown in Figure 2-26. In general, the front and rear resultant lateral tire forces have significant effects on the dynamic behavior during the snaking mode.

The lateral force produced at the tires is dependent on their cornering stiffness. Therefore, when the cornering stiffness of the front or rear tires changes, the dynamic behavior will change during the snaking mode. This change in the cornering stiffness can be a result of change in the tire properties such as construction, size and inflation pressure [37]. Even for a given size and type, tires produced by different manufacturers have a standard deviation of about 15 percent on cornering stiffness. The change in the cornering stiffness caused by using the tire properties

53
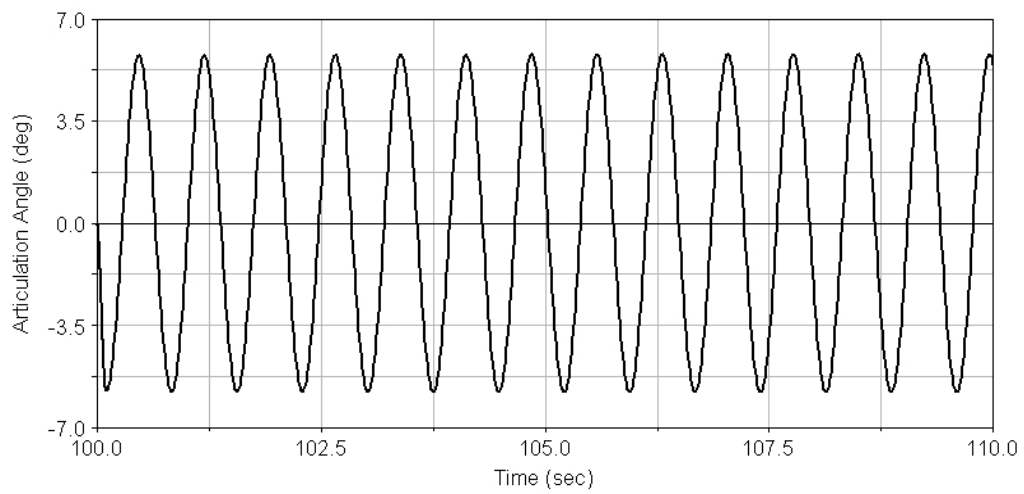
Figure 2-21: Oscillatory behavior of articulation angle in response to an external disturbance, $u = 12$ m/s.
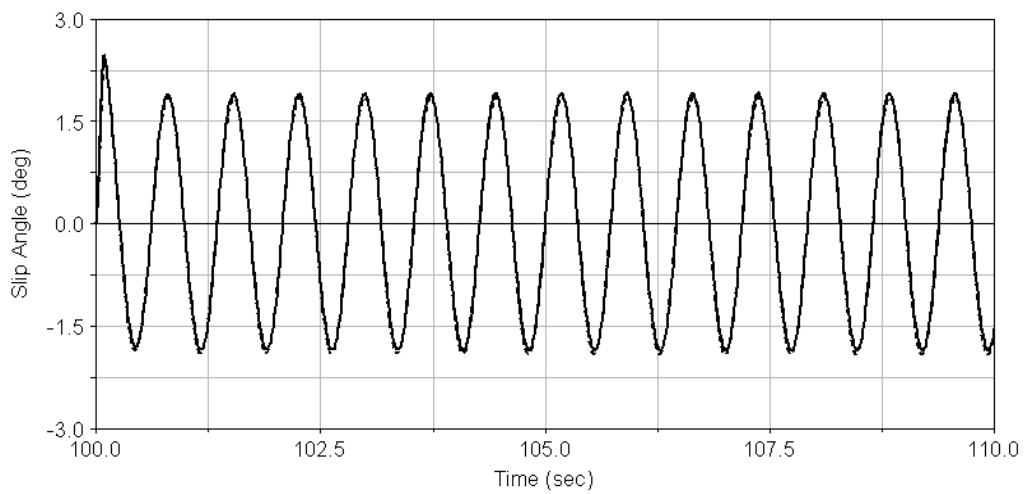
Figure 2-22: Slip angles of left and right front tires during snaking mode.

54
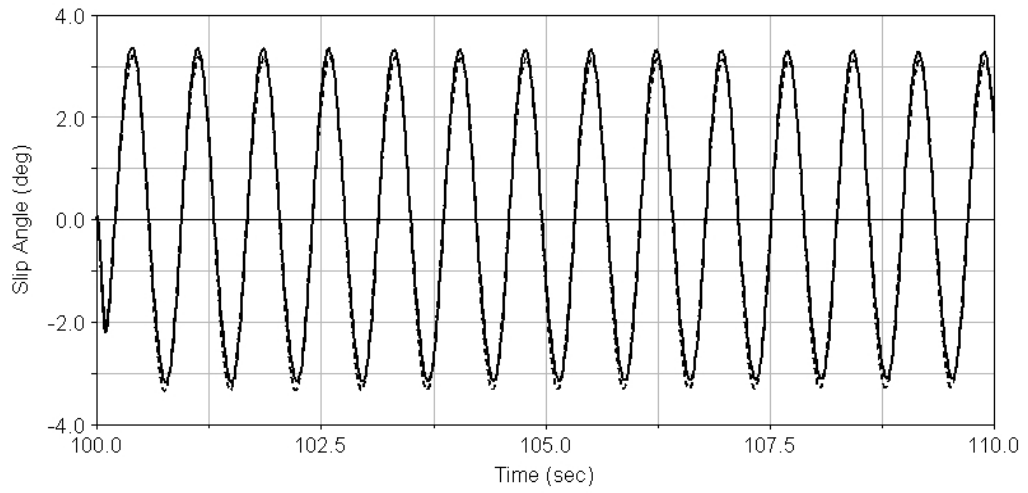
Figure 2-23: Slip angles of left and right rear tires during snaking mode.
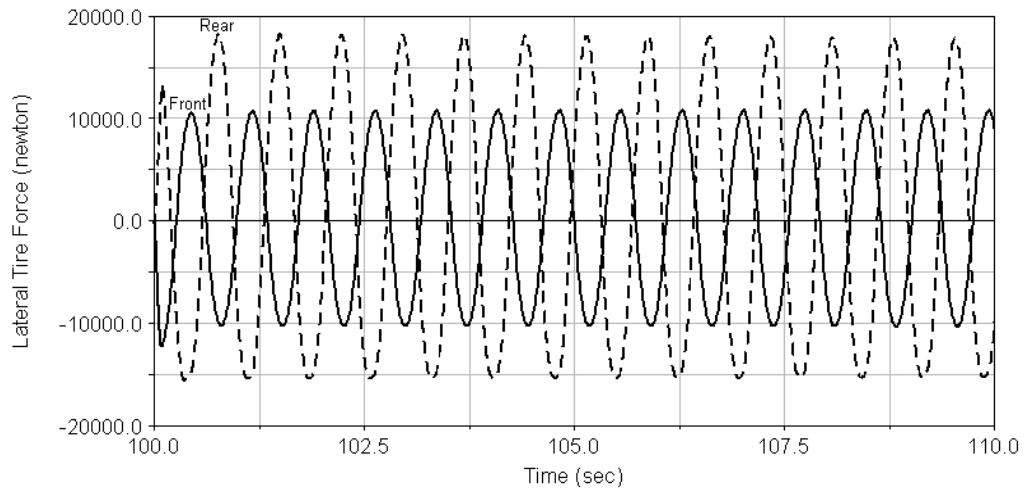
Figure 2-24: Lateral forces of left front and rear tires.
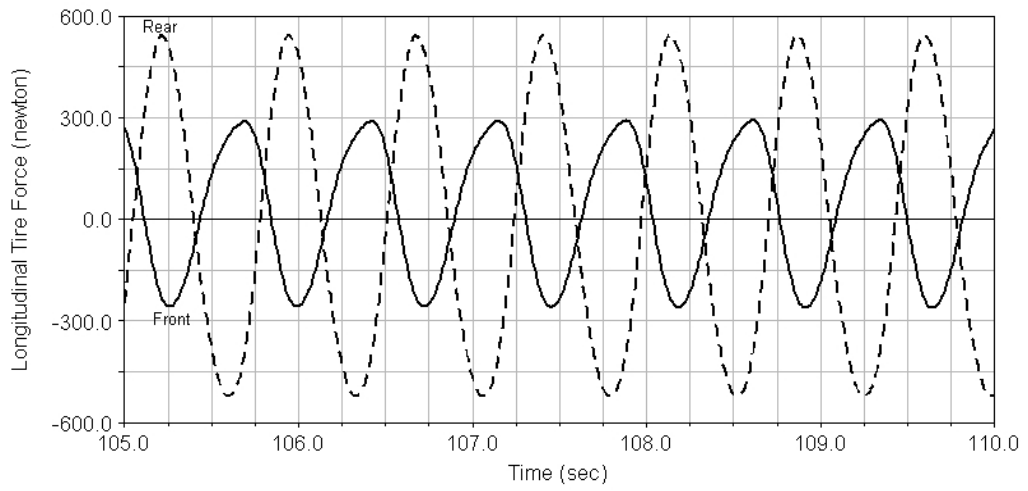
Figure 2-25: Longitudinal forces of left front and rear tires.
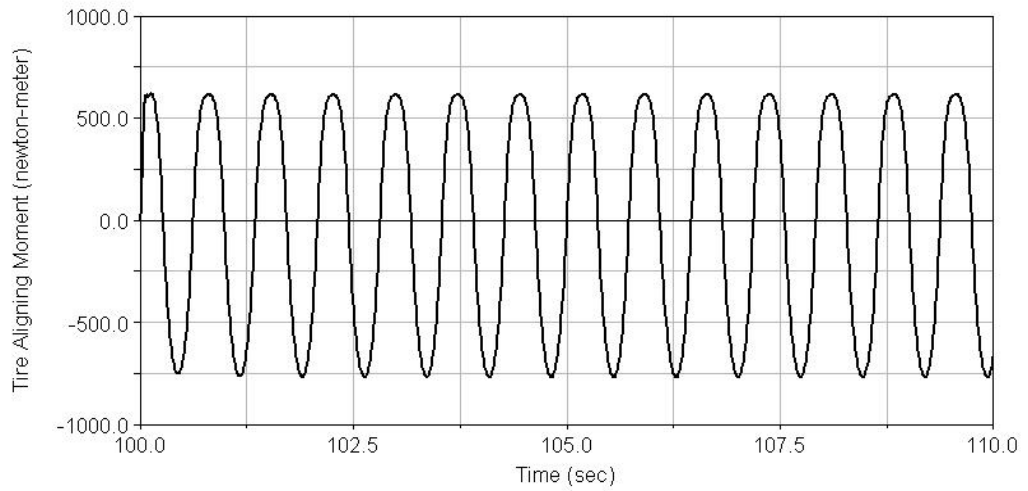
Figure 2-26: Aligning moment of left front tire.

56
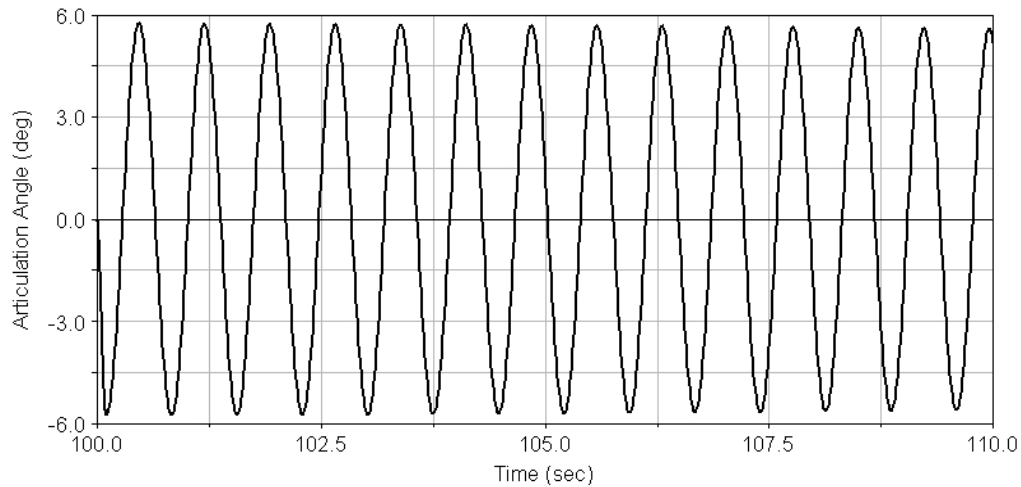
Figure 2-27: Damped oscillatory behavior by increasing $C_{F\alpha}$ at front tires.

has been used by designers to improve lateral stability and handling behavior of wheel steer vehicles. As an example, some wheel steer vehicles, such as sports and performance cars, have in common rear tires that are wider than those in front. The wider tires at the rear result in an increase in the cornering stiffness to induce an understeer effect on the handling behavior. A similar effect can be achieved by using tires with unequal pressures and section heights in the front and rear.

Now, if $C_{F\alpha}$ for the front tires increases by 10 percent of the nominal value, the articulation angle will change according to Figure 2-27. The response is a damped oscillatory yaw motion, and the vehicle is stable. However, the snaking oscillations are damping out very slowly. The articulation angle for 10 percent decrease in $C_{F\alpha}$ for the rear tires is shown in Figure 2-28. This is possible, for instance, by using narrower tires at the rear. The response is again a damped oscillatory yaw motion, but the snaking oscillations are decreasing at a higher rate compared with the previous case. The articulation angle for 10 percent decrease in the cornering stiffness of the rear tires and 10 percent increase in the cornering stiffness of the front tires is shown in Figure 2-29. The response is very close to that of the previous example.
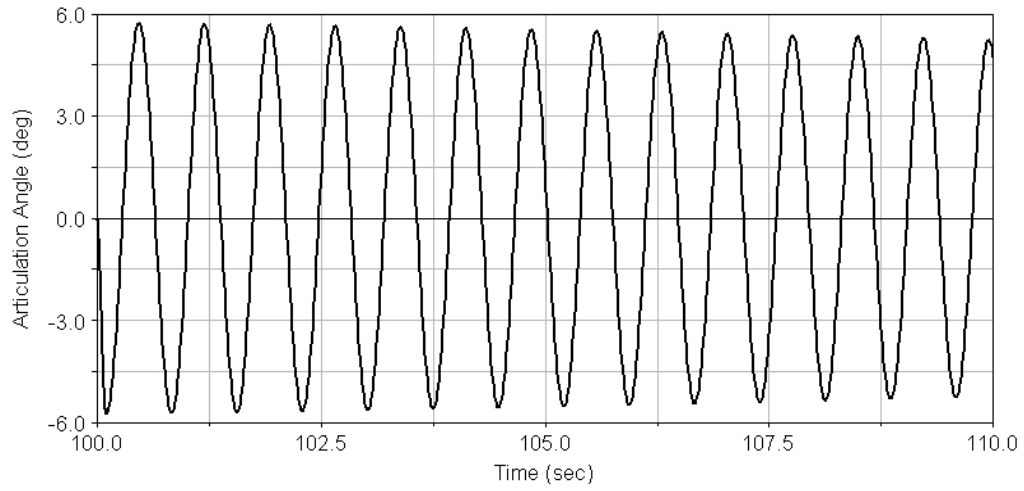
Figure 2-28: Damped oscillatory behavior by decreasing $C_{F\alpha}$ at rear tires.
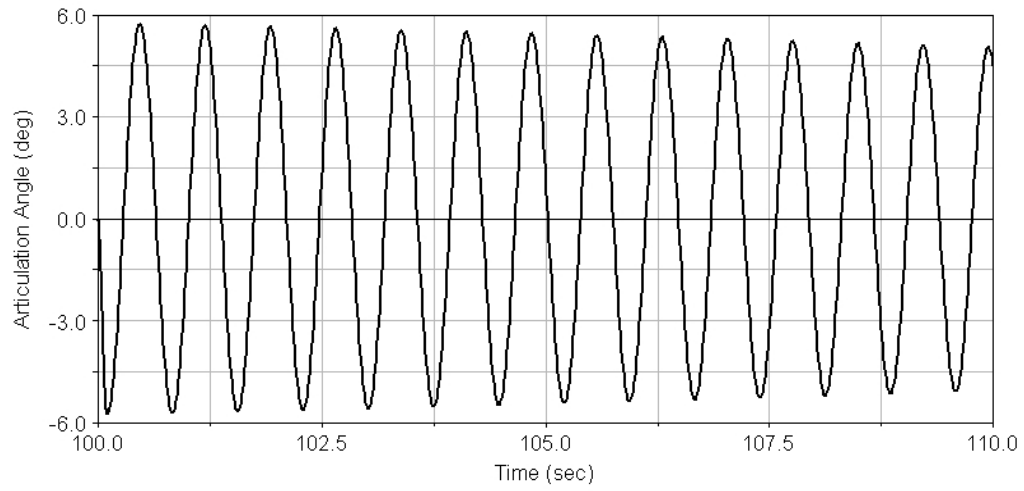
Figure 2-29: Damped oscillatory behavior by decreasing $C_{F\alpha}$ at rear tires and increasing $C_{F\alpha}$ at front tires.

2.6   Summary

A comprehensive study of the lateral stability of an ASV during the snaking mode was conducted to identify the causes of the instability. First, several stability analyses based on simplified models of the vehicle, including 1-DOF and 3-DOF, were performed. These models were developed using models of the subsystems, including tire and steering system. The modeling of tires, using linearization and mobility number, as well as Fiala and Metz methods, was described. The commonly-used steering systems for ASVs, including hydrostatic and hydraulic-mechanical, were reviewed. In view of the pressure-flow equation for these steering systems, a torsional spring and damper at the articulation joint were used to represent the steering system characteristics. The simplified models were used to analyze stability in straight-line travel with different forward speeds, based on the characteristic equation and eigenvalues. The analysis of the 1-DOF model for the baseline vehicle indicated no lateral instability, but showed that increasing the forward speed results in an oscillatory yaw motion with lower damping ratio. The eigenvalue results for the 3-DOF model were validated based on the results reported in [3] for an articulated steer tractor. The analysis of the 3-DOF model for the baseline vehicle showed an unstable oscillatory yaw motion or snaking mode for the forward speeds higher than u_{cr} =10 m/s. Also, these investigations reveal that the effects of higher speeds on the lateral stability of ASVs are remarkable.

The effects of the steering system characteristics on the stability were also examined. The additional energy given to the vehicle that could result in the instability during the snaking mode must be absorbed by the torsional stiffness, or it should be dissipated by the torsional damping. Therefore, the instability of an ASV occurred when the torsional stiffness and damping, which result from the steering system characteristics, were at low levels. An increase in the torsional stiffness or torsional damping can alleviate the snaking oscillations. These studies show that the design of the articulated frame steering system that controls the articulation angle is more critical than design of steering system for front wheel steer vehicles. This is due to the fact that the steering system of an ASV has two different functions, ensuring both maneuverability and lateral stability.

To verify the results predicted by the 3-DOF model, the motion of a virtual prototype of the vehicle in ADAMS was simulated for different conditions. The comparisons show that

the results from the simulations and stability analyses by the 3-DOF model are reasonably consistent. Therefore, the 3-DOF model can be used to obtain a considerable insight into basic aspects of the lateral stability of an ASV during the snaking mode for different conditions. The effects of the tire rolling resistance on the stability during the snaking mode were also examined by the simulations. A stabilizing yaw moment was generated by changes in the rolling resistance at the right and left tires of a given axle. This effect on the stability is equivalent to increasing the torsional damping at the articulation joint. In addition, the results show that the interaction of the lateral forces of the front and rear tires dominate the response during the snaking mode. Therefore, by making some changes in the cornering stiffness of the tires at the front or rear, the response of the vehicle will change. The studies show that when the cornering stiffness of the rear tires is reduced, the snaking oscillations will also be alleviated. The cornering stiffness of these tires can be reduced by changing the tire construction or dimensions; for instance, narrower tires have less cornering stiffness.

Chapter 3

Effects of Vehicle Parameters and Operating Conditions on Stability

ASVs are utilized to do different tasks on various surfaces. They are used to carry distinct values of loads at the front and rear, which may have interaction with ground. To do their functions, they are equipped with several changeable front and rear-mounted attachments, the configuration of which can change considerably. All of these factors affect the vehicle parameters, such as mass properties and center of mass positions, for both the front and rear parts. The operating condition is also changing for an ASV, similar to any other road vehicle. An ASV is required to travel on different soft and hard surfaces, such as soils, gravel and highways during a working cycle. It can travel in a straight-line or in a turning motion, with constant forward speed or with acceleration. Moreover, ASVs with permanent four-wheel drive configuration are usually equipped with differential locks on their front and rear axles. When more total traction is required, for instance on soft surfaces or for carrying loads, differentials can be locked. ASVs are also used to carry a rear-mounted load or attachment that interacts with the ground. For instance, forestry skidders are used to transport logs or tractors are equipped with a long plough.

When the baseline vehicle parameters or its operating condition change, the lateral stability during the snaking mode is affected. In this section, the effects of these changes on stability are studied. Some of these analyses are conducted by using the 3-DOF model. However, this model

is not suitable to study the effects of either locking differentials or of carrying a load which has interaction with the ground. For these cases, the 3-DOF model is extended to a 5-DOF and 4-DOF model to complete the analyses. Most of the materials of this chapter were previously published in [38, 39, 40].

3.1 Operation with Different Mass Distributions

The baseline vehicle, a forestry skidder, can be equipped with different types of front and rear-mounted attachments, such as a dozer and grapple. These attachments can considerably change the mass and moment of inertia for both the front and rear parts. Also, the configuration of these attachments may be changed by the operator, resulting in changes in the rear or front part center of mass positions. As an example, the rear grapple of the baseline vehicle in its full reach position represents a long rear-mounted attachment, which increases the moment of inertia for the rear part considerably. By using the 3-DOF model, the effects of these changes on stability during the snaking mode can be studied, as described in the following sections.

3.1.1 Front and Rear Center of Mass Position

As mentioned previously, conventional ASVs are typically designed in such a way that their front and rear part center of mass positions are located near their respective axles. Assuming these center of mass positions for the baseline vehicle ($a = d = 0$, $b = 1.727$ m and $c = 1.703$ m), even if both K_R and C_R are zero, the baseline vehicle will be stable over a range of forward speeds up to and beyond 20 m/s during on-highway travel. This result is based on observing the real parts of the eigenvalues (λ_1, λ_2, λ_3 and λ_4) for different forward speeds, as shown in Figure 3-1. The real parts of all eigenvalues are negative, and thus, the vehicle is always stable. The mass properties are the same as those used in Chapter 2 (Table 2.6), and the tire parameters are calculated based on the Metz tire model.

The previous work shows that the snaking mode may occur when there is a shift in the rear part center of mass position rearward of the rear axle [3]. For the baseline vehicle, this is shown in Figure 3-2 by setting $a = 0$ and $d = -0.5$ m. The system will have a pair of complex conjugate eigenvalues with positive real parts for $K_R = 1 \times 10^5$ Nm/rad and $C_R = 0$, over
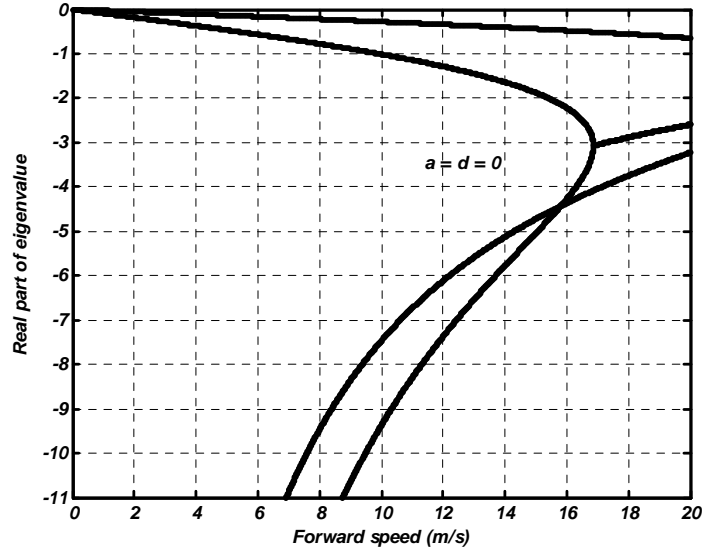
Figure 3-1: Eigenvalue results for $a = d = 0$.

the given range of the forward speeds. This means the vehicle will show the oscillatory yaw instability for this rear part center of mass position at any forward speed.

A change in the configuration of a front-mounted attachment may also shift the front part center of mass position forward of the front axle. This may cause the unstable snaking mode, as shown in Figure 3-3 for $a = -0.5$ m, $d = 0$, $K_R = 1 \times 10^5$ Nm/rad, $C_R = 0$ and forward speed higher than $u_{cr} = 16.5$ m/s (about 60 km/h). Therefore, in addition to the well-backward center of mass positions for the rear part, the well-forward center of mass positions for the front part may also lead to the unstable snaking mode if the vehicle moves at considerably high speeds. However, the well-backward center of mass positions for the rear part result in the unstable snaking mode even at lower forward speeds.

To identify the significant effects of the center of mass positions on the stability during the snaking mode, another analysis is conducted. As shown before, the equivalent torsional stiffness at the articulation joint K_R is determined based on the steering system characteristics. For a given C_R, only when this stiffness is less than a minimum value, the unstable snaking mode will occur. For $C_R = 0$, the minimum torsional stiffness K_{cr} to stabilize the baseline vehicle up to $u = 20$ m/s can be used to determine the effects of different values of the rear and front center

63
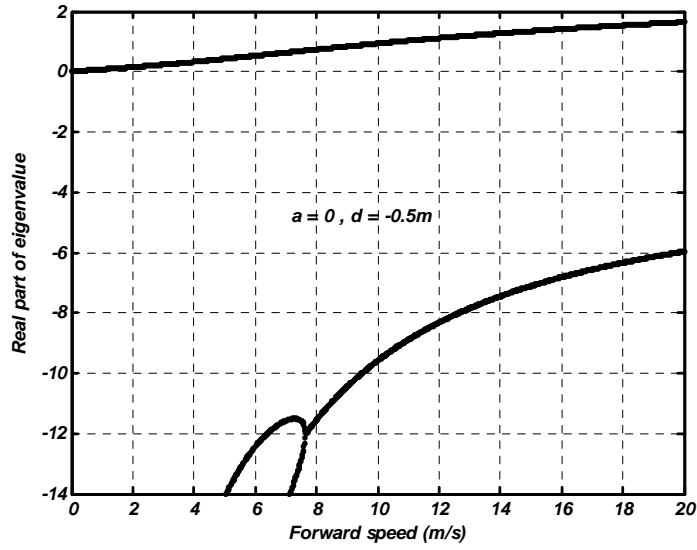
Figure 3-2: Eigenvalue results for $a = 0$ and $d = -0.5$ m.
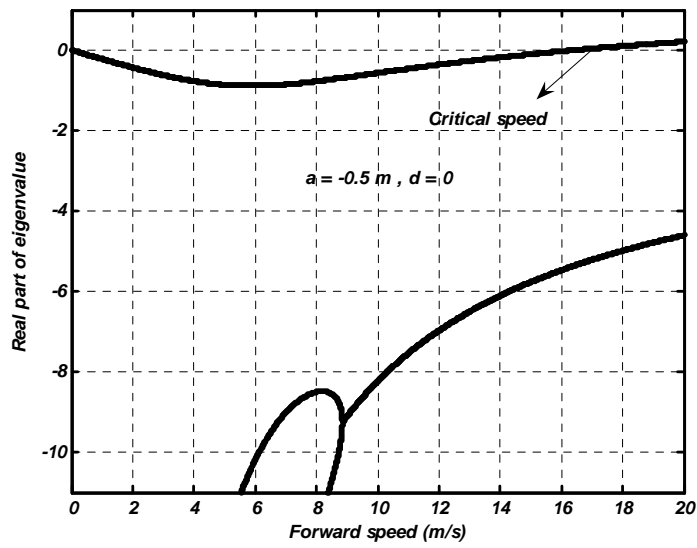
Figure 3-3: Eigenvalue results for $a = -0.5$ m and $d = 0$.
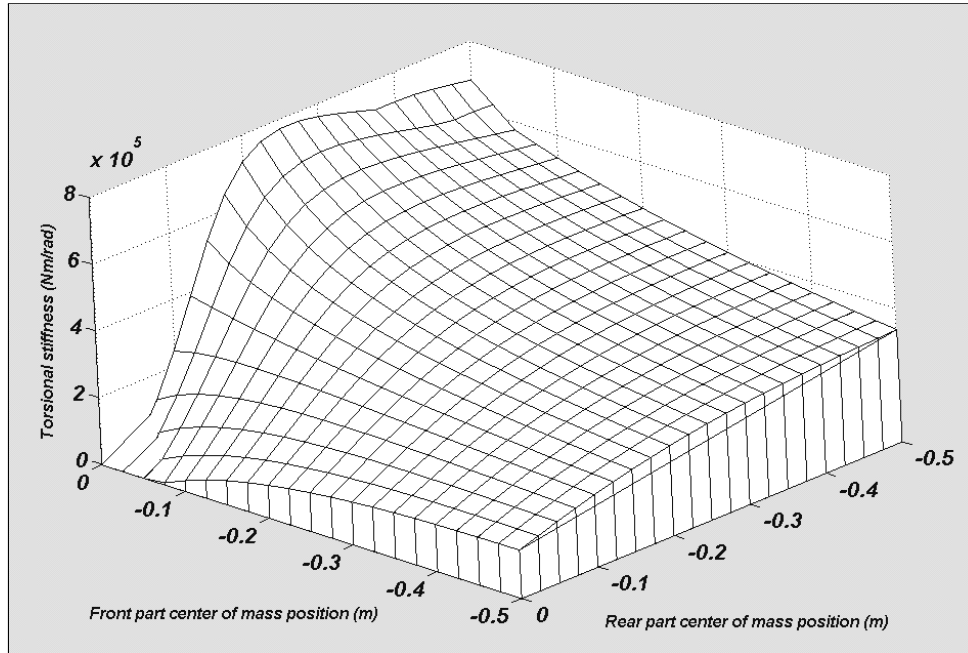
Figure 3-4: Critical torsional stiffness for various center of mass positions.

of mass positions on the stability. The critical torsional stiffness K_{cr} is calculated by examining the eigenvalues of the system for any case. The value of K_{cr} is shown in Figure 3-4 for various combinations of the front and rear parts center of mass positions. The order of magnitude for K_{cr} changes when the variations are introduced to the center of mass positions. Also, this plot clearly implies the important effect of the rear part center of mass position to promote instability during the snaking mode, compared with the front part center of mass position.

3.1.2 Front and Rear Part Mass

When a front or rear-mounted attachment is loaded, the mass of the front or rear part will change. To identify the effects of change in the front and rear part masses on stability during the snaking mode, an analysis based on K_{cr} is conducted. For the rear part center of mass position $d = -0.5$ m, the critical torsional stiffness K_{cr} is shown in Figure 3-5 for some changes in the rear part mass. Based on this graph, the maximum increase in the rear part mass is: $\frac{10000-7280}{7280} \times 100 = 37$ percent. This maximum change in the rear part mass results in a decrease of 11 percent in K_{cr}. For the front part center of mass position $a = -0.5$ m, the critical torsional
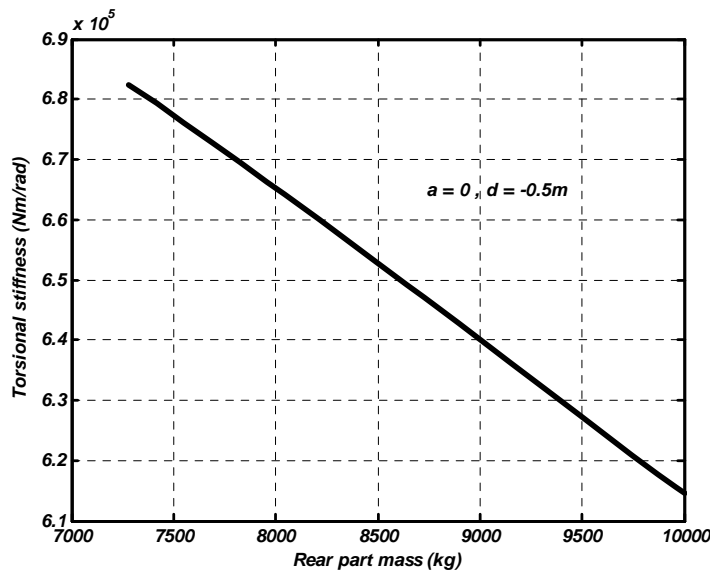
Figure 3-5: Critical torsional stiffness for different values of rear part mass.

stiffness K_{cr} is shown for the different values of the front part mass in Figure 3-6. This plot shows that an increase of 37 percent in the front part mass only changes about one percent in K_{cr}. Comparing Figures 3-5 and 3-6 also shows that K_{cr} for stabilizing the vehicle with a front-mounted attachment is considerably less than that with a rear-mounted attachment.

3.1.3   Front and Rear Part Moment of Inertia

The configuration of a front or rear-mounted attachment may change considerably. This may introduce a large change in the moment of inertia, but the mass remains constant. To identify the effects of these changes on the stability, a similar analysis is conducted. For the rear part center of mass position $d = -0.5$ m, K_{cr} for the different values of the rear part moment of inertia is shown in Figure 3-7. This graph indicates that an increase of 37 percent in the rear part moment of inertia increases 19 percent in K_{cr}. Therefore, the effect of the rear part moment of inertia is opposite of that for the rear part mass. For the front part center of mass position $a = -0.5$ m, K_{cr} is also shown for the different values of the front part moment of inertia in Figure 3-8. This plot indicates that an increase of 37 percent in the front part moment of inertia decreases 41 percent in K_{cr}.

66
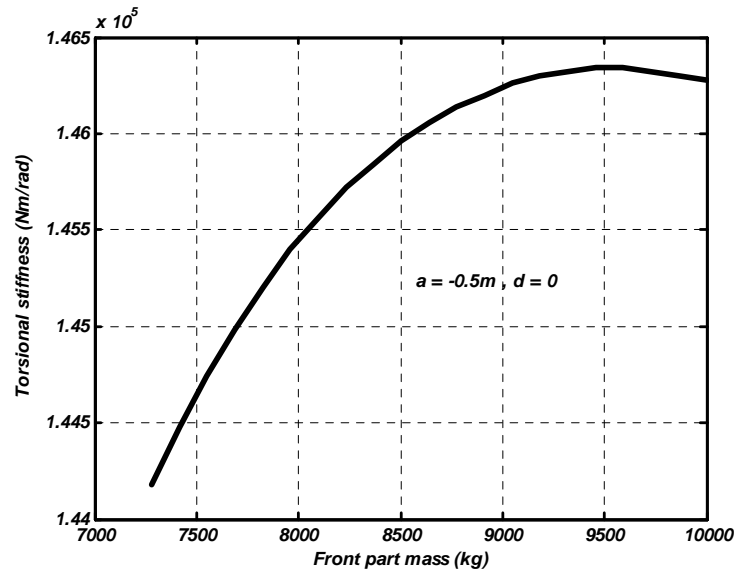
Figure 3-6: Critical torsional stiffness for different values of front part mass.
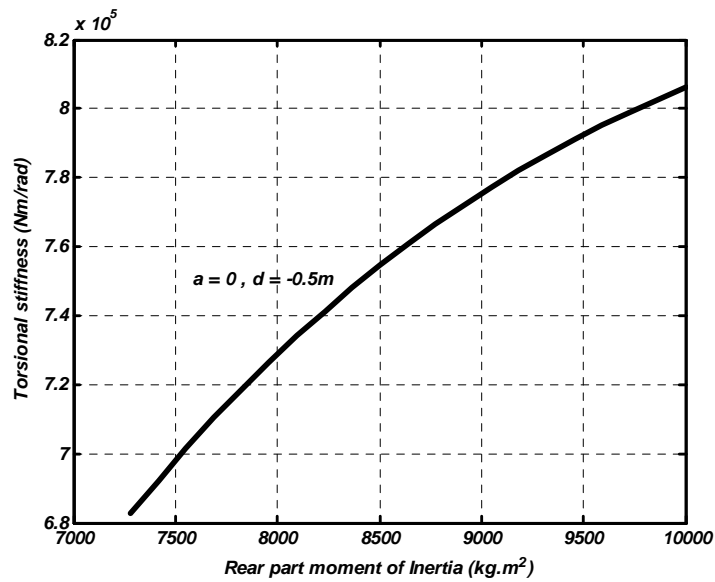
Figure 3-7: Critical torsional stiffness for different values of rear part moment of inertia.
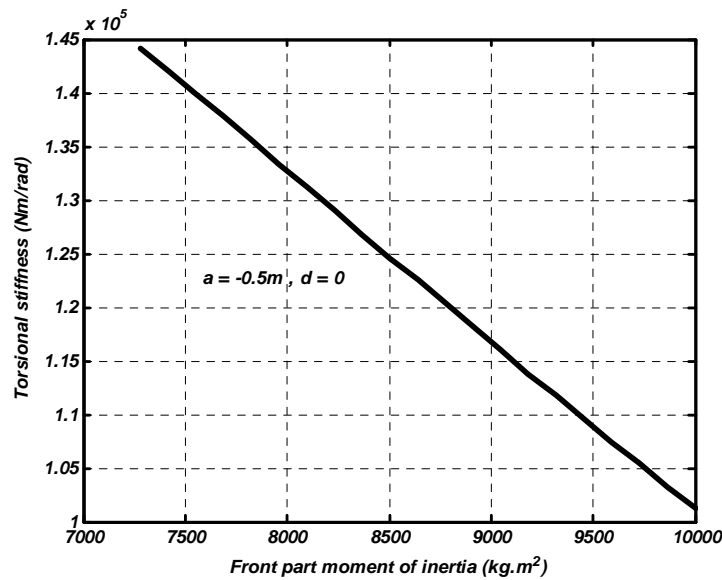
Figure 3-8: Critical torsional stiffness for different values of front part moment of inertia.

3.2   Operation on Different Road Surfaces

An ASV moves on different road surfaces during its operation. The rolling resistances of tires are smaller during on-highway travel and the vehicle can also move at higher speeds. Therefore, regarding the effects of forward speed and rolling resistance on stability, which was discussed previously, the unstable snaking oscillations are more likely during on-highway travel. For this reason, the previous analyses were conducted for travel on a highway surface. However, on a reasonably good off-road surface covered with gravel, the vehicle may be able to travel at higher speeds. For this condition, as an example, K_{cr} for different values of the rear part mass is shown in Figure 3-9. The tire properties for gravel surface are computed based on the Metz model. Comparing Figures 3-5 and 3-9 shows that the change in K_{cr} for the different values of the rear part mass is similar for gravel and highway surfaces. However, the stabilization during the on-highway travel requires more torsional stiffness, although the difference in K_{cr} is not significant (about 14 percent). This is due to the fact that the on-highway tire cornering stiffness is higher than that for a surface covered with gravel. Therefore, the lateral force produced at the tires is larger on highway surface. As shown before, the interaction of the lateral tire forces produced

68
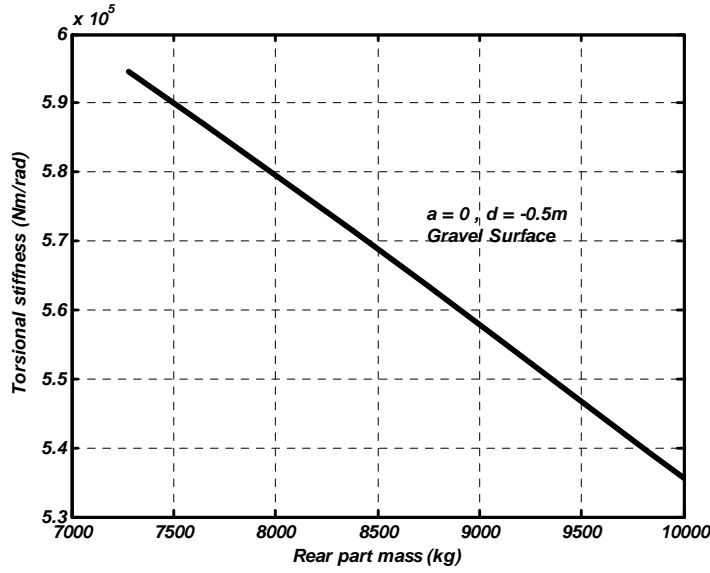
Figure 3-9: Critical torsional stiffness for different values of rear part mass on gravel surface.

at the front and rear has an important effect on the stability during the snaking mode. When there is a significant difference between the values of the resultant lateral force at the rear and front, the snaking oscillations are stronger, which is the case during on-highway travel.

3.3   Operation with Forward Acceleration

Regarding the large mass of ASVs (e.g. 14500 kg for the baseline vehicle), the forward acceleration of these vehicles is generally low. Therefore, the analysis of the lateral stability with the assumption of the constant forward speed can be extended for the travel with forward acceleration by some minor modifications. Applying driving torques for acceleration to the four wheels of an ASV results in additional tractive force at the tires. This is shown for the 3-DOF model in Figure 3-10, in which the tractive force is shown at the four tires. The virtual work done by the tire tractive forces which is related to ψ and θ can be represented by δW_l as follows:

$$\delta W_l = [(F_{x1} - F_{x2})\delta\psi + (F_{x3} - F_{x4})\delta\theta]\frac{w_t}{2} \tag{3.1}$$

69

where w_t is the wheel track, and F_{x1}, F_{x2}, F_{x3} and F_{x4} are tire tractive forces at the front and rear. The tractive tire force on the left and right tires is normally the same:

$$F_{x1} = F_{x2} \tag{3.2}$$

$$F_{x3} = F_{x4} \tag{3.3}$$

Therefore, according to Equation (3.1), there is no effect on the lateral and yaw motion of the vehicle due to the tire tractive forces. ASVs have a large wheelbase (e.g. $a + b + c + d = 3.43$ m for the baseline vehicle), which causes less pitch motion, and thus, less longitudinal load transfer for smoother driving. Therefore, the change in the cornering stiffness of the tires due to the change in the normal force at the front and rear is not significant. However, when tractive force is present at a tire, the cornering force capability reduces [37]. If the tractive force is high, the cornering stiffness of the tire decreases significantly. This effect changes the handling characteristics of conventional wheel steer vehicles. For instance, for a wheel steer vehicle with rear-wheel drive configuration, applying traction force to the rear wheels decreases the cornering stiffness of these tires, which results in an oversteering effect. However, for a front-wheel drive vehicle, applying traction force to the front wheels will cause an understeering effect [23]. To describe the effect of tire tractive force F_x on the cornering stiffness $C_{F\alpha}$, the friction ellipse model described by Equation (2.30) is written in a modified form. For a given slip angle α and tire normal load F_z, this model can be described by the following equation:

$$\left(\frac{C_{F\alpha}}{C'_{F\alpha}}\right)^2 + \left(\frac{F_x}{F_{x\,\text{max}}}\right)^2 = 1 \tag{3.4}$$

where $F_{x\,\text{max}}$ shows the maximum longitudinal tire force, and $C'_{F\alpha}$ is related to the pure lateral slip conditions when $F_x = 0$. Based on Equation (3.4), when the tire tractive force is present at the tires, $C_{F\alpha} < C'_{F\alpha}$; therefore, the effect of adding tractive force at the tires is a reduction in the cornering stiffness of these tires. This is an effect similar to travel on a surface which causes smaller cornering stiffness for the tires, for instance an off-road surface, which was analyzed in the previous section. In addition to the decrease in the cornering stiffness, applying the driving torque to the wheel during forward acceleration has a significant effect on the tire aligning
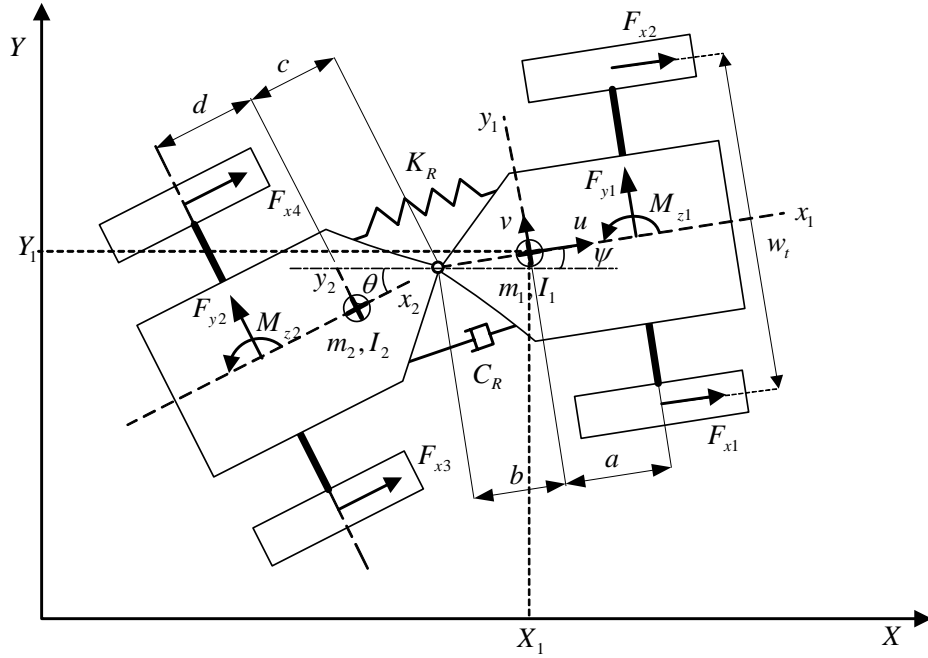
Figure 3-10: A 3-DOF model of an ASV with considering tire tractive force.

moment [23]. For a given slip angle, a driving torque increases the tire aligning moment, which has a stabilizing effect during the snaking mode. Therefore, in summary, traveling with a constant forward speed results in a more critical situation regarding the lateral stability, compared with the travel at the same speed with forward acceleration.

3.4   Operation in Steady-State Turning

One of the main disadvantages of ASVs is roll instability in steady-state turning, even at low speeds. This decreases the maximum safe driving speed of ASVs during steady-state turning. The articulation angle is typically less than $\pm 10°$ for travel on public roads. When an ASV is traveling with a non-zero articulation angle in the steady-state condition, the normal load on the inside tires will be decreased and on the outside tires will be increased. Due to the nonlinear relation between the normal force and lateral force, this lateral load transfer results in a reduction in the total lateral force [23, 37] at the front and rear. This effect is shown for a given axle in Figure 3-11. As mentioned before, the reduction in the resultant lateral force at

71

the both front and rear has a stabilizing effect during the snaking mode. In addition, when an ASV is traveling with a non-zero articulation angle in the steady-state, the slip angles of the tires will increase. When the slip angle increases, the equivalent cornering stiffness of the tire decreases (see Figure 2-2).

Moreover, during steady-state turning, tractive forces should be present at the tires for balancing the longitudinal components of the inertia forces and the lateral tire forces. The tractive force at the tires also causes a stabilizing effect during the snaking mode, as shown previously. Therefore, all of the above-mentioned factors cause stabilizing effects during the snaking mode for travel with non-zero articulation angle.

Furthermore, for hydraulic systems with a valve-piston combination, the most critical operating point from a stability viewpoint is the neutral position of the valve. Near this point, the valve flow gain is very high, and the damping ratio is very small [31]. For the hydraulic steering system of an ASV, the equivalent torsional stiffness is minimum at the zero articulation angle. As shown previously, the compressibility effects of the trapped oil in the cylinders correspond to a combination of two torsional springs at the articulation joint, according to Equation (2.44). Based on this equation, it is easy to see that the minimum stiffness occurs when the piston is in the middle, that is, the vehicle is moving in a straight line. Again, these imply that the straight-line motion (zero articulation angle) is more critical, compared with the motion during steady-state turning.

3.5   Operation with Locked Differentials

For an ASV, the front and rear differential locks are hydraulically operated, and may be activated on-the-go or in standstill by the operator through pushing a button or through a foot-controlled valve in the cab. By opening these locks, full differential operation during normal load conditions can be achieved. Both the front and rear differentials can be also controlled by a single valve. This section is intended to investigate the effects of locking differentials on stability during the snaking mode of the baseline vehicle. First, the 3-DOF model is modified for the operation with locked differentials. Then, the critical torsional stiffness K_{cr} for the vehicle with front or rear differentials locked in the straight-line motion with constant forward
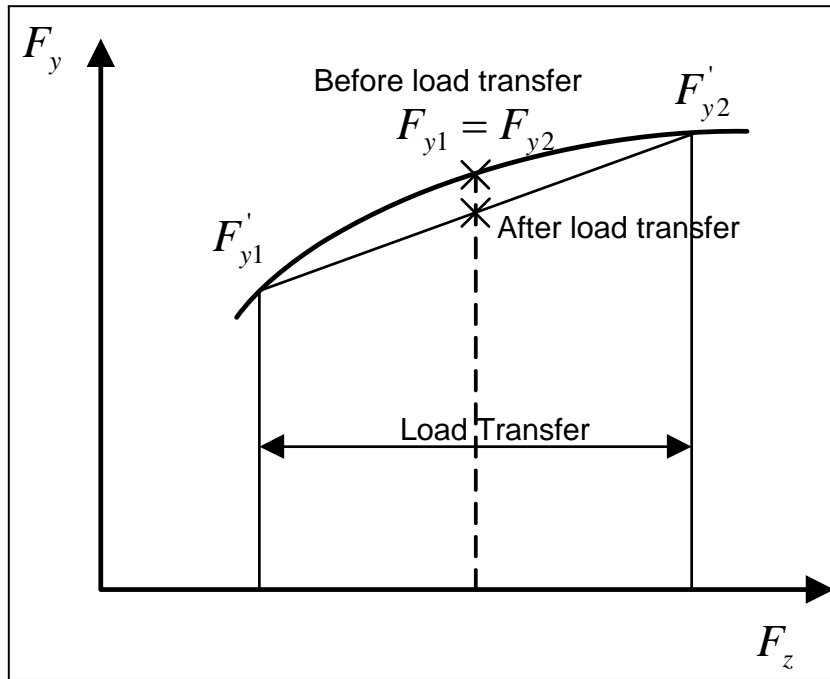
Figure 3-11: Effect of lateral load transfer on resultant force.

speed (which is the most critical driving condition based on the above-mentioned analyses) is plotted for changes in the center of mass positions. To verify the results from the analysis of the resulting 5-DOF model, the motion of the virtual prototype with the front differential locked is simulated during the snaking mode in ADAMS.

3.5.1   5-DOF Model of Vehicle with Locked Differentials

In wheel steer vehicles, when an axle is solid, the right and left wheels will rotate at the same speed. If the left and right wheels travel in tracks with different radius, this causes longitudinal slips for these wheels. Therefore, two longitudinal forces with opposite directions will be produced, which results in a turning moment on the vehicle. This effect has been used in racing cars with solid differentials to produce an understeering moment [37]. Moreover, this effect has been used to enhance running stability and controllability of large-sized vehicles, for instance trucks, against disturbances such as road roughness and wind gusts at higher speeds [41]. During the snaking mode of an ASV with locked front and rear differentials, there is
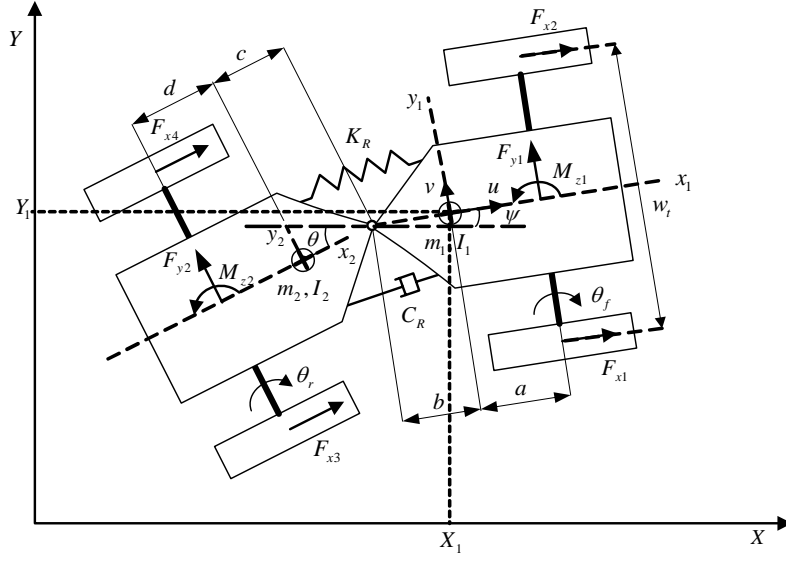
Figure 3-12: A 5-DOF model of an ASV with locked differentials.

similar condition. The previous 3-DOF model can be extended to include the effects of locking differentials, as shown in Figure 3-12.

3.5.2 Equations for Perturbed Motion

In this case, new variables θ_f and θ_r, which represent the spin rotation angle of the front and rear wheels, introduce two additional degrees of freedom. The independent coordinates $\mathbf{q}$ to describe the configuration of the system are:

$$\mathbf{q} = [X_1, Y_1, \psi, \theta, \theta_f, \theta_r] \tag{3.5}$$

According to Equation (3.1), the longitudinal forces produced at the tires contribute the virtual work δW_l to the system. Therefore, the generalized forces and moments are changed as follows:

$$Q_Y = F_{y1} + F_{y2} \tag{3.6}$$

$$Q_\psi = aF_{y1} - bF_{y2} + M_{z1} + (F_{x1} - F_{x2})\frac{w_t}{2} \tag{3.7}$$

74

$$Q_\theta = -(c+d)F_{y2} + M_{z2} + (F_{x3} - F_{x4})\frac{w_t}{2} \tag{3.8}$$

The longitudinal tire force produced at the left and right tires are similar; therefore, the forward speed remains constant ($u \approx Const.$). The wheel longitudinal slips, which are required to find the longitudinal tire force, based on Equation (2.1) can be described in a linearized form as:

$$S_1 \approx -\frac{u + \frac{w_t}{2}\dot\psi - r_e\dot\theta_f}{u} \tag{3.9}$$

$$S_2 \approx -\frac{u - \frac{w_t}{2}\dot\psi - r_e\dot\theta_f}{u} \tag{3.10}$$

$$S_3 \approx -\frac{u + \frac{w_t}{2}\dot\psi - r_e\dot\theta_r}{u} \tag{3.11}$$

$$S_4 \approx -\frac{u - \frac{w_t}{2}\dot\psi - r_e\dot\theta_r}{u} \tag{3.12}$$

Also, based on Equation (2.10), the tire longitudinal forces F_{x1}, F_{x2}, F_{x3} and F_{x4} are as follows:

$$F_{x1} = C_{sf}S_1 \tag{3.13}$$

$$F_{x2} = C_{sf}S_2 \tag{3.14}$$

$$F_{x3} = C_{sr}S_3 \tag{3.15}$$

$$F_{x4} = C_{sr}S_4 \tag{3.16}$$

where C_{sf} and C_{sr} are the longitudinal slip stiffness of the front and rear tires, respectively. After substituting the resulting longitudinal tire force relationships, two variables θ_f and θ_r are eliminated from the equations of motion, and based on Equation (2.71) and Equation (2.70), the following state variables can be again used to represent the final equations:

$$\mathbf{X} = [v, \dot\psi, \dot\phi, \phi]^T \tag{3.17}$$

The final form of the equations in terms of the state variables can be considered as a LTI system described by:

$$\dot{\mathbf{X}} = \mathbf{AX} \tag{3.18}$$

The entries for matrix $\mathbf{A}$ are found in Appendix B, and are different from those for the 3-DOF model. They include the longitudinal slip stiffness of the tires, in addition to the cornering stiffness. The characteristic equation of the system is:

$$a_4 s^4 + a_3 s^3 + a_2 s^2 + a_1 s + a_0 = 0 \tag{3.19}$$

Therefore, the system has four eigenvalues (λ_1, λ_2, λ_3 and λ_4) whose values are dependent on the forward speed and other parameters of the vehicle.

3.5.3 Preliminary Analysis

For an ASV, locking the differentials causes longitudinal slips at the wheels for non-zero articulation angles. This leads to the longitudinal tire forces at the wheels that produce turning moments. For introductory study, the baseline vehicle with its nominal mass properties (given in Table 2.6 and $w_t = 2.46$ m) and the rear part center of mass position $d = -0.5$ m is considered when it is traveling with the front differential locked. For $K_R = 1 \times 10^5$ Nm/rad and $C_R = 0$, the vehicle with open differentials will show the lateral instability over a range of operating speeds up to 20m/s, as shown in Figure 3-2. However, if the front differential is locked, the vehicle will be stable up to $u_{cr} = 14$ m/s, as shown in Figure 3-13. Therefore, the resultant turning moment produced by locking the front differential has a stabilizing effect. Now, this result is compared with the response of the virtual prototype of the vehicle with front differential locked during the snaking mode in ADAMS.

3.5.4 Simulation in ADAMS

For the virtual prototype of the baseline vehicle with the front differential locked (the rear part center of mass position $d = -0.5$ m, $K_R = 1 \times 10^5$ Nm/rad and $C_R = 0$), the perturbed motion is simulated for forward speeds smaller, equal to and higher than the critical speed predicted by the 5-DOF model ($u_{cr} = 14$ m/s). To model the locked front differential, the left and right driveshafts of the front axle are connected rigidly by a fixed joint, but the left and right wheels
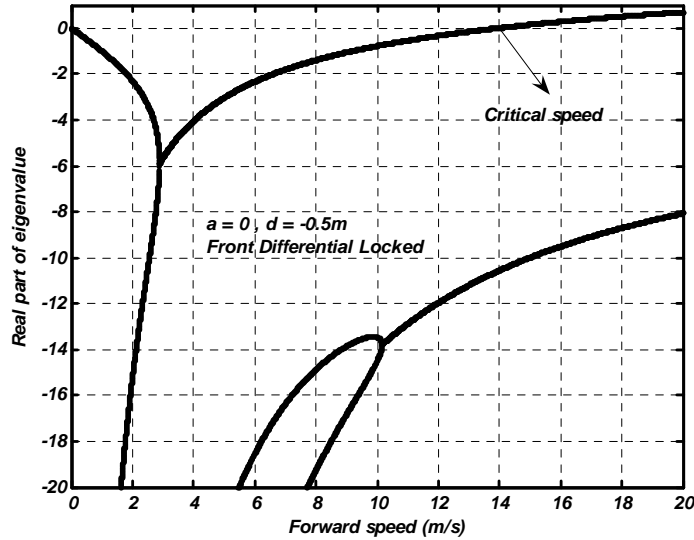
Figure 3-13: Real part of eigenvalues for $a = 0$ and $d = -0.5$ m (front differential locked).

of the rear axle can rotate independently. The results are shown in Figures 3-14, 3-15 and 3-16. For $u = 13.5$ m/s, the response is a damped oscillatory yaw motion, as shown in Figure 3-14. The amplitude of this motion is decreasing. The response at $u = 14$ m/s is an undamped oscillatory yaw motion, as shown in Figure 3-15. The amplitude of this motion is constant, and thus, this velocity indicates the critical speed of the vehicle. For $u = 14.5$ m/s, the response is a snaking mode whose amplitude is increasing, as shown in Figure 3-16. Therefore, the dynamic behavior of the virtual prototype is similar to that predicted by the 5-DOF model. This means that the 5-DOF model can be used to identify the effects of locking the differentials on the stability during the snaking mode with an acceptable precision.

3.5.5 Locking Front and Rear Differentials

As shown in the previous sections, if the front differential is locked, the vehicle will be unstable for $u > 14$ m/s, based on the 5-DOF model. However, if both the front and rear differentials are locked, the vehicle will be stable over a range of operating speeds up to and beyond 20 m/s. This is shown for the baseline vehicle with its nominal mass properties ($d = -0.5$ m, $K_R = 1 \times 10^5$ Nm/rad and $C_R = 0$) in Figure 3-17. As mentioned before, ASVs have a
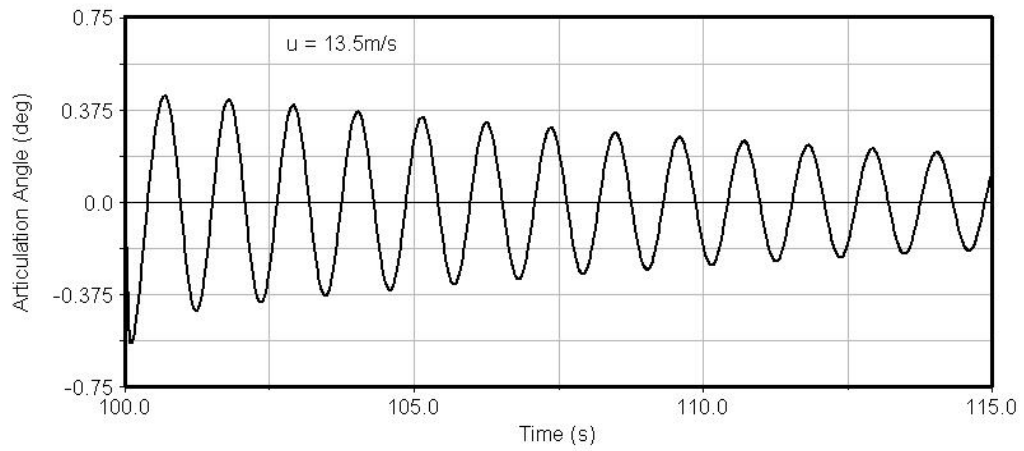
Figure 3-14: Articulation angle for $u = 13.5$ m/s with front differential locked.
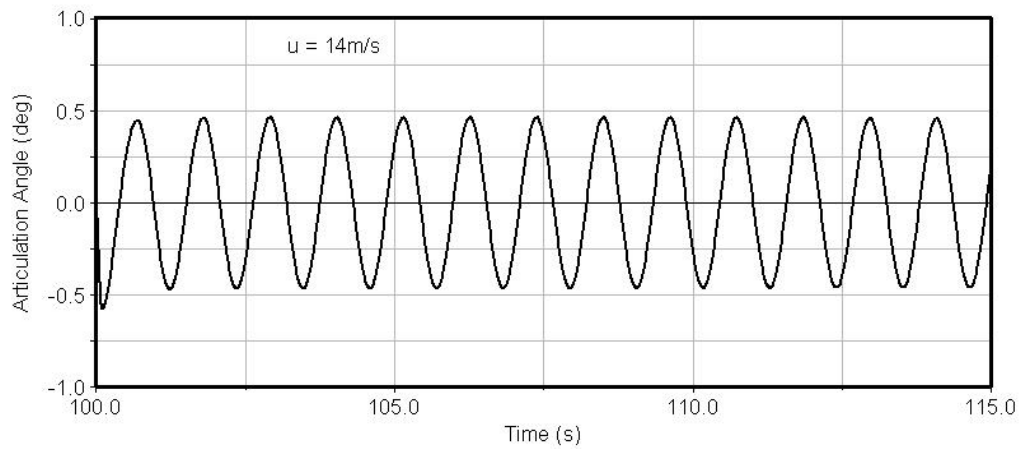
Figure 3-15: Articulation angle for $u = 14$ m/s with front differential locked.
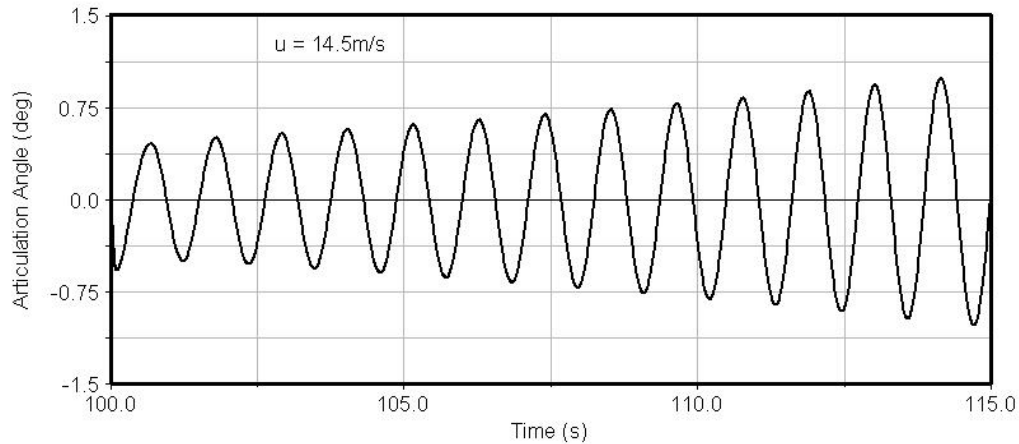
Figure 3-16: Articulation angle for $u = 14.5$ m/s with front differential locked.

differential locking device that can be activated manually by the operator even on-the-go. Therefore, the operator can easily utilize this device for stabilizing the vehicle, as the frequency of the snaking oscillations is low (about 1 Hz). Therefore, this is a simple method to alleviate the snaking oscillations effectively in different conditions.

To show the effectiveness of locking differentials, K_{cr} for different center of mass positions for front or rear or both differentials locked are compared during the straight line on-highway motion with constant forward speed, which is the most critical driving condition for a conventional ASV. Figure 3-18 shows K_{cr} for both differentials locked. Comparing this plot with that for both differentials open (see Figure 3-4) indicates that the value of K_{cr} is reduced by a factor of 100 for different center of mass positions if the differentials are locked. This means that the instability will not occur for different center of mass positions during the most critical driving condition unless there is a major problem in the hydraulic steering system of the vehicle. Similar plots for the vehicle with the front and also rear differential locked are shown in Figures 3-19 and 3-20. These plots are obtained from the 5-DOF model by eliminating the effects of the resulting longitudinal tire forces at the front or rear. For these cases, K_{cr} is still considerably less than that for the open differentials (see Figure 3-4), but more than that for the both differentials locked (see Figure 3-18). However, when only one of the differentials is locked, a better maneuverability can be achieved during the motion. In addition, the tire wear

79
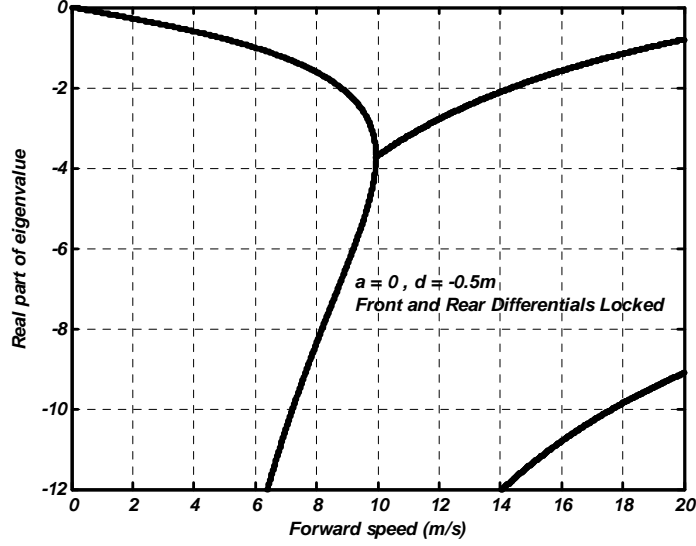
Figure 3-17: Eigenvalues results for $a = 0$ and $d = -0.5$ m (both differentials locked).

problem is less under this condition.

These results can be clearly justified based on a good theoretical explanation as follows. The unstable snaking mode of an ASV is an undamped oscillatory yaw motion that can be alleviated by introducing appropriate values of damping to the system for a given K_R. This can be done by absorbing energy through friction at the articulation joint or introducing leakage across the hydraulic cylinders [10, 16]. These forms of damping will add extra values to the existing C_R. The key point is that by locking the differentials, the required damping for alleviating the snaking oscillations will be provided by the work done by longitudinal tire forces. This can be realized by comparing the virtual work done by these forces δW_l and that done by C_R at the articulation joint δW_c. The value of δW_c can be described as follows:

$$\delta W_c = -[C_R(\dot{\psi} - \dot{\theta})\delta\psi + C_R(\dot{\theta} - \dot{\psi})\delta\theta] \tag{3.20}$$

By using Equation (3.1), and the equations describing the tire longitudinal slips, δW_l can be described as follows:
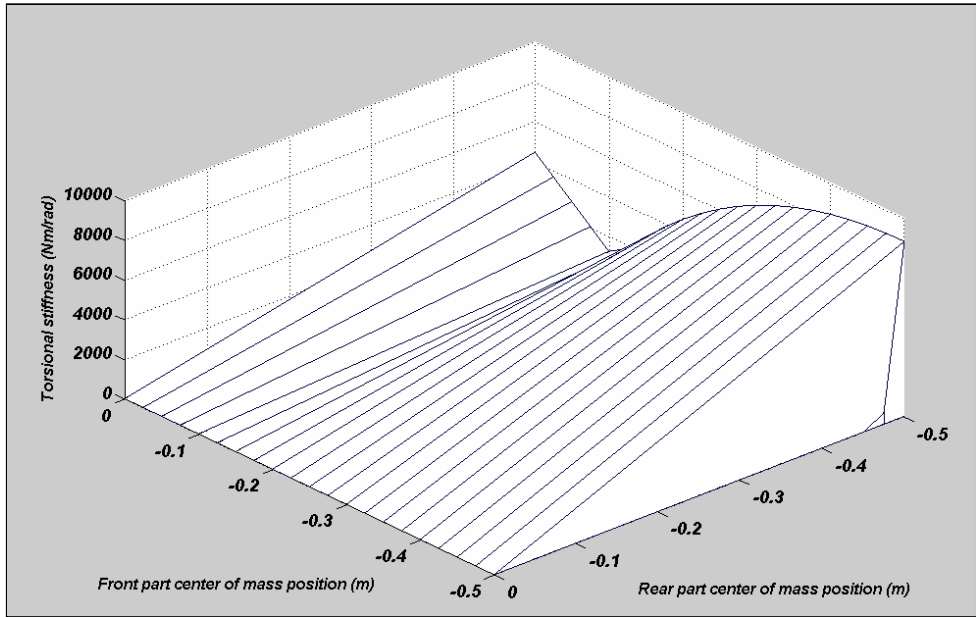
Figure 3-18: Critical torsional stiffness for both differentials locked.
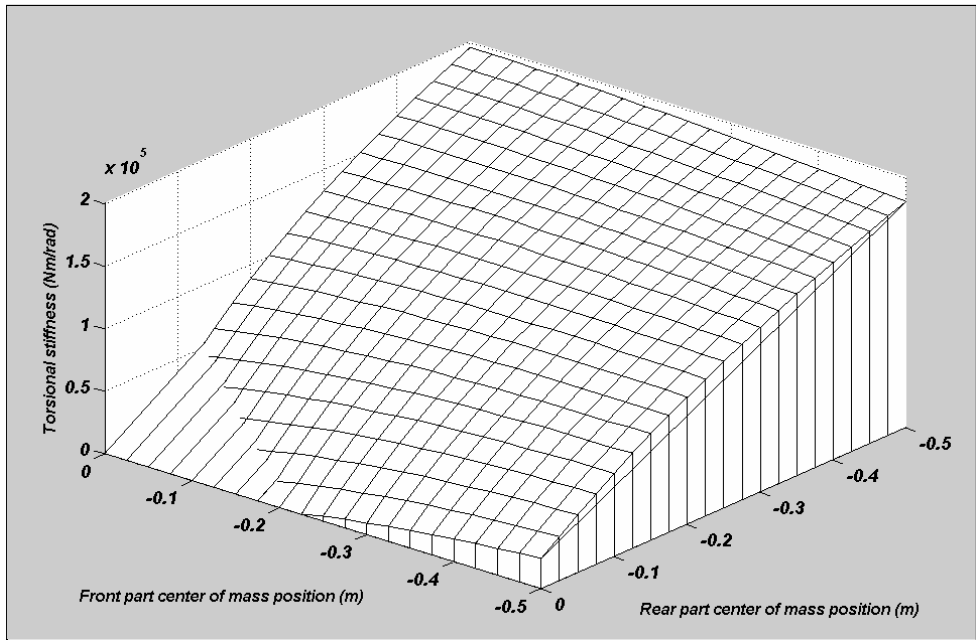
Figure 3-19: Critical torsional stiffness for front differential locked.
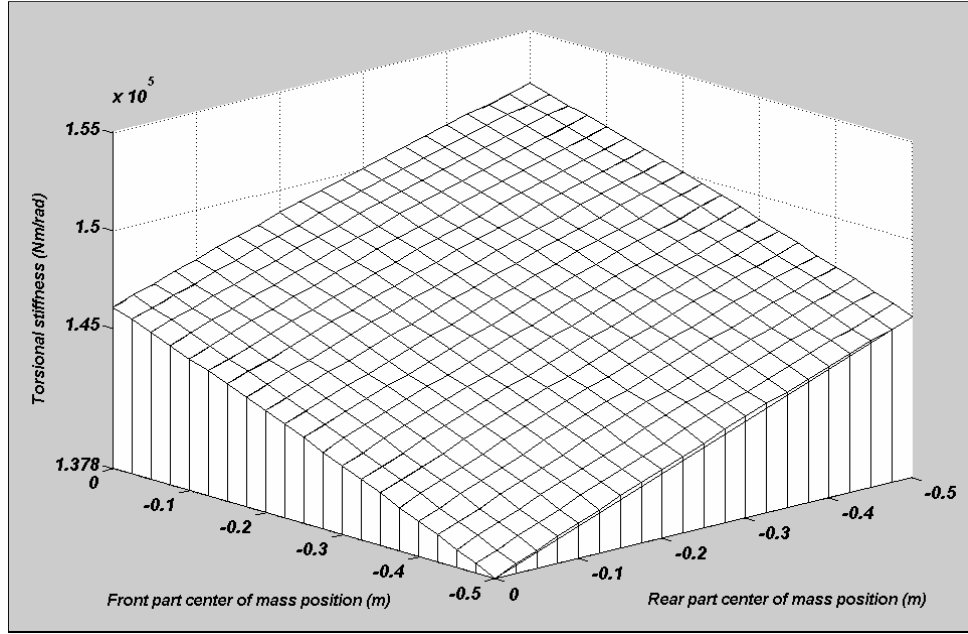
Figure 3-20: Critical torsional stiffness for rear differential locked.

$$\delta W_l = -[\frac{C_{sf}w_t^2\dot{\psi}}{2u}\delta\psi + \frac{C_{sr}w_t^2\dot{\theta}}{2u}\delta\theta]$$ (3.21)

Comparing Equations (3.20) and (3.21) clearly shows that locking the differentials introduces an equivalent damping, similar to C_R, that dissipates the energy during the snaking mode. It is obvious that when both the differentials are locked, the equivalent damping increases. Therefore, the instability can be prevented more effectively in this condition. These explanations are reasonably consistent with the results from the 5-DOF model analysis in Figures 3-18 to 3-20.

3.6   Operation with Rear-mounted Log Interacting with Ground

ASVs are also used to carry a rear-mounted load or attachment that contacts the ground. For instance, forestry skidders are usually used for carrying logs on the soft surfaces of forestlands or farms, where, under typical conditions, tire cornering properties and lateral load capability may be half that of on-highway characteristics [28]. In this condition, even if the vehicle with

its rear–mounted load can travel at higher speeds, the lateral tire forces are still very small to cause the lateral instability during the snaking mode. There are new trends towards the more efficient usage of ASVs to move loads to farther places for loading operations. For this purpose, ASVs may also be required to carry their rear-mounted loads on poor roads or on dry and firm soils, and thus, an unstable snaking mode may occur. In this situation, the tire cornering properties and lateral force capabilities are higher than those for forestlands, but still less than those for highways. In addition, the moment of inertia of the whole rear part of the vehicle may be increased considerably by a long rear-mounted attachment or load. Most importantly, the position of the center of mass of the whole rear part of the vehicle, including a rear-mounted attachment or load, will be well backward of the rear axle. All of these factors deteriorate the lateral stability of the vehicle with its rear-mounted load during the snaking mode. In this section, an analysis of the lateral stability of the baseline vehicle pulling a log in the critical condition is presented.

3.6.1 4-DOF Model of Vehicle with Load

A model of the perturbed motion for the baseline vehicle with load is illustrated in Figure 3-21. The load is a log carried by the rear grapple of the vehicle. The grapple is connected to the rear part by a joint (grapple joint), and thus, the log can rotate during the motion. This introduces an extra degree of freedom to the 3-DOF model, and thus, the resulting model will have 4-DOF. In addition, a torsional damping C_g at the grapple joint is present (due to a swing dampener with friction plate), and the value of C_g can be adjusted manually by the operator to some degree.

3.6.2 Equations for Perturbed Motion

Forces acting at different contact points of the vehicle before the perturbed motion are shown in Figure 3-22. The rear grapple and the log are both connected to the rear part by a lateral axis and a vertical axis joint. Again, N_1 and N_2 are the resultant vertical loads at the front and rear axles, respectively, and it is assumed that they act at the center of the axles. The rolling resistance of the tires is also neglected. However, a vertical contact force N_3 and a longitudinal force F_l are present at the load-ground contact area, and it is assumed that:
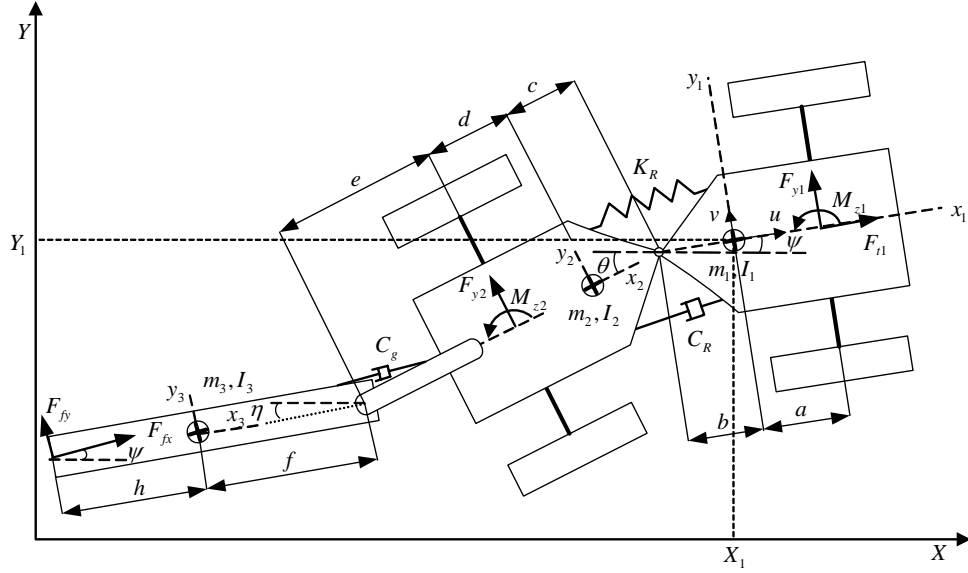
Figure 3-21: A model of an ASV with a rear-mounted load.

$$F_l = \mu N_3 \tag{3.22}$$

where μ is the surface friction coefficient, and the direction of F_l is the opposite of the direction of the log contact point velocity. As the forward velocity u is assumed to be constant, the resultant tractive force at the tires equals to F_l. It is assumed that a resultant tractive force F_{t1} acts only at the front wheels (front-wheel drive configuration). For small deviations, the type of the drive configuration of the vehicle has negligible effect on the dynamic behavior during the snaking mode. Therefore:

$$F_{t1} = \mu N_3 \tag{3.23}$$

It is assumed that N_1, N_2 and N_3 remain constant during the perturbed motion. These forces can be computed using the static equilibrium equations. As shown in Figure 3-22, there are two reaction forces, P and Q, at the grapple lateral axis joint, which are used for finding the following relations:

$$N_1 = \frac{m_1 g(b + c + d) + m_2 gd - Pe - \mu N_3 H_g}{a + b + c + d} \tag{3.24}$$

84
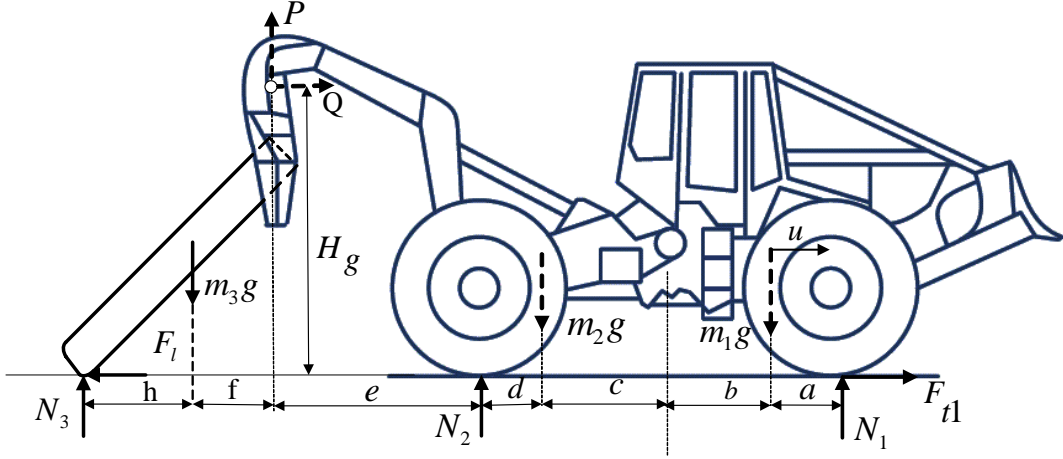
Figure 3-22: Contact forces before perturbed motion for vehicle with load.

$$N_2 = (m_1 + m_2)g - P - N_1 \tag{3.25}$$

$$N_3 = \frac{m_3 g f}{f + h + \mu H_g} \tag{3.26}$$

$$P = m_3 g - N_3 \tag{3.27}$$

where:

e : Distance from the grapple joint to rear wheels

f: Distance from the grapple joint to the log center of mass

h : Distance from the log center of mass to the log contact point

H_g : Height of the grapple lateral axis joint above ground

The independent coordinates $\mathbf{q}$ to describe the situation of the system are:

$$\mathbf{q} = [X_1, Y_1, \psi, \theta, \eta] \tag{3.28}$$

where η is the angle between the load centreline and X axis. The total kinetic energy of the system is:

$$T = T_1 + T_2 + T_3 \tag{3.29}$$

where T_1 and T_2 are the same as those for the 3-DOF model, and T_3 is the kinetic energy of

the load:

$$T_3 = \frac{1}{2}m_3\{\dot{X}_1^2 + [\dot{Y}_1 - b\dot{\psi} - (c+d)\dot{\theta} - f\dot{\eta}]^2\} + \frac{1}{2}I_3\dot{\eta}^2 \tag{3.30}$$

where m_3 and I_3 represent load mass and moment of inertia, respectively. The potential energy of the system is the same as 3-DOF model, but the dissipation function is due to both torsional damper at the articulation and grapple joints:

$$R = \frac{1}{2}C_R(\dot{\psi} - \dot{\theta})^2 + \frac{1}{2}C_g(\dot{\theta} - \dot{\eta})^2 \tag{3.31}$$

The load contact force F_l can be considered as a resultant of lateral and longitudinal components F_{fy} and F_{fx} in $x_1- y_1$ frame. These components are proportional to N_3, in direction opposite to log tip velocity:

$$F_{fx} = -\mu N_3 \cos(\frac{v - br - (c+d+e)\dot{\theta} - (f+h)\dot{\eta}}{u}) \tag{3.32}$$

$$F_{fy} = -\mu N_3 \sin(\frac{v - br - (c+d+e)\dot{\theta} - (f+h)\dot{\eta}}{u}) \tag{3.33}$$

The virtual work done by F_{t1} and F_{fx} can be described as follows:

$$\delta W_1 = -F_{fx}[(c+d+e+f+h)(\psi-\theta)]\delta\theta - F_{fx}[(f+h)(\psi-\eta)]\delta\eta + F_{fx}\psi\delta Y_1 + F_{t1}\psi\delta Y_1 \tag{3.34}$$

The virtual work done by F_{fy} is:

$$\delta W_2 = F_{fy}\delta[Y_1 - b\psi - (c+d+e+f+h)\theta - (f+h)\eta] \tag{3.35}$$

The above equations can be used to describe the general forces and moments as follows:

$$Q_Y = F_{y1} + F_{y2} + F_{fy} \tag{3.36}$$

$$Q_\psi = aF_{y1} - bF_{y2} - F_{fy}b + M_{z1} \tag{3.37}$$

$$Q_\theta = -(c+d)F_{y2} - F_{fy}(c+d+e+f+h) + M_{z2} - F_{fx}[(c+d+e+f+h)(\psi-\theta)] \tag{3.38}$$

86

$$Q_\eta = -F_{fx}(f + h)(\psi - \eta) - F_{fy}(f + h) \tag{3.39}$$

As the baseline vehicle is used for carrying the load in off-road applications, the mobility number-based off-road tire model is used. Therefore, the lateral tire forces and aligning moments can be calculated using Equation (2.22) and Equation (2.24). By introducing the following state variables, the order can be reduced to six. In addition, the articulation angle ϕ and grapple joint angle φ will be used:

$$\mathbf{X} = [v, \dot{\psi}, \dot{\phi}, \dot{\varphi}, \phi, \varphi]^T \tag{3.40}$$

where:

$$\varphi = \theta - \eta \tag{3.41}$$

Again, the final form of the equations in terms of the state variables can be considered as a LTI system described by:

$$\dot{\mathbf{X}} = \mathbf{A}\mathbf{X} \tag{3.42}$$

The entries for matrix $\mathbf{A}$ are found in Appendix C. The characteristic equation of the system is:

$$a_6 s^6 + a_5 s^5 + a_4 s^4 + a_3 s^3 + a_2 s^2 + a_1 s + a_0 = 0 \tag{3.43}$$

Based on the Routh criteria, the coefficinets of this equation can be used to identify the stability of the system. Also, the roots of Equation (3.43) are the six eigenvalues of the system.

3.6.3 Effects of Parameter Variations

Table 3.1 shows the parameters of the baseline vehicle and its rear-mounted load. The mobility numbers MOB_1 and MOB_2 for the front and rear tires, respectively, are given for a dry and firm surface. Different experiments in a variety of field conditions show that the tire aligning moment on deformable surfaces is negligibly small [25, 42], and thus, the tire aligning moment coefficients $C_{M\alpha 1}$ and $C_{M\alpha 2}$ are set to zero. In addition, the center of mass position for the

Parameter	Unit	Value	Parameter	Unit	Value
m_1	kg	7280	a	m	0.03
m_2	kg	7280	b	m	1.697
m_3	kg	2500	c	m	1.803
I_1	kgm^2	7280	d	m	-0.1
I_2	kgm^2	7280	e	m	1.797
I_3	kgm^2	10700	f	m	3.5
MOB_1	-	17.8	h	m	3.45
MOB_2	-	13.5	H_g	m	1.5
C_I	kPa	1500	μ	-	0.9

Table 3.1: Parameters of baseline vehicle and its load.

rear part is located far from the rear axle, which is another factor that would reduce the effect of the aligning moment on stability.

If C_R and C_g are assumed to be negligibly small, for $K_R = 1 \times 10^6$ Nm/rad, all the eigenvalues have negative real parts; thus, the vehicle is stable for any forward speed u smaller than 7 m/s, as shown in Figure 3-23. If K_R is reduced to a value, such as 5×10^5 Nm/rad, the real part of the dominant complex roots is very close to the horizontal axis, which indicates a slowly damped oscillatory mode, as plotted in Figure 3-24. The other eigenvalues have negative real parts and similar patterns to their previous ones. When K_R is reduced to a lower value, such as 4.5×10^5 Nm/rad, the dominant oscillatory roots have a positive real part at forward velocities higher than $u_{cr} = 4.75$ m/s, as depicted in Figure 3-25. The value of u_{cr} depends highly on K_R and C_R. When K_R and C_R are increased, u_{cr} increases, as shown in Figure 3-26. For a suitable combination of K_R and C_R values, the vehicle is stable over the given range of operating speeds. This is shown for $K_R = 3.5 \times 10^5$ Nm/rad and $C_R = 300$ Nms/rad in Figure 3-27. For much smaller values of K_R with $C_R = 0$, the unstable snaking oscillations may occur over the given range of the operating speeds, as shown in Figure 3-28 for $K_R = 1 \times 10^5$ Nm/rad. The snaking mode for this value of K_R has a typical frequency of 0.9 Hz (predicted by the model). When K_R decreases from this value, the unstable snaking mode occurs over the given range of operating speeds, but the frequency of the snaking mode is also reduced because the effective stiffness of the system is diminished.

During the snaking mode, all parts of the vehicle including the rear-mounted log are involved in the oscillatory motion. This is an undesirable behavior because even a very small change
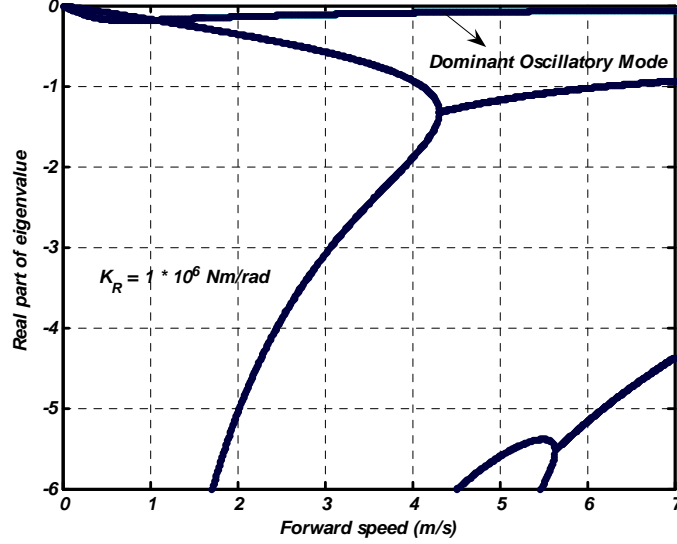
Figure 3-23: Eigenvalue results for $K_R = 1 \times 10^6$ Nm/rad (vehicle with load).

in the articulation or grapple joint angle will result in a considerable change in the position of the log contact point. In addition to increasing C_R, by an increase in C_g at the grapple joint, u_{cr} can be increased, and the instability can be removed. This is shown in Figure 3-29, when C_g takes different values, but $C_R = 0$. However, the effect of C_R on u_{cr} is more significant than that of C_g, as shown in Figure 3-26. For a suitable combination of K_R and C_g values, the vehicle is stable over the whole range of its operating speed. This is plotted for $K_R = 3.5 \times 10^5$ Nm/rad and $C_g = 600$ Nms/rad in Figure 3-30.

3.6.4   Simulation in ADAMS

The virtual prototype of the baseline vehicle is changed in a way that a log is held by a grapple at the rear part, as shown in Figure 3-31. A torsional damper C_g is present at the grapple joint, similar to the 4-DOF model. The grapple and log can rotate about the vertical axis by this joint. In addition, they can rotate around the lateral axis freely by a lateral axis joint. Moreover, a contact force between the log and the ground is defined. This can be done by defining a plane as the ground and using the contact function of ADAMS. The parameters of the load will be the same as those for the 4-DOF model. A subroutine including the off-road
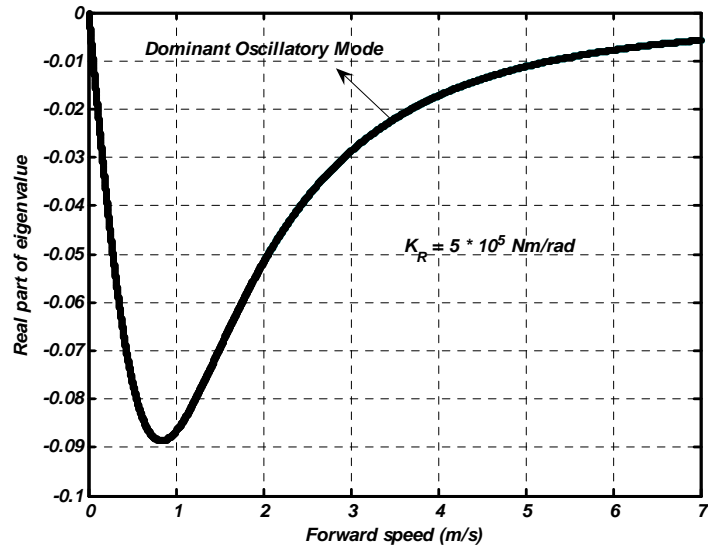
Figure 3-24: Eigenvalue results for $K_R = 5 \times 10^5$ Nm/rad (vehicle with load).
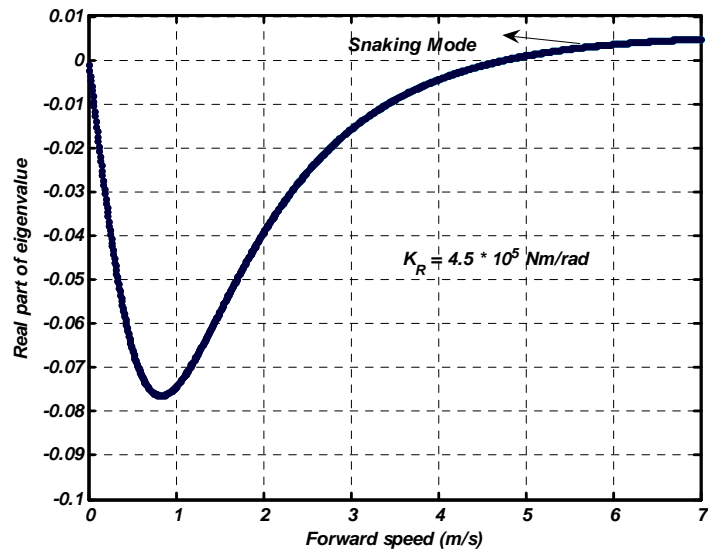
Figure 3-25: Real part of dominant oscillatory eigenvalues for $K_R = 4.5 \times 10^5$ Nm/rad (vehicle with load).
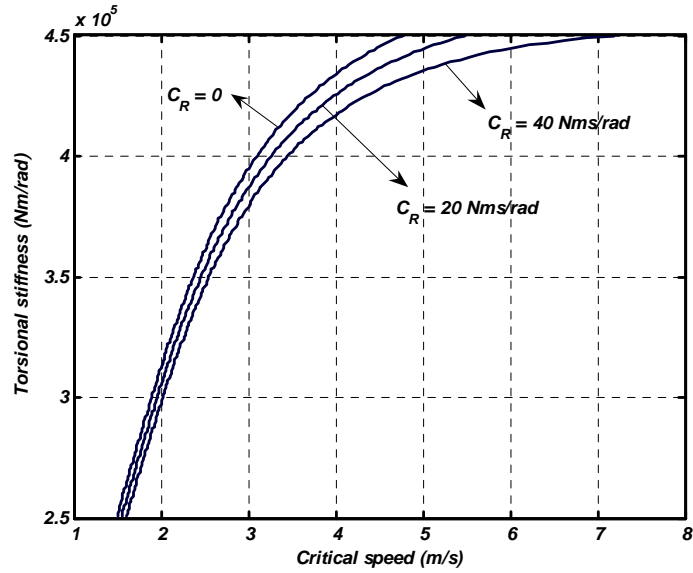
Figure 3-26: Critical speed for different values of K_R and C_R (vehicle with load).
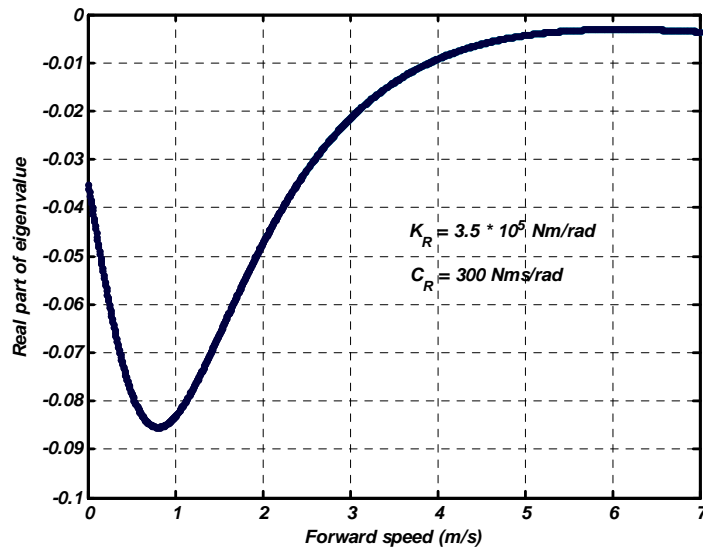
Figure 3-27: Eigenvalue results for $K_R = 3.5 \times 10^5$ Nm/rad and $C_R = 300$ Nms/rad (vehicle with load).
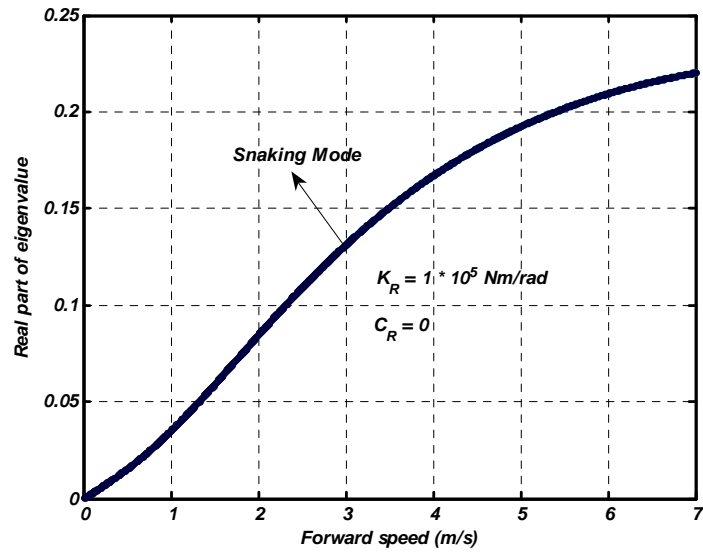
Figure 3-28: Real part of unstable oscillatory eigenvalues for $K_R = 1 \times 10^5$ Nm/rad and $C_R = 0$.
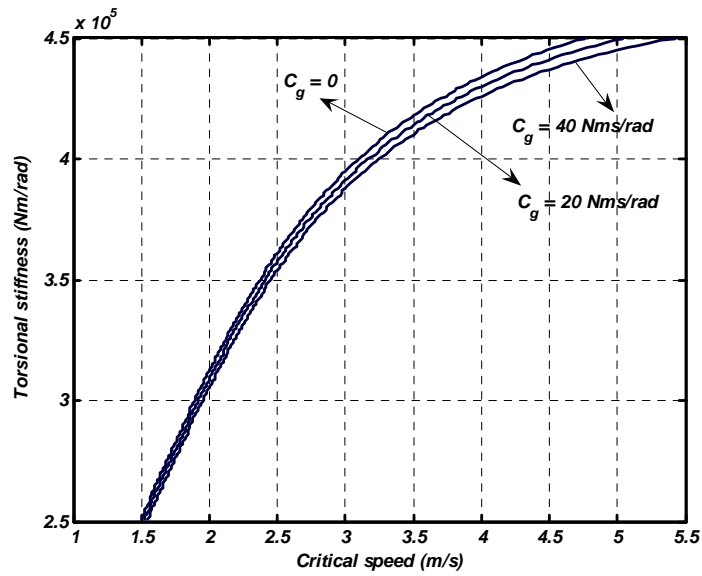
Figure 3-29: Critical speed for $C_R = 0$ and different values of C_g.
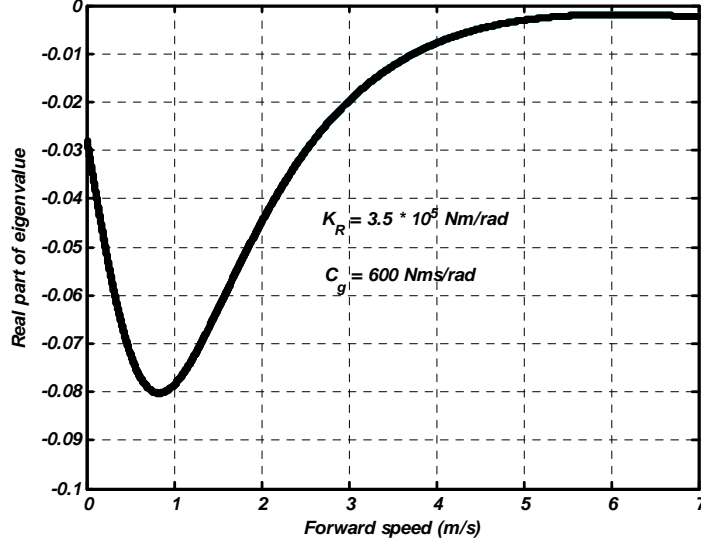
Figure 3-30: Eigenvalue results for $K_R = 3.5 \times 10^5$ Nm/rad and $C_g = 600$ Nms/rad $(C_R = 0)$.

tire model based on the mobility number is developed and linked to the model of the vehicle. The tire rolling resistance, lateral force and longitudinal force are computed by this subroutine for both front and rear tires. The effect of longitudinal tire force on the lateral force coefficient (the friction ellipse model, Equation (2.30)) is also considered.

Figure 3-32 shows the response for the perturbed motion with $u = 5$ m/s, and $K_R = 5 \times 10^5$ Nm/rad and $C_R = C_g = 0$ after applying T_e. The response is a slowly damped oscillatory mode, as predicted by the 4-DOF model.

Figure 3-33 shows the response for $K_R = 3.5 \times 10^5$ Nm/rad and $C_R = C_g = 0$. In this condition, the vehicle is again moving with forward velocity $u = 5$ m/s, and the response is an undamped oscillatory mode, as predicted by the 4-DOF model for this value of K_R. The change in the grapple joint angle is also shown in Figure 3-34. This response is also an undamped oscillatory motion, similar to that of the articulation angle. Figure 3-35 shows the response with $u = 5$ m/s, $K_R = 3.5 \times 10^5$ Nm/rad, $C_R = 300$ Nms/rad and $C_g = 0$. The response is a slowly damped oscillatory motion and the vehicle is stable at this velocity, as predicted by the 4-DOF model. A similar response can be achieved if C_g is increased to 600 Nms/rad, as plotted in Figure 3-36.

93
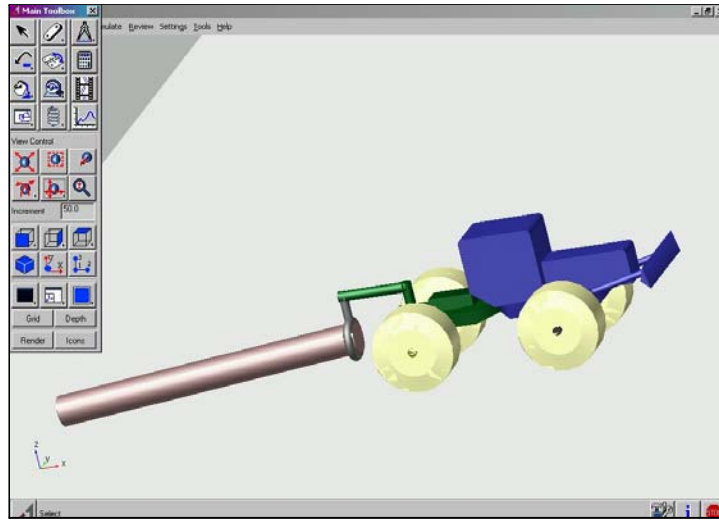
Figure 3-31: Virtual prototype of baseline vehicle with load in ADAMS.
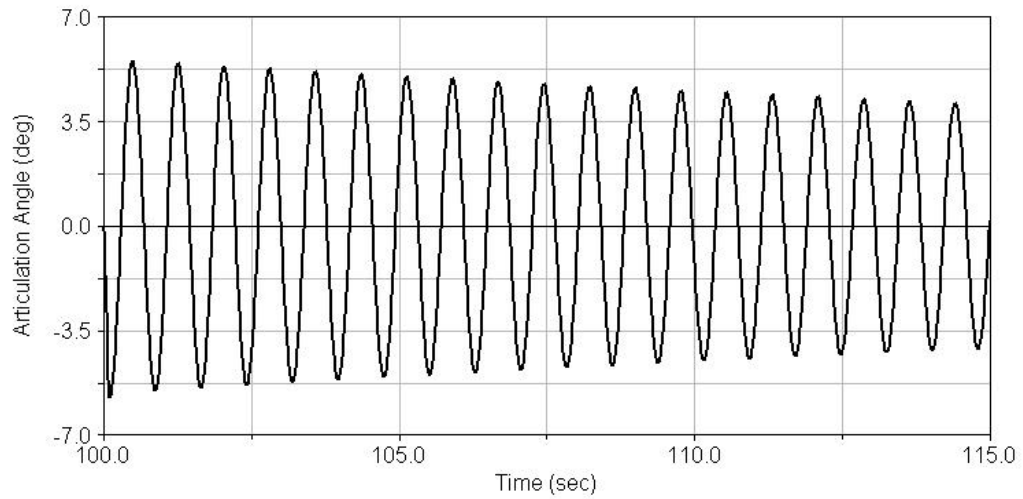
Figure 3-32: Articulation angle for $K_R = 5 \times 10^5$ Nm/rad and $u = 5$ m/s.
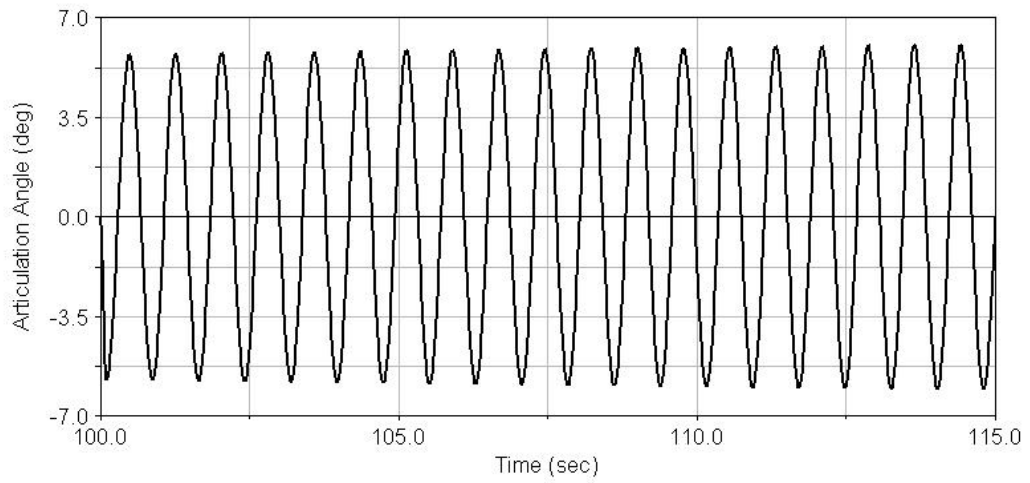
Figure 3-33: Articulation angle for $K_R = 3.5 \times 10^5$ Nm/rad and $u = 5$ m/s.
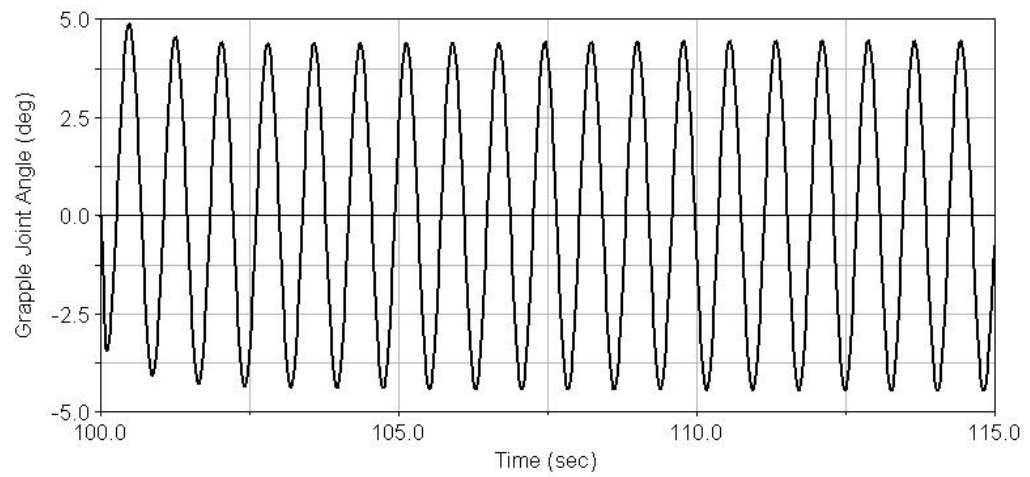
Figure 3-34: Grapple joint angle for $K_R = 3.5 \times 10^5$ Nm/rad and $u = 5$ m/s.
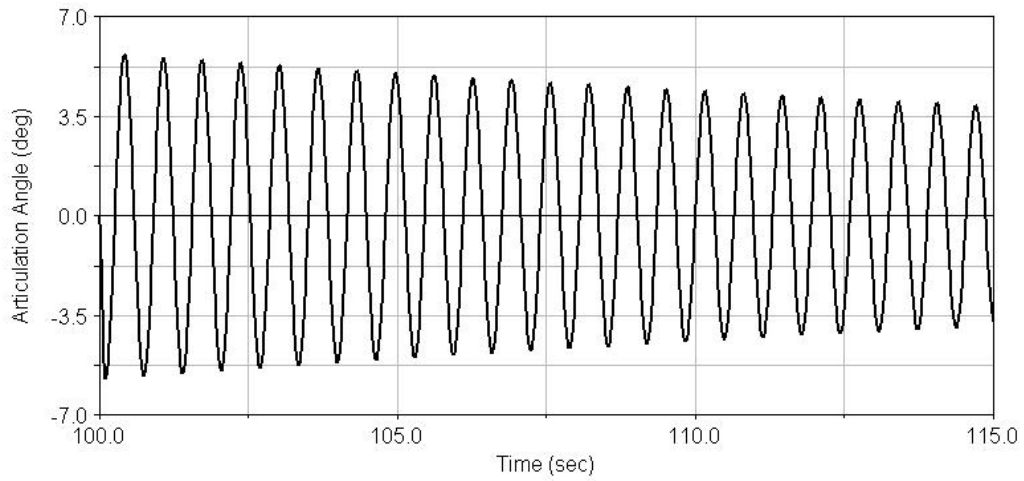
Figure 3-35: Articulation angle in response to an external disturbance for $K_R = 3.5 \times 10^5$ Nm/rad, $C_R = 300$ Nms/rad and $u = 5$ m/s.
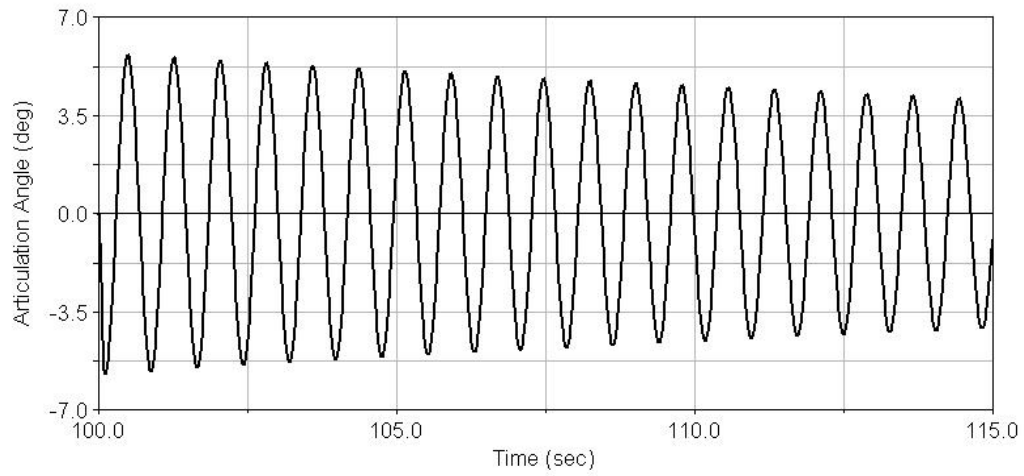
Figure 3-36: Articulation angle for $K_R = 3.5 \times 10^5$ Nm/rad, $C_R = 0$, $C_g = 600$ Nms/rad and $u = 5$ m/s.

3.7   Summary

The analysis of the effects of different parameters and operating conditions on the lateral sta-
bility of an ASV during the snaking mode showed that the straight-line on-highway motion
with constant forward speed was the most critical driving condition. It was shown that the
change in the mass and moment of inertia can change the critical torsional stiffness to some
degree. However, the center of mass positions for the front and rear parts can change the order
of magnitude of the critical torsional stiffness. The front part center of mass position had less
effect on the stability compared with that of the rear part. The results also indicated that, in
addition to the well-rearward center of mass positions for the rear part, the well-forward center
of mass positions for the front part of the vehicle may cause the instability. However, this may
only happen at considerably high speeds, for instance 60 km/h or higher.

To study the effects of locking differentials on stability, the 5-DOF model was generated
based on the previous 3-DOF model. The results showed that locking both front and rear
differentials caused a significant reduction in the critical torsional stiffness. It was shown that
locking both differentials prevented the instability in normal driving conditions. In addition,
locking only one of the differentials also improved the lateral stability of the vehicle during the
snaking mode. Based on the conducted theoretical analysis, locking one or both of the differ-
entials introduced an equivalent damping, similar to the torsional damping at the articulation
joint that dissipated the energy during the snaking mode. However, when both the differentials
were locked, the equivalent damping was increased. Therefore, the snaking oscillations can
be alleviated more effectively in this condition. The 5-DOF model was developed based on
some simplifications. By using the simulation of the motion for the virtual prototype of the
baseline vehicle in ADAMS, it was shown that these simplifications had no significant effect on
the results. The snaking mode is a problem that makes some difficulties for the drivers during
travel at higher speeds on roads and highways, and many manufacturers have tried different
changes to the hydraulic system of the vehicle to alleviate this problem. However, locking the
differentials is a simple and effective method for this purpose, which can be even used on-the-go.

To study the lateral stability of an ASV with a rear-mounted load having interaction with
ground, the 3-DOF model was extended to a 4-DOF model. Some assumptions were considered
to develop this model. For instance, the normal force at the tires and load-ground contact

area was assumed to be constant. A stability analysis of the straight-line motion of the baseline vehicle was presented by using the eigenvalues of the system. The results showed that, when the vehicle was carrying a rear-mounted load, unstable snaking oscillations occurred if the travel was on a relatively good off-road surface and the torsional stiffness or damping at the articulation joint was very small. However, when the torsional stiffness or damping at the articulation angle was increased, the snaking oscillations were removed or delayed to higher speeds. This can be also achieved if the torsional damping at the grapple joint is increased. To verify the results from the analysis of the 4-DOF model, the motion of the virtual prototype in ADAMS was simulated for different values of the torsional stiffness and damping at the articulation joint and the torsional damping at the grapple joint. The off-road tire model based on the mobility number was also linked to the virtual prototype. The results from the simulations and the stability analyses were reasonably consistent. They both indicated the important effects of the torsional stiffness and damping at the articulation joint and also the torsional damping at the grapple joint on the lateral stability. These results were expected regarding the important effects of the steering system characteristics on the stability for the vehicle without load, which was discussed before. For the time being, with regard to the current operation of the baseline vehicle for carrying logs, which is mostly on soft soils with differentials locked and considerable damping at the grapple joint, the instability during the snaking mode is not a problem. However, for future applications of this type of vehicle at higher speeds and on good surfaces such as dry and firm soils or unpaved roads, it may be a problem.

Chapter 4

Design and Evaluation of Stability Control Systems

In the previous chapters, the studies focused on identifying the causes of the instability during the snaking mode and the effects of different parameters and operating conditions on the stability. These studies showed that a conventional ASV is more prone to the instability in on-highway travel at higher speeds. Such concerns are very important for highway traffic safety as there is no guarantee of an appropriate driver response to dangerous situations. In view of a gradual increase in operating speeds of ASVs, it is essential to address this undesirable dynamic behavior to avoid loss-of-control accidents as these vehicles move from one job site to another on public roads and highways. Regarding the instability during the snaking mode, some studies have indicated the use of passive methods to alleviate the problem. These methods are mostly based on some changes in the steering system. However, the review of the research literature on lateral stability of conventional ASVs clearly shows that no attention has been paid to the development of more effective methods for stability control.

Stability control systems for wheel steer vehicles were introduced to the market two decades ago. These systems are used to lead the vehicle to predictable behavior and to prevent the vehicle from spinning and drifting out by influencing the vehicle yaw rate so that the drivers have better control on the vehicle. Two main techniques are commonly used for yaw moment control. The first technique is introducing an additional steer angle to the front or rear wheels, called

active front or rear steering. Improved vehicle dynamics, increased safety, enhanced comfort and compact packaging are new features that are all incorporated into active steering systems for wheel steer vehicles [43]. The second technique is generating a yaw moment by producing different values of driving or braking force on the two sides of the vehicle. Depending on the type of the longitudinal force (driving or braking), the technique is called torque vectoring or differential braking. Integrated stability control systems, resulted from combining the two above techniques, have been also proposed by some researchers [44, 45].

One of the challenging issues in development of vehicle stability control systems is the controller design. Any reliable controller for such a system must be developed with regard to existing uncertainties of parameters of the vehicle and its subsystems. Regarding the highly variable operating condition of ASVs, the controller design will be a crucial subject. In this chapter, the shortcomings of using passive methods to stabilize the baseline vehicle during the snaking mode by making some changes in the steering system are indicated. Then, commonly used active strategies for stabilizing the baseline vehicle, including active steering, torque vectoring and differential braking, are investigated. The studies are concentrated on the application of the tire longitudinal forces (torque vectoring and differential braking) for the purpose of stability control. For each strategy, a different controller is utilized and its performance is evaluated. These include classical, robust full-state feedback and robust variable structure controllers. Most of the materials of this chapter were previously published in [46, 47, 48, 49, 50].

4.1   Shortcomings of Stabilization by Passive Methods

Based on previous work, the snaking oscillations can be alleviated to some degree by using passive methods. These methods are based on some changes in the steering system. Therefore, to review the effectiveness of these methods, the 3-DOF model is modified to include the pressure-flow equation of the steering system. Then, using the modified model, the shortcomings of some passive methods, such as introducing friction at the articulation joint and leakage flow across the cylinders for decreasing the snaking oscillations, are indicated.

4.1.1 Equations for Perturbed Motion based on Modified 3-DOF Model

To modify the 3-DOF model, the pressure-flow characteristics of the steering system described by Equation (2.40) are added to the equations of motion, and the torsional spring K_R at the articulation joint is eliminated. However, the torsional damping C_R is still present to introduce the structural damping. In addition, to avoid large numerical errors, a scaled and dimensionless pressure difference variable $\hat{P}_L$ (instead of P_L) is used in the pressure-flow Equation (2.40):

$$\hat{P}_L = \frac{P_L}{\beta_e} \tag{4.1}$$

Therefore, the pressure-flow equation can be rewritten as:

$$K_q x_v = A_e d_j \frac{d\phi}{dt} + (C_{tp} + K_c)\hat{P}_L \beta_e + \frac{V_t}{4} \frac{d\hat{P}_L}{dt} \tag{4.2}$$

Also, the steering torque T_S becomes:

$$T_S = \hat{P}_L \beta_e A_e d_j \tag{4.3}$$

The virtual work δW_S done by T_S is as follows:

$$\delta W_S = T_S \delta \psi - T_S \delta \theta \tag{4.4}$$

The equations of the system can be written in terms of the following state variables:

$$\mathbf{X} = [v, \dot{\psi}, \dot{\phi}, \phi, \hat{P}_L]^T \tag{4.5}$$

The final form of the equations in terms of the state variables can be considered as a linear time invariant (LTI) system described by:

$$\dot{\mathbf{X}} = \mathbf{A}\mathbf{X} + \mathbf{B}U \tag{4.6}$$

The entries for the system matrix $\mathbf{A}$ and the input matrix $\mathbf{B}$ are found in Appendix D, where the input U is the valve displacement x_v.

4.1.2 Analysis of Passive Methods

The parameters of the baseline vehicle are the same as those given in Table 2.6. The tire parameters are also computed for on-highway surface based on the Metz tire model. For the first step, the values of C_R and C_{tp} are assumed to be negligibly small. It is assumed that the baseline vehicle is traveling in a straight line with forward velocity of $u = 12$ m/s. By using the modified model, the articulation angle is simulated in response to an initial condition ϕ_0 $= 0.1$ rad $(5.73°)$, with no input from the steering system $(x_v = 0)$, as shown in Figure 4-1. The response of the vehicle shows a snaking mode for which the amplitude of oscillations is increasing. The snaking oscillations of the baseline vehicle are produced because the equations of motion result in a pair of complex poles with positive real part at $u = 12$ m/s. These unstable poles dominate the response of the vehicle and result in the instability. Now, if the value of structural damping C_R increases to 1×10^3 Nms/rad, the response of the vehicle will be stable, as depicted in Figure 4-2. An increase in C_R results in a negative real part for the dominant oscillatory poles. To increase the value of C_R, some friction pads at the articulation joint can be used. Although this value of C_R is sufficient to decrease the snaking oscillations in this condition, it may be insufficient when the road properties or forward speed change. Therefore, using static friction is not a reliable method to remove the instability.

Now, the effect of introducing leakage flow across the cylinder on the stability is examined. For the neutral position of the steering valve $(x_v = 0)$, when $C_R = 0$ and $C_{tp} = 1 \times 10^{-11}$ m^3/Pa.s, the response to the above initial condition $(\phi_0 = 0.1$ rad$)$ is an unstable snaking mode, as shown in Figure 4-3. For this C_{tp} and pressure difference $P_L = 1 \times 10^7$ Pa, leakage flow across the cylinder Q_L is about 10^{-4} m^3/s. Although this value of Q_L is not very small (about 6 percent of the rated flow of the steering system, $Q_0 = 1.6 \times 10^{-3}$ m^3/s), the instability occurs. In this condition, the response of the vehicle is dominated by a pair of unstable complex poles and a very small negative real pole generated by the pressure-flow equation. If Q_L is increased to more than half of the rated flow of the steering system, the instability still occurs. Therefore, introducing more leakage flow across the cylinder is not always a practical method to decrease the snaking oscillations.

In addition to the external disturbance, the snaking may occur in response to the steering input. The articulation angle in response to a pulsed steering input $\phi_S = 10°$, which is produced
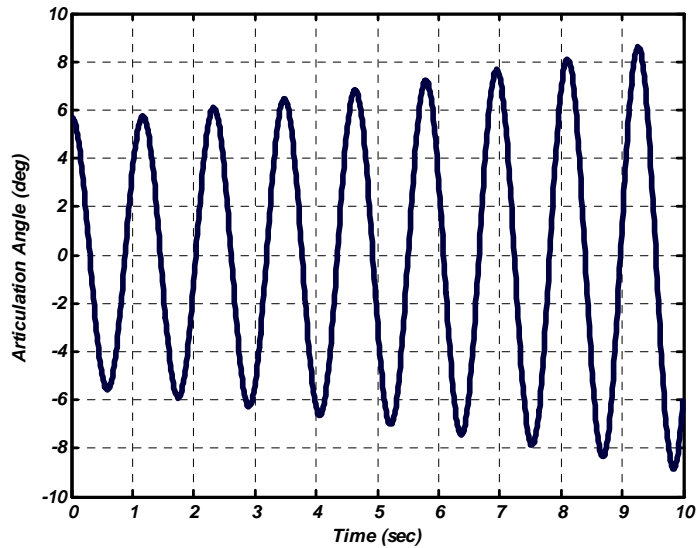
Figure 4-1: Instability of baseline vehicle in response to an initial condition.

by a valve displacement $x_v = 0.463$ mm, is shown in Figure 4-4 for $C_{tp} = 1 \times 10^{-11}$ m^3/Pa.s. The steering response of the vehicle is an unstable snaking mode similar to the disturbance response.

In summary, the use of the passive methods, including static friction and leakage, to remove the instability has the advantage of simplicity. However, there are certain disadvantages, including loss of power in steady-state conditions and an increase in the nonlinearity of the steering behavior (due to nonlinear sliding friction). Most importantly, these methods may not be always reliable or practical methods of stability control.

4.2 Performance of Different Yaw Moment Control Strategies

Regarding the shortcomings of the passive methods, the use of other alternative methods including active yaw moment control strategies should be investigated for the stabilization of the baseline vehicle. However, at the first step, two main strategies for the yaw moment control including change in the steering (articulation) angle by a steering torque and producing a stabilizing yaw moment by generating longitudinal force (driving or braking) at tires are compared.
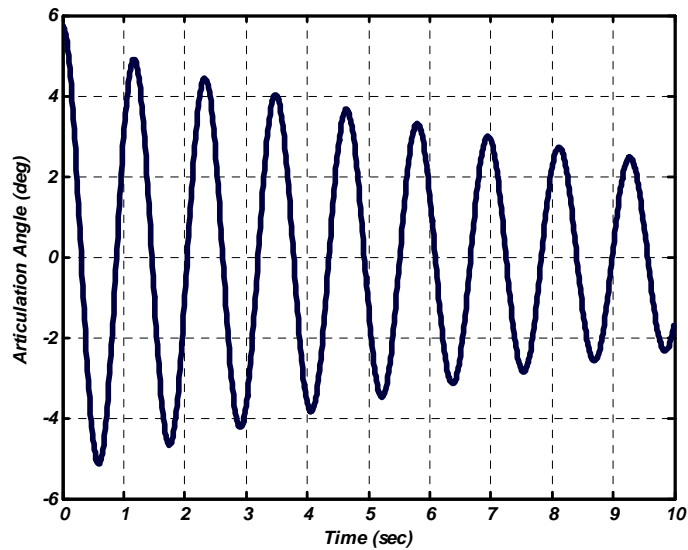
Figure 4-2: Articulation angle in response to an intial condition with $C_R = 1000$ Nms/rad.
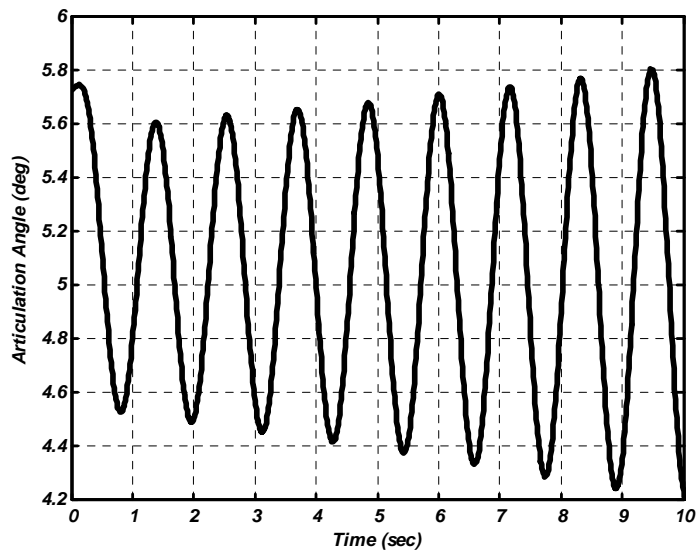
Figure 4-3: Articulation angle in response to an intial condition with $C_{tp} = 1 \times 10^{-11}$ m^3/Pa.s.
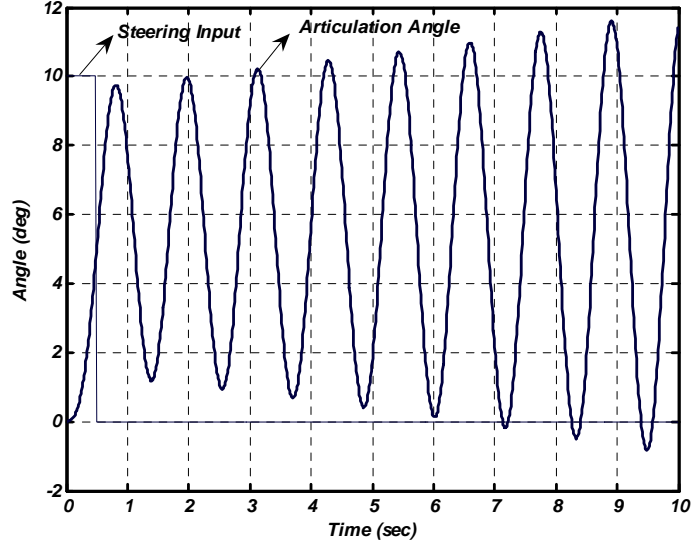
Figure 4-4: Articulation angle in response to steering input with $C_{tp} = 1 \times 10^{-11}$ m^3/Pa.s.

According to Equation (4.4), the steering torque T_S can be used to change the articulation angle for the stabilization of a conventional ASV during the snaking mode. In this condition, when the articulation angle ϕ is increasing, the yaw angles of the both front and rear parts of the vehicle can be reduced by applying an appropriate T_S. This results in a decrease in the slip angles of the both front and rear tires, and thus, the resultant lateral force at the front and rear axles is also reduced. Therefore, the snaking oscillations are alleviated. Although this is one method of diminishing the snaking oscillations, a more efficient method for this purpose can be achieved by producing longitudinal tire force at the rear wheels of the vehicle. This method is more efficient for several reasons: first, the resulting yaw moment can be used to prevent an increase in the yaw motion of the rear part, and thus, the slip angles of the rear tires. Therefore, the resultant lateral force at the rear axle is reduced. Moreover, the normal load on the rear axle is usually more than that on the front axle during the snaking mode. This is due to the fact that the snaking oscillations are mainly initiated when a massive rear-mounted attachment shifts the rear part centre of mass position well-backward of the rear axle [3]. Therefore, as the normal loads on the rear wheels are large, high longitudinal tire forces can be also generated at these wheels to stabilize the vehicle. The second factor is related to a

change in the cornering properties of the rear wheels due to the generation of the longitudinal tire forces at these wheels. The generation of the longitudinal tire forces at the rear wheels reduces the cornering stiffness of these tires. This effect also decreases the resultant lateral force at the rear axle. As another advantage, the distance between the tire centerline and the articulation point is typically about three times the distance between the hydraulic cylinder centerline and the articulation point. Therefore, a higher stabilizing moment is produced by using the tire longitudinal force to stabilize the vehicle. Finally, the snaking oscillations are stronger when the vehicle is traveling on surfaces with a larger friction coefficient. Therefore, a higher longitudinal tire force can be produced at the tire and can be used for the stabilization of the vehicle. In brief, the most effective strategy to deal with the instability of conventional ASVs during the snaking mode is the use of longitudinal force at the rear tires.

However, the use of active steering to stabilize conventional ASVs during the snaking mode can be still considered as an alternative. Conventional ASVs are sometimes required to do specific tasks during travel. For some of these tasks, the steering should be accurate and the vehicle should follow a desired path exactly. For instance, when a tractor is used for row crop cultivating, the inter-row maneuverability must be approximately ± 9 cm to prevent overrunning the crop [51]. To improve steering response for this kind of ASV, the use of an active steering system for the vehicle can result in a prompt and accurate steering. Recently, the concept of an electrohydraulic steering system to improve steering performance of ASVs has been proposed [52]. An electrohydraulic valve receives electrical control signals from a controller to adjust the hydraulic pressure to each cylinder. By using this system, the steering jerk can be limited and the articulation angle is adjusted precisely according to the rotation of the steering wheel. The concept has been suggested by considering the regulations that demand a mechanical or hydraulic connection between the steering wheel and the steering actuator in the event of electrical power failure. Therefore, for ASVs demanding a good steering response, the use of active steering for improvement of stability behavior during the snaking mode can be a solution; however, this is not the case for the baseline vehicle. As a result, although a preliminary study is conducted regarding the use of active steering system to stabilize the baseline vehicle, the more detailed investigations are related to the use of longitudinal force at the rear tires for the stabilization.

106

The required longitudinal force at the tires can be produced by applying driving or braking torques. ASVs have very powerful engines, and their powertrains are designed to produce extremely high driving torques at the wheels. To enhance the traction capabilities of four-wheel drive vehicles, they may be equipped with active torque distribution devices, such as electronically-controlled, limited-slip differentials and electromagnetically-controlled couplings [53, 54]. These devices can optimize driving force distribution to all four wheels of the vehicle under different driving conditions. Active torque distribution systems have also been utilized as a basis for designing vehicle stability control systems [18]. These new applications of active torque distribution systems motivate the development of a similar active control system to prevent instability during the snaking mode of the baseline vehicle. As a result, both enhanced traction performance and stability control can be achieved using this type of system. By using a torque vectoring device, both the left and right rear tires can be used to produce the longitudinal force; thus, tire wear is not a big problem. Moreover, as two equal but opposite longitudinal forces can be generated at the left and right tires for the stabilization, the forward speed remains constant. However, for stability control of the vehicle, the input torque from the engine to the rear axle may be insufficient for cases in which the snaking oscillations are very strong. For these cases, extra power should be supplied to the rear axle for the stabilization.

A much simpler method for producing the longitudinal force at the tires is the application of braking torque; however, using this method results in more energy loss by wasting the energy provided for one of the wheels in the form of heat [55]. Despite this shortcoming, in many stability control systems for front wheel steer vehicles, differential braking is a popular strategy to produce the required yaw moment for the control of the directional stability [56]. This is mainly due to the availability of anti-lock braking systems (ABS) and the possibility for easily changing the brake pressure for each wheel. Differential braking can be used to develop a similar active control system to prevent instability during the snaking mode for a conventional ASV, as well. As the braking torque is applied to one individual rear wheel for producing the longitudinal tire force, the required longitudinal force is about two times that for the case of using torque vectoring device. Thus, a larger braking force should be generated, resulting in more tire wear. Although, the forward speed of a wheel steer vehicle may be reduced due to braking force, this effects is not considerable in the case of ASVs, due to their large mass

107

(typically about 14500 kg).

In the following sections, the application of different types of stability control systems as alternative solutions for the stabilization of the baseline vehicle is reviewed.

4.3   Classical Controller for Active Steering System

In this section, the idea of using an active steering system to remove instability during snaking mode for the baseline vehicle is investigated using the previously modified 3-DOF model with the pressure-flow equation of the steering system. To make an active steering system for the vehicle, the sliding valve of the steering system is replaced with an electrohydraulic valve that has the capability of implementing electronic control. It is assumed that the displacement of the valve x_v is adjusted by a controller. Figure 4-5 shows a schematic of an ASV with an active steering system. The user of the vehicle turns the steering wheel to achieve the desired articulation angle ϕ_d. The actual articulation angle ϕ is then fed back and used by the control system to adjust x_v. The steering process continues until ϕ_d is achieved.

The most commonly used classical controllers for improving the response of a dynamic system are PD, PI, and PID (Proportional+Integral+Derivative control). The PD controller can increase damping in a system, but it has less effect on the steady-state error. The PI controller can improve the relative stability and steady-state error at the same time, but the rise time is increased. By using a PID controller, the best features of each of the PI and PD controllers are utilized. As a representative of the classical controllers, PID controllers have been used in many engineering applications, owing to their essential functionality, structural simplicity and easy application by manual tuning.

If the controller of the active steering system includes only a PID element, the displacement of the electrohydraulic valve x_v is adjusted as follows

$$x_v = P_c(\phi_d - \phi) + I_c \int (\phi_d - \phi)dt + D_c(\dot{\phi}_d - \dot{\phi}) \tag{4.7}$$

where P_c, I_c and D_c are the proportional, integral and derivative gains of the controller, respectively. These gains can be tuned to stabilize the snaking oscillations for a specific condition. Sometimes, the pressure-flow equation of the steering system (Equation (2.40)) introduces a
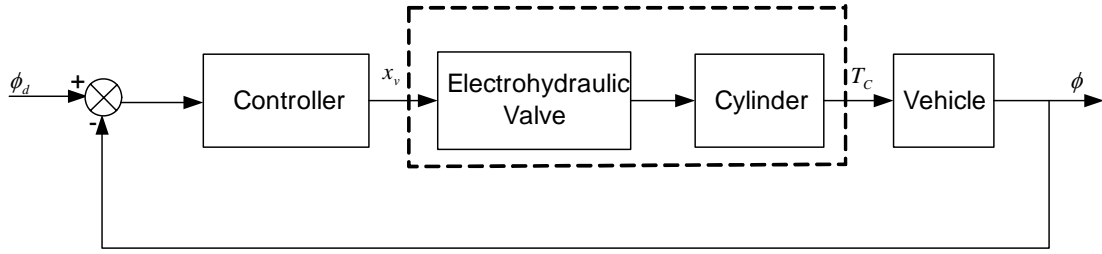
Figure 4-5: A schematic of an ASV with active steering system.

high lag to the system, which can not be compensated by tuning the PID element, and the steering response is not sufficiently prompt and well-damped.

As shown before, the unstable snaking oscillations of the baseline vehicle are due to a pair of complex poles which dominate the response of the vehicle. By using a notch filter in the network of the controller, the undesirable effect of the dominant unstable poles can be reduced. A notch filter consists of a pair of complex zeros and a pair of complex poles, and has the following transfer function [57]:

$$G_n(s) = K_c \frac{s^2 + b_1 s + b_2}{s^2 + a_1 s + a_2} \tag{4.8}$$

where all of the coefficients K_c, b_1, b_2, a_1 and a_2 can be adjusted independently. As long as the notch zeros are close enough to the dominant poles of the system, they can sufficiently reduce their effects. Also, the magnitude of the real value of the notch poles should be large enough to result in a well-damped response. Although the notch filter can remove the instability generated by the dominant unstable poles, the response of the vehicle should also be prompt and well-damped. This can be done in a good way by tuning a PID element. Thus, a stable and acceptable steering response can be achieved by a controller including both a notch filter and a PID element. By using MATLAB, the coefficients of these elements which are given in Table 4.1, are tuned to obtain the desirable response for the on-highway travel at $u = 12$ m/s. The response of the vehicle for a pulsed steering input $\phi_d = 10°$ is shown in Figure 4-6. The response is stable with no snaking oscillations. The step steering response of the vehicle for $\phi_d = 15°$ is also plotted in Figure 4-7. The resulting steering response is stable and sufficiently prompt.

109

Based on the simulations, the developed controller works satisfactorily for many other operating conditions, when the parameters of the vehicle or its subsystems, such as rear part moment of inertia, forward speed or tire parameters change. This is due to the fact that the dominant poles of the resulting closed-loop system are chosen in such a way that the parameter variations do not affect them significantly. However, the controller is highly conservative and the required flow to stabilize the vehicle in the critical conditions may be as many times as the maximum flow of the existing hydraulic system of the vehicle. This means that some extra elements should be added to the hydraulic system of the vehicle to provide the required flow. Moreover, there are many unknown factors affecting the vehicle dynamics due to the operation with different attachments and on unpredictable and time-varying terrains that may deteriorate the performance of the controller. Therefore, design of robust controllers for the stabilization of the baseline vehicle must be taken into account.

As shown before, the most critical driving condition for a conventional ASV is the straight-line travel with constant forward speed. For a given straight-line motion with constant forward speed, all the vehicle parameters are constant, except for the tire parameters, as the road surface may change. These parameters may change rapidly when the vehicle is moving from one job site to another. In practice, many factors, such as inflation pressure, normal load, nonlinearity and so on affect these parameters. In general, tire parameters represent the most important source of uncertainties of models for road vehicles. Thus, the controller must be robust against these uncertain time-varying parameters. Also, although other parameters of the vehicle, for instance mass properties, are constant for a given straight-line motion with constant forward speed, they can take different values for different motions. Therefore, the controller should be robust when these unknown constant parameters change, as well, for instance, when the vehicle is carrying a long rear-mounted attachment.

For the straight-line travel with constant forward speed, the dynamic system of a conventional ASV can be adequately represented by a dominant nominal system plus time-varying unknown terms resulting from the uncertain tire-road contact parameters. As the bounds on the uncertainties are known, two popular techniques for designing a deterministic stability control of the vehicle are present. These design techniques are both based on the Lyapunov second theorem on stability [58]:

PID	Value	Notch filter	Value
P_c	10	K_c	1.5
I_c	0.01	b_1	6
D_c	2.5	b_2	9
		a_1	120
		a_2	3600

Table 4.1: Parameters of classical controller for active steering system.
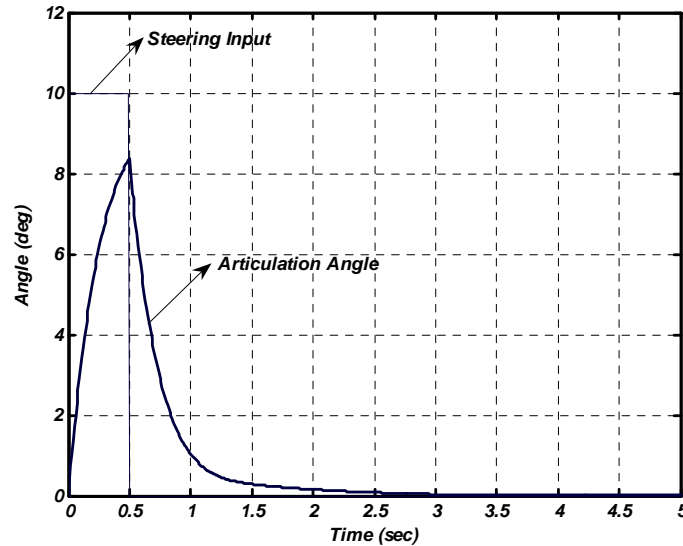
Figure 4-6: Articulation angle in response to a pulsed steering input.

(I) Design by finding a Lyapunov function

(II) Design of a Variable Structure Control (VSC)

The use of these techniques to design a robust controller for the stability control system of the baseline vehicle is the focus of the following sections.

4.4   Robust Feedback Controller for Torque Vectoring System

Many active torque managing devices that include electronically controlled differentials and couplings, overdriven and torque vectoring differentials, and engine control systems have been developed to control torque distribution between, as well as across axles. By using these active
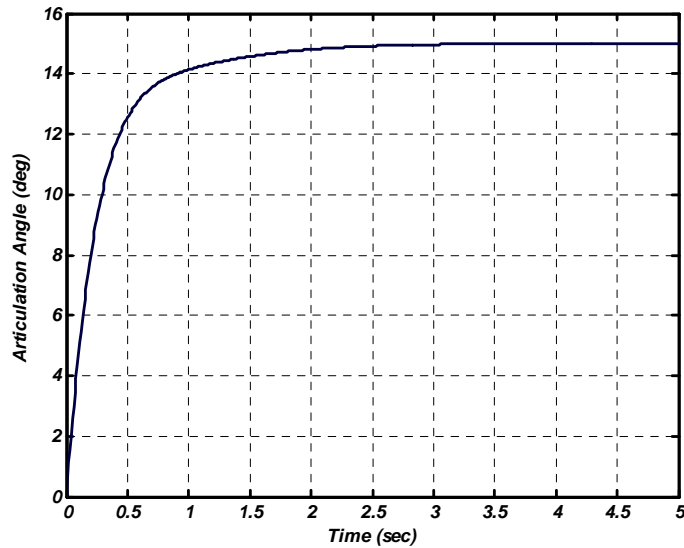
Figure 4-7: Articulation angle in response to step steering input.

devices, the driving torque can be distributed independently among all the wheels, depending on driving condition. The driveline system is adaptive, and can be like an open ordinary differential, a locked differential, or a limited-slip differential. In addition, the input torque can be delivered to the wheels of a given axle with different values, and the input power from the engine can be adjusted and delivered to one or both of the axles with any desirable ratio. Obviously, these devices are more advantageous for enhancing the traction capabilities of ASVs with regard to their heavy-duty applications, than with front wheel steer vehicles. At the same time, these devices can be utilized to improve the stability behavior of conventional ASVs during snaking mode.

In this section, a torque vectoring device equipped with a robust full-state feedback controller to accommodate the uncertainties is designed for the stabilization of the baseline vehicle. First, the 3-DOF model is modified to include the rotational dynamics of the four wheels of the vehicle. This is due to the fact that the rotation angles of the wheels are changed by applying the torque vectoring device. The resulting 7-DOF model is then examined to identify the most important uncertain tire parameters. The equations of motion for this model are represented in the form of a polytope system, which depends affinely on the most important uncertain tire

parameters. Then, the Lyapunov function and state feedback matrix of the controller are found by solving some Linear Matrix Inequalities (LMIs) in MATLAB. Finally, to verify the results from the 7-DOF model analysis, simulations are performed using the virtual prototype of the vehicle, to which the active torque vectoring device is connected.

4.4.1 7-DOF Model of Vehicle with Wheel Rotational Dynamics

The 3-DOF model can be extended to include the rotations of the four wheels of the vehicle, as shown in Figure 4-8. As a result, four additional degrees of freedom are introduced to the system. As the previous cases, it is assumed that the tire rolling resistance and aerodynamic forces are negligibly small and the road is flat. Therefore, the input driving torque from the engine will be zero for constant speeds during a straight line motion. During the perturbed motion, the yaw motions of the front and rear parts of the vehicle result in a longitudinal slip at the four wheels, and thus the longitudinal tire force. By controlling the direction and magnitude of the resulting longitudinal tire forces at the left and right wheels of the rear axle, the produced yaw moment can be used to stabilize the snaking oscillations. The control of the longitudinal tire force at the rear wheels can be achieved by applying equal but opposite torque ΔT to these wheels, which will be a basis for the stability control system of the vehicle by its torque vectoring device.

4.4.2 Equations for Perturbed Motion

For the resulting 7-DOF model, the following coordinates are used to describe the configuration of the system:

$$\mathbf{q} = [X_1, Y_1, \psi, \theta, \theta_1, \theta_2, \theta_3, \theta_4] \tag{4.9}$$

where θ_1, θ_2, θ_3 and θ_4 represent the spin rotation angle of the right and left front and rear wheels, respectively. To derive the equations of motion, the gyroscopic effects are neglected and the axles and wheels are assumed lumped with their respective parts. As shown previously, the longitudinal tire forces produced at the tires introduce the virtual work δW_l to the system, according to Equation (3.1). These forces, together with the applied input torque ΔT, change
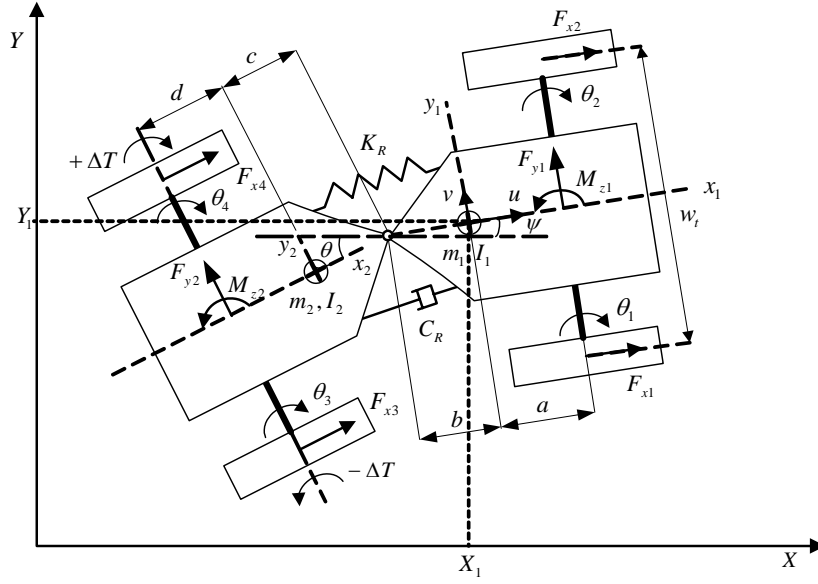
Figure 4-8: A model of an ASV with considering wheel rotational dynamics.

the rotational motion of the wheels ($\theta_1, \theta_2, \theta_3$ and θ_4), and introduce another virtual work δW_r described by:

$$\delta W_r = -(F_{x1}\delta\theta_1 + F_{x2}\delta\theta_2 + F_{x3}\delta\theta_3 + F_{x4}\delta\theta_4)r_e + \Delta T\delta\theta_4 - \Delta T\delta\theta_3 \qquad (4.10)$$

Therefore, the seven corresponding generalized forces and moments are:

$$Q_Y = F_{y1} + F_{y2} \qquad (4.11)$$

$$Q_\psi = aF_{y1} - bF_{y2} + M_{z1} + (F_{x1} - F_{x2})\frac{w_t}{2} \qquad (4.12)$$

$$Q_\theta = -(c+d)F_{y2} + M_{z2} + (F_{x3} - F_{x4})\frac{w_t}{2} \qquad (4.13)$$

$$Q_{\theta_1} = -F_{x1}r_e \qquad (4.14)$$

$$Q_{\theta_2} = -F_{x2}r_e \qquad (4.15)$$

$$Q_{\theta_3} = -F_{x3}r_e - \Delta T \qquad (4.16)$$

114

$$Q_{\theta_4} = -F_{x4}r_e + \Delta T \tag{4.17}$$

Also, the longitudinal wheel slips are:

$$S_1 \approx -\frac{u + \frac{w_t}{2}\dot\psi - r_e\dot\theta_1}{u} \tag{4.18}$$

$$S_2 \approx -\frac{u - \frac{w_t}{2}\dot\psi - r_e\dot\theta_2}{u} \tag{4.19}$$

$$S_3 \approx -\frac{u + \frac{w_t}{2}\dot\psi - r_e\dot\theta_3}{u} \tag{4.20}$$

$$S_4 \approx -\frac{u - \frac{w_t}{2}\dot\psi - r_e\dot\theta_4}{u} \tag{4.21}$$

In the resulting equations of motion, the spin angles of the wheels θ_1, θ_2, θ_3 and θ_4 are not present, therefore, the rotational dynamics of the wheels can be represented by a set of first order equations. In addition, by using the new variables ϖ_1, ϖ_2, ϖ_3 and ϖ_4, instead of $\dot\theta_1$, $\dot\theta_2$, $\dot\theta_3$ and $\dot\theta_4$, the above equations (4.18 to 4.21) are changed to a suitable form for the state-space representation by eliminating u from the numerator:

$$\varpi_1 = \dot\theta_1 - \frac{u}{r_e} \tag{4.22}$$

$$\varpi_2 = \dot\theta_2 - \frac{u}{r_e} \tag{4.23}$$

$$\varpi_3 = \dot\theta_3 - \frac{u}{r_e} \tag{4.24}$$

$$\varpi_4 = \dot\theta_4 - \frac{u}{r_e} \tag{4.25}$$

Also, the four first order equations of motion for the wheels can be replaced by two equations in terms of the following variables:

$$\varpi_f = \varpi_2 - \varpi_1 \tag{4.26}$$

$$\varpi_r = \varpi_4 - \varpi_3 \tag{4.27}$$

Finally, the following six state variables are enough to derive the equations of motion:

$$\mathbf{X} = [v, \dot{\psi}, \dot{\phi}, \phi, \varpi_f, \varpi_r]^T \tag{4.28}$$

The final form of the equations in terms of the state variables is:

$$\dot{\mathbf{X}} = \mathbf{A}\mathbf{X} + \mathbf{B}U \tag{4.29}$$

The entries for the system matrix $\mathbf{A}$ and input matrix $\mathbf{B}$ are found in Appendix E. The input U is ΔT, the transferred torque from one wheel to another one at the rear axle. By designing a proper controller, the transferred torque ΔT can be adjusted to stabilize the baseline vehicle during the snaking mode. The transferred torque ΔT can be found based on a full state feedback as follows:

$$\Delta T = \mathbf{K}\mathbf{X} \tag{4.30}$$

where $\mathbf{K}$ shows the feedback matrix, and must be found for the robust stabilization of the vehicle.

The difference between the resulting equations for the 7-DOF model and those for the 3-DOF model affects the critical speed of the vehicle u_{cr}. To find u_{cr} based on the 7-DOF model ($C_R = 0$, $K_R = 1 \times 10^5$, $I_e = 574$ kgm^2, $r_e = 0.94$ m and the nominal parameters of the vehicle given in Table 2.6), the eigenvalue results in terms of forward speed are plotted. The tire parameters take their values for on-highway travel based on the Metz tire model. The system has a pair of dominant eigenvalues with positive real parts for the forward speed $u_{cr} \approx 12$ m/s and higher, as shown in Figure 4-9. This indicates that the critical speed predicted by the 7-DOF model is higher than that predicted by the 3-DOF model ($u_{cr} \approx 10$ m/s). As a result, the longitudinal forces produced at the tires during the snaking mode result in a stabilizing turning moment, which increases the critical speed.

4.4.3 Range of Uncertainty in Tire Parameters

When the baseline vehicle is travelling at a constant forward speed, all the parameters of the vehicle, such as mass and moment of inertia, are constant. However, the road surface may change; for instance, from a hard on-highway surface to a surface covered with gravel, or from
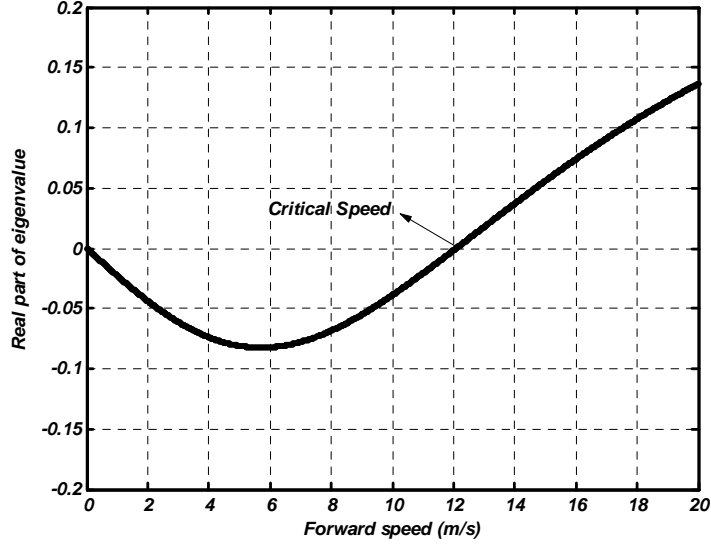
Figure 4-9: Eigenvalue results for baseline vehicle with considering wheel rotational dynamics.

a dry to a wet surface, and thus, the tire parameters will also change. In addition to the above uncertainties in practice, the theoretical equations based on a proposed tire model introduce another type of uncertainty to these parameters due to the different tire parameters that may be obtained based on different tire models. A different value for the tire parameters may result in a completely different response for the vehicle during the snaking mode. Therefore, a robust controller is required to accommodate the uncertainties of the tire parameters. Two steps are required to analyze the effects of these uncertainties on the vehicle dynamics. First, the most significant tire parameters on the lateral stability must be identified. Then, the controller must be designed with consideration of the range of the possible changes in these important tire parameters.

In the equations of motion for the 7-DOF model, C_{sf}, C_{sr} (the longitudinal slip stiffness of the front and rear tires, respectively) and $C_{\alpha f}$, C_{Tf}, $C_{\alpha r}$, C_{Tr} (the effective cornering stiffness and effective aligning stiffness for the front and rear axles, respectively) are related to the tire-road contact. To obtain the previous eigenvalue results from the 7-DOF model, these parameters were set to their corresponding values for an on-highway surface. Generally, for this surface, $C_{\alpha f}$ and $C_{\alpha r}$ have their maximum values, which are reduced during travel on other

117

surfaces and, due to this reduction, the snaking oscillations are alleviated. This effect can be recognized in Figure 4-10. When $C_{\alpha f}$ and $C_{\alpha r}$ are about 90 percent of their maximum values, the critical speed is very close to that for their maximum values (according to 100 percent in Figure 4-10). However, for the lower values, the critical speed increases significantly. When $C_{\alpha f}$ and $C_{\alpha r}$ are reduced to 62 percent of their maximum values (for instance, on an off-road surface), the vehicle will be stable over the whole range of its operating speed (until $u = 60$ km/h or 16.7 m/s). The pneumatic trail that is the distance between the tire lateral force and the centre of the tire-road contact area was set to about 17 percent of the length of contact area to reach the previous results, based on the Fiala tire model. However, some models predict that the pneumatic trail is about 25 percent of the length of contact area [21], which is a more realistic value. If this value is used to calculate C_{Tf} and C_{Tr}, the vehicle will be stable over the whole range of its operating speeds during on-highway travel. However, when the slip angle increases slightly, the pneumatic trail will decrease, and it may reach about 17 percent of the length of contact area for the small perturbations. This may promote the snaking oscillations by reducing the critical speed, as shown in Figure 4-11. Finally, the longitudinal slip stiffness for the front and rear tires, C_{sf} and C_{sr} were considered to be 20 percent higher than their respective cornering stiffness. However, these values may be about 0-50 percent more than their respective cornering stiffness, due to the tire construction and other factors [21]. When C_{sf} and C_{sr} change in this range, the critical speed of the vehicle does not change considerably, as shown in Figure 4-12. In summary, the conducted analyses show that the uncertainties in C_{sf} and C_{sr} do not have a significant effect on lateral stability during the snaking mode. However, the uncertainties in $C_{\alpha f}$, $C_{\alpha r}$, C_{Tf} and C_{Tr} do have considerable effects on the stability behavior of the vehicle and must be considered in the design of the controller.

4.4.4   Robust State Feedback Controller Design

As mentioned previously, to guarantee the stability of the baseline vehicle in the presence of uncertainties, the controller should be robust. To design a robust controller, the uncertainties must first be represented by a polytopic or norm-bounded characterization. Generally, a polytopic characterization of uncertainties results in less conservative controller designs compared with norm-bounded characterization [59]. The important case of interval matrices can be
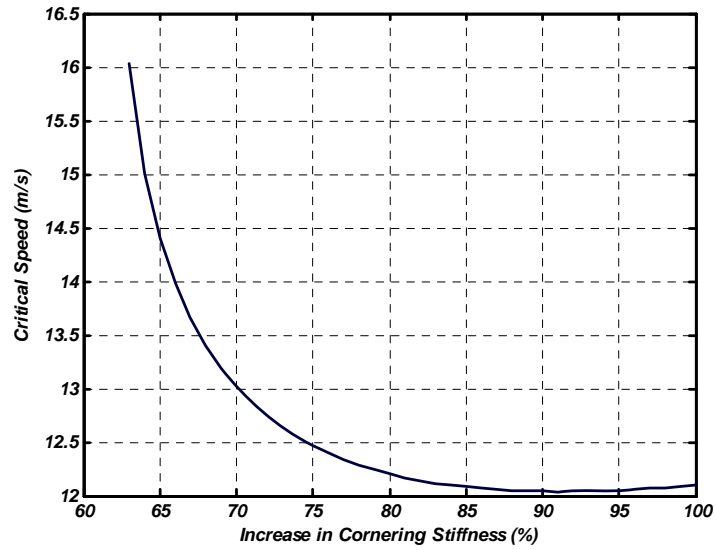
Figure 4-10: Effect of cornering stiffness on critical speed of baseline vehicle.
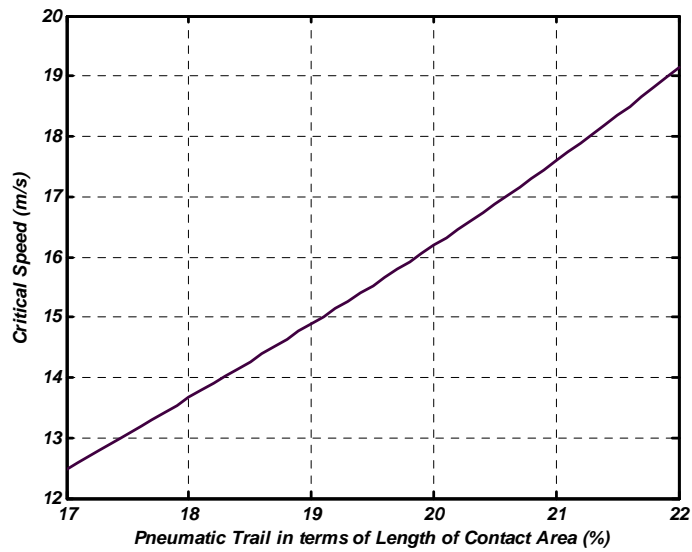
Figure 4-11: Effect of pneumatic trail on critical speed of baseline vehicle.
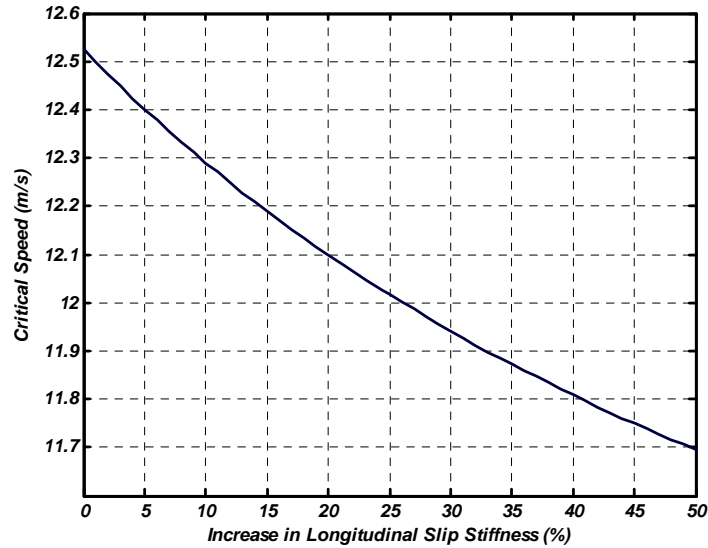
Figure 4-12: Effect of longitudinal slip stiffness on critical speed of baseline vehicle.

exactly modelled using the polytopic characterization. However, the norm-bounded characterization may introduce some dependencies among the parameters for this case, and this leads to an approximate representation of the uncertain domain [60]. A robust controller for stabilizing the uncertain system of the baseline vehicle can be designed by finding a Lyapunov function. For doing this, a polytopic characterization of the uncertainties of the parameters related to tire-road contact is required. In the following, a brief review of the theoretical background of the subject is presented.

Quadratic Stabilization of Polytopic Systems

Clearly, there is a difference between Linear Time-Varying (LTV) and Linear Time-Invariant (LTI) systems for stability analysis. To examine the stability of LTI systems, the real parts of the eigenvalues of the system can be considered as the stability criterion. For LTV systems, for instance the dynamic system of a conventional ASV, even if the real parts of the eigenvalues of the system are all negative for any given time, the system may be unstable. Therefore, the use of Lyapunov functions for examining the stability of LTV systems has been proposed by researchers [61]. More specifically, for uncertain LTV systems, undertaking the stability

120

analysis by constructing a suitable quadratic Lyapunov function is a popular approach. This leads to the concept of quadratic stability as follows.

Consider the following LTV system:

$$\dot{\mathbf{X}}(t) = \mathbf{A}(t)\mathbf{X}(t) \tag{4.31}$$

By definition, this system is quadratically stable if there is a quadratic Lyapunov function $L(\mathbf{X}) = \mathbf{X}^T\mathbf{P}\mathbf{X}$, where $\mathbf{X}^T$ is the transpose of $\mathbf{X}$, and $\mathbf{P}$ is a positive definite matrix $(\mathbf{P} > \mathbf{0})$ with constant arrays. This results in:

$$\dot{L}(\mathbf{X}) = \mathbf{X}^T[\mathbf{A}^T(t)\mathbf{P} + \mathbf{P}\mathbf{A}(t)]\mathbf{X} \tag{4.32}$$

Therefore, the above LTV system is quadratically stable if and only if there is a constant matrix $\mathbf{P} > \mathbf{0}$ and:

$$\mathbf{A}^T(t)\mathbf{P} + \mathbf{P}\mathbf{A}(t) < \mathbf{0}, \qquad \forall\, t\, \epsilon\, \mathbb{R}^+ \tag{4.33}$$

Thus, all trajectories of this system converge to zero as $t \rightarrow \infty$, which indicates a uniformly asymptotic stability [61]. Now, the stability of polytopic linear systems is described. Consider the following linear time-varying system in the state-space form:

$$\dot{\mathbf{X}}(t) = \mathbf{A}(t)\mathbf{X}(t) + \mathbf{B}(t)U(t) \tag{4.34}$$

where $\mathbf{A}(t)$ and $\mathbf{B}(t)$ include r time-varying parameters $p_i(t)$ $(i = 1, ..., r)$ and each $p_i(t)$ is bounded by its extreme values:

$$p_i^{\min} \leq p_i(t) \leq p_i^{\max} \tag{4.35}$$

If there are constant matrices $\mathbf{A}_0$, $\bar{\mathbf{A}}_i$, $\mathbf{B}_0$ and $\bar{\mathbf{B}}_i$ such that $\mathbf{A}(t)$ and $\mathbf{B}(t)$ can be represented for all time by the following equations:

$$\mathbf{A}(t) = \mathbf{A}_0 + \sum_{i=1}^{r} \bar{\mathbf{A}}_i p_i(t) \tag{4.36}$$

121

$$\mathbf{B}(t) = \mathbf{B}_0 + \sum_{i=1}^{r} \bar{\mathbf{B}}_i p_i(t) \tag{4.37}$$

By definition, the system introduced in Equation (4.34) will be a polytope of linear systems. To determine the stability of this polytopic system, its vertices, $(\mathbf{A}_1, \mathbf{B}_2), (\mathbf{A}_2, \mathbf{B}_2), \ldots, (\mathbf{A}_L, \mathbf{B}_L)$, where $L = 2^r$, can be used. These vertices can be found easily when r time-varying parameters $p_i(t)$ take their extreme values ($p_i^{\min}$, $p_i^{\max}$) [59]. The above-mentioned polytope system is quadratically stable if and only if there is a Lyapunov matrix $\mathbf{P} > \mathbf{0}$ such that [62]:

$$\mathbf{A}_j^T \mathbf{P} + \mathbf{P} \mathbf{A}_j < \mathbf{0}, \qquad j = 1, ..., L \tag{4.38}$$

where, each $\mathbf{A}_j$ shows one vertex of the system. Suppose that the input $U(t) = \mathbf{K}\mathbf{X}(t)$. This system can then be stabilized by state feedback if and only if there is a Lyapunov matrix $\mathbf{P} > \mathbf{0}$ and a feedback matrix $\mathbf{K}$ such that:

$$(\mathbf{A}_j + \mathbf{B}_j \mathbf{K})^T \mathbf{P} + \mathbf{P}(\mathbf{A}_j + \mathbf{B}_j \mathbf{K}) < \mathbf{0}, \qquad j = 1, ..., L \tag{4.39}$$

Boyd et al. [62] introduce a change of variables that converts this inequality to a Linear Matrix Inequality (LMI). A LMI may be presented by an equivalent convex optimization problem that can be solved by various numerical methods starting from an arbitrary initial point and executing a number of iterations in a specific way for converging to a solution. By multiplying $\mathbf{Q} = \mathbf{P}^{-1}$ from both sides of Equation (4.39), the following equation is obtained:

$$\mathbf{Q}(\mathbf{A}_j + \mathbf{B}_j \mathbf{K})^T + (\mathbf{A}_j + \mathbf{B}_j \mathbf{K})\mathbf{Q} < \mathbf{0}, \qquad j = 1, ..., L \tag{4.40}$$

By defining $\mathbf{Y} = \mathbf{K}\mathbf{Q}$ and substituting that in the above equation, the following can be achieved:

$$\mathbf{Q}\mathbf{A}_j^T + \mathbf{A}_j \mathbf{Q} + \mathbf{Y}^T \mathbf{B}_j^T + \mathbf{B}_j \mathbf{Y} < \mathbf{0}, \qquad j = 1, ..., L \tag{4.41}$$

If a $\mathbf{Q} > \mathbf{0}$ and a $\mathbf{Y}$ can be found such that the above LMI holds, the system will be stable and the state feedback matrix $\mathbf{K}$ is calculated from:

$$\mathbf{K} = \mathbf{Y}\mathbf{Q}^{-1} = \mathbf{Y}\mathbf{P} \tag{4.42}$$

State Feedback Matrix for Control of Baseline Vehicle

By using the equations of motion for the 7-DOF model, the dynamics of the baseline vehicle can be described as a polytopic linear system. This representation will be helpful in designing a state feedback control system for the vehicle, as follows. In this system, $\mathbf{A}(t)$ depends affinely on the four uncertain parameters $C_{\alpha f}$, $C_{\alpha r}$, C_{Tf} and C_{Tr} $(r = 4)$:

$$\mathbf{A}(t) = \mathbf{A}_0 + \mathbf{A}_1 C_{\alpha f} + \mathbf{A}_2 C_{\alpha r} + \mathbf{A}_3 C_{Tf} + \mathbf{A}_4 C_{Tr} \tag{4.43}$$

However, $\mathbf{B}$ is a constant matrix, and does not include these uncertain parameters. The range of the uncertain tire parameters can be found based on the previously conducted analysis, as follows:

$$460100 \leq C_{\alpha f} \leq 742100 \tag{4.44}$$

$$477940 \leq C_{\alpha r} \leq 770870 \tag{4.45}$$

$$41122 \leq C_{Tf} \leq 99489 \tag{4.46}$$

$$44571 \leq C_{Tr} \leq 107830 \tag{4.47}$$

By using the extreme values of the uncertain parameters, the system can be described by its vertices $(\mathbf{A}_1, \mathbf{B}_2)$, $(\mathbf{A}_2, \mathbf{B}_2)$,..., $(\mathbf{A}_L, \mathbf{B}_L)$ and LMIs in Equation (4.41) can be solved by using LMI Control Toolbox in MATLAB for finding the state feedback matrix $\mathbf{K}$ [63]. The maximum value of the forward speed of the vehicle is assumed to be $u = 60$ km/h or 16.7 m/s, and the torsional stiffness and damping are set at their minimum values ($K_R = 1 \times 10^5$ Nm/rad, $C_R = 0$). The other parameters of the vehicle are the same as in previous cases. A solution for $\mathbf{K}$ can be found based on the algorithm developed in [63], as follows:

$$\mathbf{K} = 1 \times 10^4 [-0.1481 \ -3.2948 \ -1.4472 \ -3.2759 \ -1.2524 \ 0.1754] \tag{4.48}$$
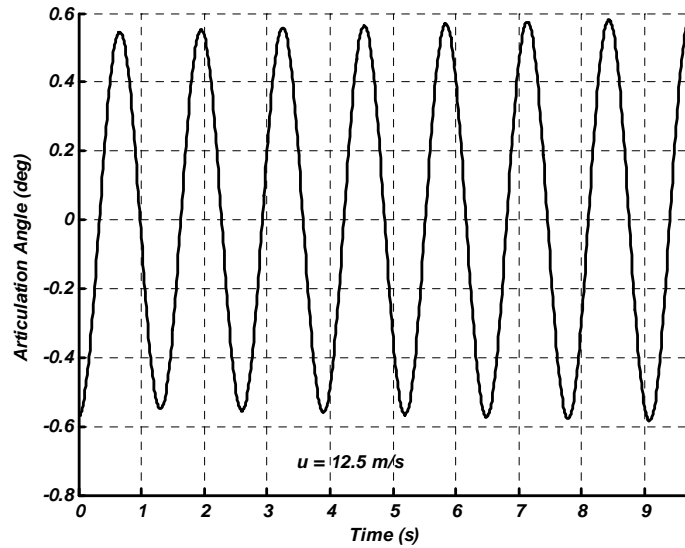
Figure 4-13: Instability of baseline vehicle for $u = 12.5$ m/s.

4.4.5 Evaluation of Controller Performance

By using the resulting feedback matrix $\mathbf{K}$, the baseline vehicle can be stabilized in different driving conditions. As shown previously, if the tire parameters take their nominal values for the highway surface, the vehicle shows instability for the forward speed $u_{cr} \approx 12$ m/s and higher. For example, the change in the articulation angle in response to an initial condition for $u = 12.5$ m/s is shown in Figure 4-13, based on the 7-DOF model. The response is in the form of an undamped oscillatory mode with increasing amplitude. The amplitude of the oscillations is growing, and it would reach $0.6°$ after about 9.7 seconds of the motion. If the controller is activated at this time, the snaking oscillations will be eliminated, as shown in Figure 4-14. The required transfered torque ΔT for stabilization of the vehicle is also shown in Figure 4-15, based on the 7-DOF model.

Now, by using the 7-DOF model, the response of the vehicle is simulated for on-highway travel at 60 km/h (16.7 m/s) for a larger perturbation in the articulation angle. This forward speed is higher than the critical speed of the vehicle; therefore, the amplitude of the snaking mode will grow at a faster rate as shown in Figure 4-16. After ten seconds of this motion, the

124
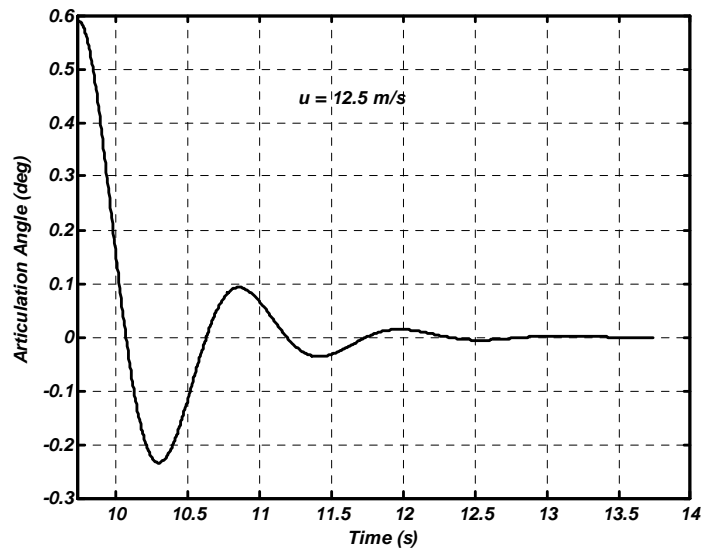
Figure 4-14: Stabilization of baseline vehicle for $u = 12.5$ m/s.
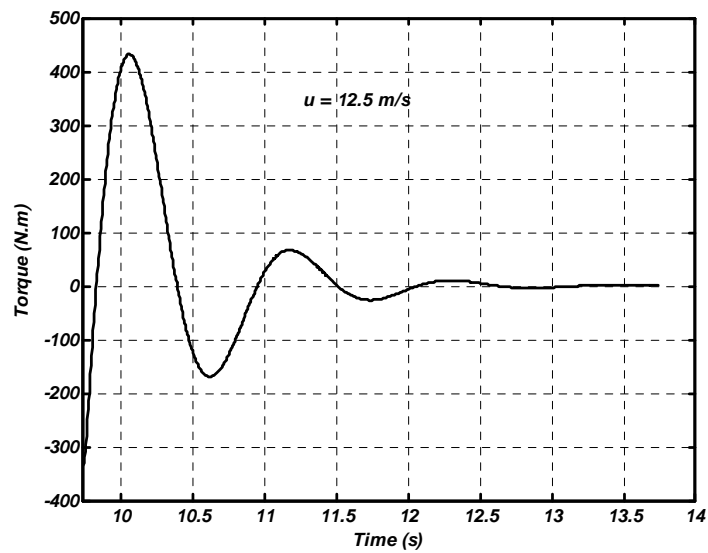
Figure 4-15: Required torque transfer for stabilization of baseline vehicle for $u = 12.5$ m/s.

articulation angle will be about 5° and the vehicle may roll over, with regard to its high speed. If the control system is activated at this time, the instability will be prevented, as shown in Figure 4-17. The required torque transfer to stabilize the vehicle in this condition is shown in Figure 4-18.

There is a difference between the angular velocity of the left and right rear wheels during the snaking mode when the rear differential is free or unlocked. When the torque vectoring device is not present, the angular velocities of the left and right wheels can become the same as each other by locking the rear differential. This results in two reaction torques in the opposite directions at the left and right wheels, and the resulting longitudinal forces at these wheels tend to stabilize the vehicle, as discussed previously. The value of this reaction torque or locking torque is also shown in Figure 4-18. To compute the locking torque in the dynamic equations of the rear wheels, the angular velocities of the left and right wheels are assumed to be the same as each other and the reaction torque is then computed. It is clear that the required torque transfer is less than the locking torque in most cases.

The baseline vehicle can be equipped with different attachments at the front and rear. A rear-mounted attachment has more effect on stability during the snaking mode than a front-mounted attachment. A rear-mounted attachment can change the mass, moment of inertia and the centre of mass position for the whole rear part. In general, a change in the mass has no significant effect on the stability of the vehicle during the snaking mode. However, an increase in the moment of inertia and a well-backward centre of mass position for the rear part may promote the snaking oscillations. To design the controller, the rear part centre of mass position was set to its most critical condition for the various rear-mounted attachments ($d = -0.12$ m). This centre of mass position can be achieved if, for instance, the grapple is placed at its full reach. This long rear-mounted attachment can increase the whole rear part moment of inertia.

For an increase of 1000 kgm^2 in the rear part moment of inertia, the response of the vehicle during on-highway disturbed motion with $u = 60$ km/h is shown in Figure 4-19. After five seconds of this motion, the articulation angle will be about 5° and the vehicle may roll over. If the developed controller is activated at this time, the instability will be prevented, as shown in Figure 4-20. The required torque transfer ΔT to stabilize the vehicle and locking torque are shown in Figure 4-21. The change in the angular velocity of the left and right rear wheels from
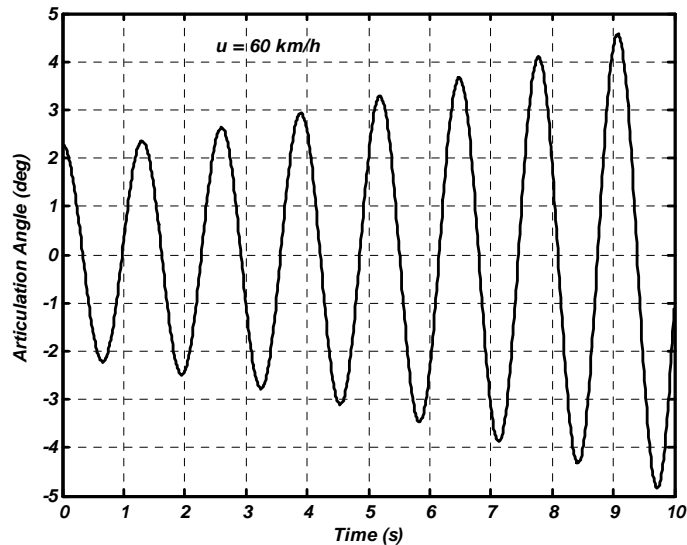
Figure 4-16: Snaking oscillations in response to an initial condition for $u = 60$ km/h.

the initial conditions are shown in Figure 4-22. The changes in the angular velocity of the left and right wheels are similar but occur in opposite directions.

Figure 4-21 shows the required torque transfer to stabilize the vehicle in the most critical driving condition, when the vehicle is travelling at its maximum speed and carrying a long rear-mounted attachment. The locking torque is also shown for any moment of the stabilization in the graph. For many moments, the required torque transfer is less than the locking torque. Therefore, for these times, if the torque vectoring device acts like a limited slip differential, the required torque can be provided, regardless of the driving torques at the wheels. However, for those times when the locking torque is less than the required torque, the driving torque at one wheel should be decreased and the same value should be added to the driving torque at the other wheel using the device. Based on the graph, the maximum transferred torque from one wheel to another is less than 4000 N.m for this case (the first intersection point of two curves). In addition, the average of the angular velocities of the rear wheels is about 17.73 rad/s for the forward speed of 60 km/h. Therefore, the required power at each wheel will be about 71 kW, which means the transferred power to the rear axle should be about 142 kW. For a typical ASV that travels with a forward speed up to 60 km/h, the engine power is more than 200

127
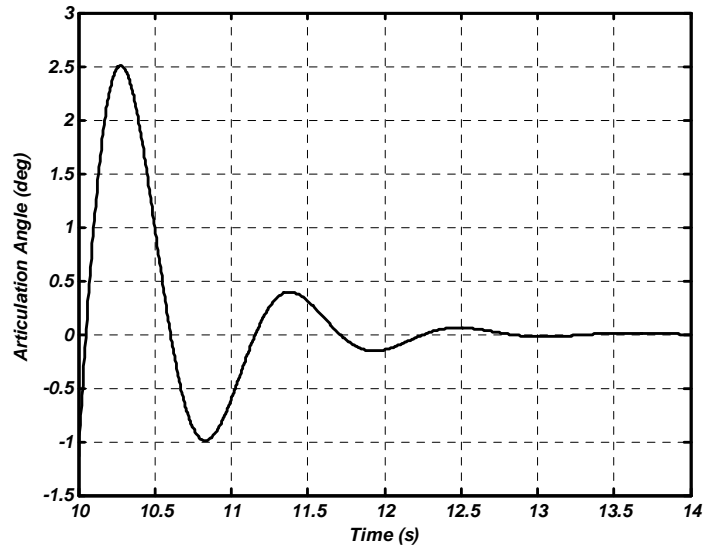
Figure 4-17: Stabilization of snaking oscillations by feedback controller for $u =60$ km/h.
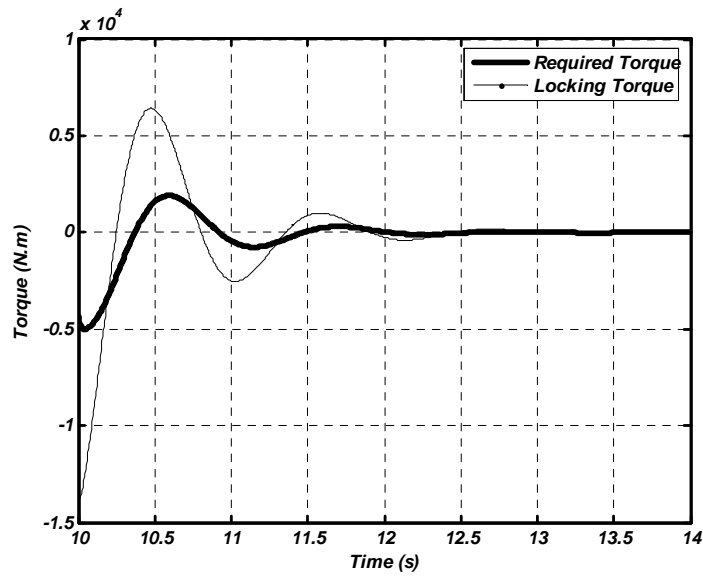
Figure 4-18: Required torque transfer and locking torque for stabilization at $u =60$ km/h.
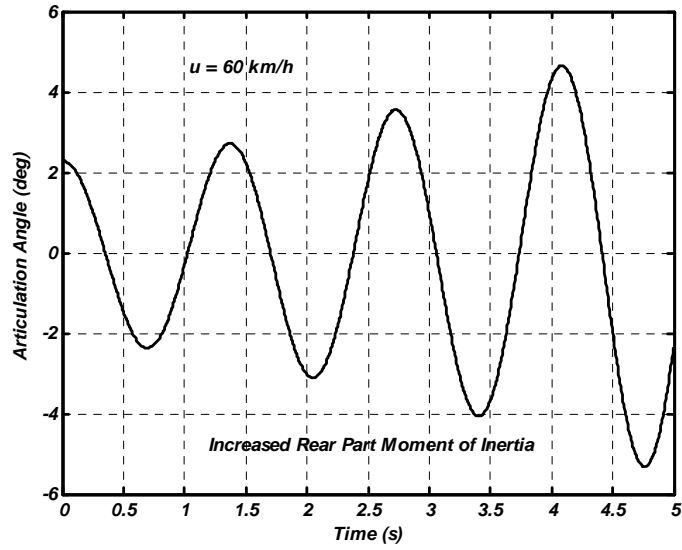
Figure 4-19: Snaking mode for baseline vehicle with a long rear-mounted attachment.
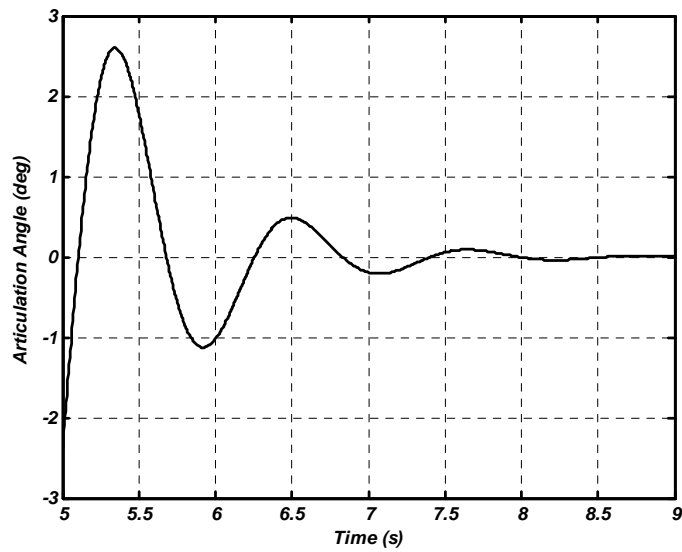
Figure 4-20: Stabilization of baseline vehicle with a long rear-mounted attachment.

129
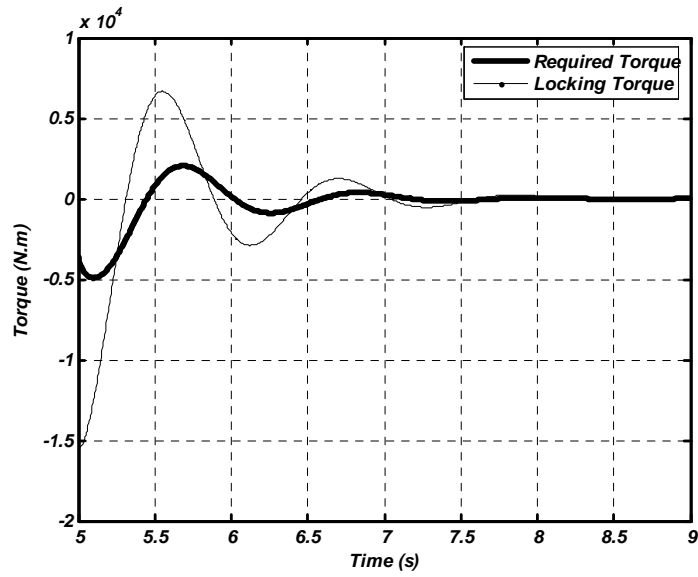
Figure 4-21: Required torque transfer and locking torque for baseline vehicle with its attachment.
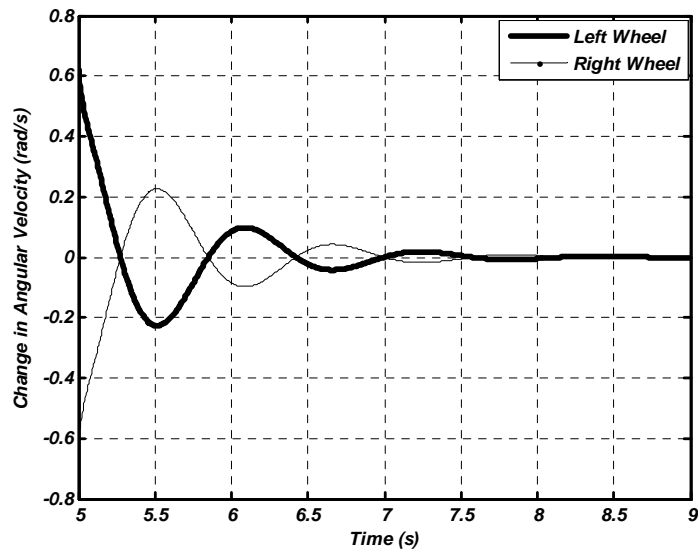
Figure 4-22: Change in angular velocity for left and right rear wheels.

kW. Therefore, the required power is available for stabilizing the vehicle, in the worst case, by application of the torque vectoring device.

Finally, the combination of the vehicle and the stability controller causes a new system. The steering response of the resulting system is also stable, although the stability of the disturbance response was only examined in the previous sections. This is due to the fact that stability is a property of the system, regardless of the nature of the external force or moment applied to the system that can typically be from the road or from the steering by the operator. Moreover, the stability controller must be active when the vehicle is operating at small steering angles, typically $\phi_S \leq 10°$. This range of steering angles is normally used during travel on public roads at higher speeds, which is the most critical driving condition with regard to the stability. As mentioned previously, in the other situations ($\phi_S > 10°$), the instability during the snaking mode is unlikely because the vehicle normally travels at much smaller forward speeds due to the risk of rollover. To deactivate the stability controller for these situations, the angular position of the steering wheel can be measured by a sensor.

4.4.6   Simulation in ADAMS

The analysis of the 7-DOF model shows that for $u = 12.5$ m/s, the instability happens in response to an assumed initial condition during the snaking mode. For this forward speed and the given initial condition, the change in the articulation angle is simulated for the virtual prototype of the vehicle in ADAMS, as shown in Figure 4-23. The response is an undamped oscillatory mode, similar to that for the 7-DOF model. The change in the amplitude of the response is also similar to that for the 7-DOF model (see Figure 4-13). However, the amplitude of the response reaches the same level as that for the 7-DOF model (0.6°) after 9.4 seconds of the disturbed motion, instead of 9.7 seconds. Note that there is a difference about 7 percent between the frequency of the oscillations for the 7-DOF model and that for the virtual prototype. This is mainly due to the fact that the tires have their own mass for the virtual prototype. If the front and rear part mass consist of the mass of their tires, the frequency of the oscillations will be similar to that for the 7-DOF model. The controller is connected to the existing virtual prototype of the vehicle and is activated at this time. This in turn prevents the instability during the snaking mode, as shown in Figure 4-24. The dynamic behavior after the controller
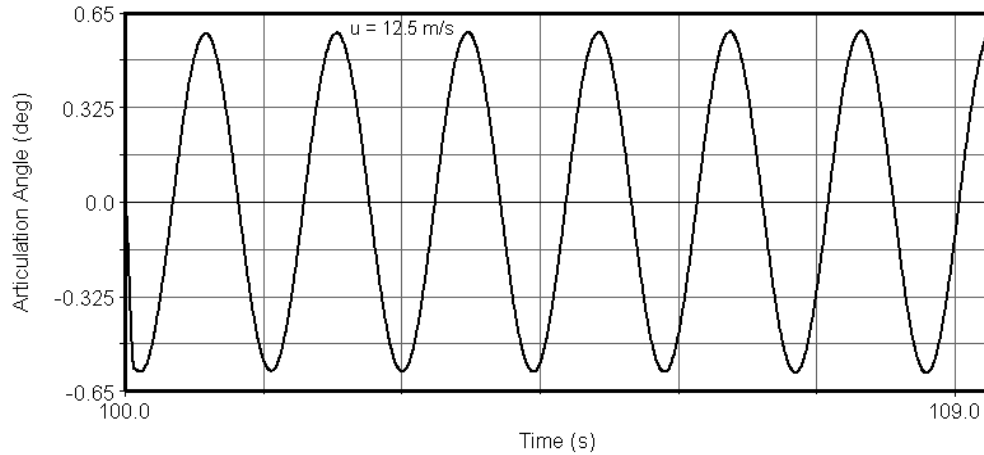
Figure 4-23: Simulation of snaking oscillations for $u = 12.5$ m/s in ADAMS.

is activated is also similar to that for the 7-DOF model (see Figure 4-14). The required torque transfer is also shown in Figure 4-25, which is very close to that shown in Figure 4-15. In summary, the results from the 7-DOF model analysis and those from the simulations in ADAMS are reasonably consistent.

4.5 Robust Variable Structure Control for Differential Braking System

In this section, to remove the instability of the baseline vehicle, the applied braking torque at the rear wheels will be adjusted to produce the required stabilizing yaw moment. Regarding the existing uncertainties, the controller should be designed with robustness as a significant feature. The variable structure control (VSC) on the basis of the sliding mode theory is a common technique to design robust controllers that are suitable for uncertain dynamic systems [64], and thus, is applicable to the dynamics of the baseline vehicle, as well. To design a robust VSC, the input matrix for the 7-DOF is first modified according to the differential braking strategy. The equations of motion are then written in the state-space form in which the uncertain parameters related to tire-road contact appear as some unknown and time-varying terms. These terms introduce a time-varying disturbance function. The bound on the norm of this function can

132
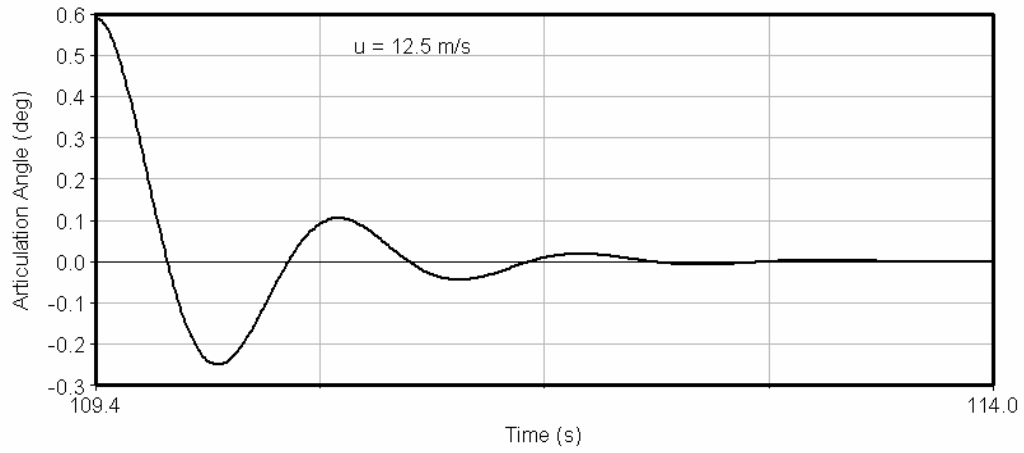
Figure 4-24: Stabilization of baseline vehicle at $u = 12.5$ m/s in ADAMS.
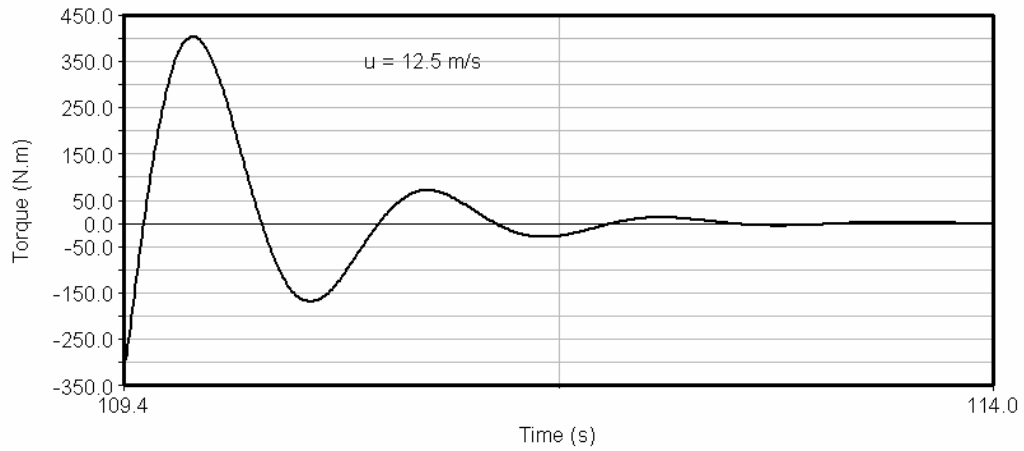
Figure 4-25: Required torque transfer for stabilization at $u = 12.5$ m/s in ADAMS.

be found by the range of the uncertainties, which will be a basis for designing the controller structure. To verify the results from the analysis of the modified 7-DOF model, the motion of the virtual prototype is simulated in ADAMS, to which the controller is connected.

4.5.1 Model Modification for Differential Braking

The 7-DOF model was developed to include the wheel rotational dynamics when applying two equal but opposite torques to the rear wheels. However, the input matrix for this model must be changed for the differential braking strategy (see Appendix E). For this strategy, as shown in Figure 4-26, the differential braking torque ΔT is the input to the system, and can be found by:

$$\Delta T = T_{Br} - T_{Bl} \tag{4.49}$$

where, T_{Br} and T_{Bl} are the braking torque applied to the right and left rear wheels, respectively. The differential braking torques can be provided by applying the braking torques to the rear wheels of the vehicle according to the following rules:

$$\text{For } \Delta T > 0: \quad \Delta T = T_{Br} \text{ and } T_{Bl} = 0 \tag{4.50}$$

$$\text{For } \Delta T < 0: \quad \Delta T = -T_{Bl} \text{ and } T_{Br} = 0 \tag{4.51}$$

4.5.2 Robust Variable Structure Controller Design

In a variable structure control (VSC) system, the control structure is switched when the system state trajectory crosses a certain hypersurface in the state space. When the system trajectory reaches this surface, it is constrained to remain on that, keeping a motion along its trajectory on that surface, the so-called sliding mode [65]. One advantage of this technique is that the dynamics of the system during the sliding mode can be totally determined by choosing the hypersurface [66]. However, in view of the implementation, the main drawback of this technique is chattering due to the discontinuity of the control effort because the switching is not

Figure 4-26: Modified model of an ASV with differential braking.

instantaneous. This undesirable behavior results in high control activity, and may excite the unmodeled high frequency dynamics. To alleviate this problem, the control discontinuity can become smooth in a boundary layer near the hypersurface [61]. Another alternative to remove the chattering is adding an integrator to the control signal; however, this will increase the order by one and the transient response may deteriorate considerably [67].

The VSC technique is a popular method used to provide robustness for the control of uncertain systems, such as spacecraft, power systems and underwater vehicles. For example, this technique has been used for robust control functions of underwater vehicles when the dynamics and operating conditions of the system are changing. Cristi et al. [68] designed both non-adaptive and adaptive VSC systems for an Autonomous Underwater Vehicle (AUV). In their work, the dynamics of the AUV were represented by a dominant single input linear model plus a function denoting the uncertainties. For developing the non-adaptive VSC, the norm on the uncertainty function, including nonlinearities and parameter uncertainties, were assumed to be known. The control law had two different parts, including a linear feedback and a switching

function. The first part of the control determined the desirable dynamics of the system on the sliding surface. The second part was designed to push and maintain the system trajectory on the sliding surface. To design the first part of the control law, conventional methods, such as pole placement, were used.

For the case of the adaptive VSC, the uncertainty function represented the norm-bounded nonlinearities. In addition, the norm on the parameter uncertainties were assumed to be known, and they were also in the range space of the output, so-called matching conditions. In this case, the gains of the feedback part of the controller were updated on-line based on a given law. The VSC was also utilized to design a sliding mode AUV autopilot for the combined steering, diving and speed control functions by Healy and Lienard [69]. The design method was similar to the previous approach; however, the control law consisted of an extra term denoting an estimate of the uncertainty function. Later, the approach proposed by Healy and Lienard was used for designing a VSC system for the control of a flight AUV [70]. The experimental results showed that the resulting controller had more robustness and better performance compared to both classical and fuzzy controllers.

The parameter uncertainty in the dynamic system of the baseline vehicle does not lie in the range space of the input matrix (so-called mismatched uncertainty) [71]; therefore, the adaptive VSC designs proposed in [68, 72] are not applicable to this system. To design a VSC for systems with a specific class of mismatched uncertainties, another adaptive technique has been proposed by Kwan [71]. However, to use this technique, another type of matching conditions for the system is required, which is not the case for many dynamic systems, including the dynamics of the baseline vehicle. For designing an adaptive VSC, an on-line estimation method can be coupled to modify the controller parameters. However, this makes some difficulties, for instance, the stability and convergence of the resulting controller is very difficult to guarantee, more specifically when the signals of the system are not very rich (persistently exciting), leading to the large increase in estimation errors [61]. Moreover, on-line estimation methods in general require enough time for parameter adaptation with good accuracy. More specifically, this is the case during the transient phase, for instance, in the start-up or when the parameters change considerably. On the other hand, the implementation of a VSC in practice, by using a computer and several sensors, is performed at a time interval. If this time interval becomes higher, owing

to an acceptable adaptation and the time delay related to the computations of the estimation process, the VSC system is prone to chattering and instability. Therefore, the non-adaptive VSC presented by Healy and Lienard is used for the robust stability control of the baseline vehicle. Before designing the robust VSC system, a brief explanation of the approach is presented.

VSC Design for single input Systems

Consider a class of single input systems represented by a combination of a dominant linear model and a function representing the uncertainties and nonlinearities:

$$\dot{\mathbf{X}} = \mathbf{A}\mathbf{X} + \mathbf{B}U + \mathbf{F}(\mathbf{X}) \tag{4.52}$$

where, $\mathbf{A}$ and $\mathbf{B}$ are constant matrices, and $\mathbf{F}(\mathbf{X})$ denotes the nonlinearities and parametric uncertainties. The following control U is proposed for stabilizing the system:

$$U = U_l + U_n \tag{4.53}$$

where U_l is the linear part of the control, usually a state feedback law that is called equivalent control. The equivalent control U_l determines the dynamics on the sliding surface. Furthermore, there is a nonlinear switching control law U_n that ensures keeping the state trajectory on the sliding surface in spite of the uncertainties. Now, the method for finding U_l and U_n are described. First, a set of negative eigenvalues λ_i for having a desirable dynamics on the sliding surface are chosen. One of these eigenvalues should be zero. This is consistent with the reduced order dynamics of the system in the sliding mode. By using the pole placement technique for the linear part of Equation (4.52), a feedback vector $\mathbf{K}$, and thus, the linear part $U_l = -\mathbf{K}^T\mathbf{X}$ can be determined so that the closed loop dynamics of the linear part of the system has the specified eigenvalues λ_i. Therefore, based on Equations (4.52) and (4.53):

$$\dot{\mathbf{X}} = \mathbf{A}_C\mathbf{X} + \mathbf{B}U_n + \mathbf{F}(\mathbf{X}) \tag{4.54}$$

where:

$$\mathbf{A}_C = \mathbf{A} - \mathbf{B}\mathbf{K}^T \tag{4.55}$$

If $\mathbf{S}$ is an eigenvector of $\mathbf{A}_C^T$ corresponding to $\lambda = 0$, then:

$$\mathbf{A}_C^T \mathbf{S} = \lambda \mathbf{S} = \mathbf{0} \tag{4.56}$$

Therefore:

$$\mathbf{S}^T \mathbf{A}_C = (\mathbf{A}_C^T \mathbf{S})^T = \mathbf{0} \tag{4.57}$$

The sliding surface σ is defined as follows:

$$\sigma = \mathbf{S}^T \mathbf{X} \tag{4.58}$$

Multiplying Equation (4.54) by $\mathbf{S}^T$:

$$\mathbf{S}^T \dot{\mathbf{X}} = \mathbf{S}^T \mathbf{A}_C \mathbf{X} + \mathbf{S}^T \mathbf{B} U_n + \mathbf{S}^T \mathbf{F}(\mathbf{X}) \tag{4.59}$$

Based on Equation (4.57) and (4.59), this results in:

$$\dot{\sigma} = \mathbf{S}^T \mathbf{B} U_n + \mathbf{S}^T \mathbf{F}(\mathbf{X}) \tag{4.60}$$

If $\hat{\mathbf{F}}(\mathbf{X})$ indicates an estimation of $\mathbf{F}(\mathbf{X})$, the following may be used to determine the discontinuous control U_n:

$$\mathbf{S}^T \mathbf{B} U_n = -\mathbf{S}^T \hat{\mathbf{F}}(\mathbf{X}) - \eta\, sign(\sigma), \qquad \eta \in \mathbb{R}^+ \tag{4.61}$$

where $\eta(t)$ is a positive switching gain, which is determined later. Therefore, Equation (4.60) can be written as:

$$\dot{\sigma} = \mathbf{S}^T [\mathbf{F}(\mathbf{X}) - \hat{\mathbf{F}}(\mathbf{X})] - \eta\, sign(\sigma) \tag{4.62}$$

Defining the following Lyapunov function:

$$L(\sigma) = \frac{1}{2}\sigma^2 \tag{4.63}$$

To guarantee reaching the sliding surface ($\sigma = 0$) globally asymptotic, the condition below must be satisfied:

$$\frac{dL}{dt} = \sigma\dot{\sigma} < 0 \tag{4.64}$$

However, to guarantee reaching the sliding surface in a finite time or having an ideal sliding mode, a stronger condition is required [64]:

$$\sigma\dot{\sigma} \leq -\eta_0\,|\sigma|\,, \qquad\qquad \eta_0 \,\epsilon\, \mathbb{R}^+ \tag{4.65}$$

where η_0 is a positive value. Based on Equation (4.62):

$$\sigma\dot{\sigma} = \sigma\{\mathbf{S}^T[\mathbf{F}(\mathbf{X}) - \hat{\mathbf{F}}(\mathbf{X})] - \eta sign(\sigma)\} \tag{4.66}$$

or

$$\sigma\dot{\sigma} = \sigma\{\mathbf{S}^T[\mathbf{F}(\mathbf{X}) - \hat{\mathbf{F}}(\mathbf{X})]\} - \eta\,|\sigma| \tag{4.67}$$

Now, to satisfy Equation (4.65), assume that:

$$\eta = \|\mathbf{S}\|\,\left\|\mathbf{F}(\mathbf{X}) - \hat{\mathbf{F}}(\mathbf{X})\right\| + \eta_0 \tag{4.68}$$

where $\|.\|$ indicates the Euclidean norm for each vector. Therefore:

$$\sigma\dot{\sigma} \leq \sigma\{\mathbf{S}^T[\mathbf{F}(\mathbf{X}) - \hat{\mathbf{F}}(\mathbf{X})]\} - (\,\|\mathbf{S}\|\,\left\|\mathbf{F}(\mathbf{X}) - \hat{\mathbf{F}}(\mathbf{X})\right\| + \eta_0)\,|\sigma| \tag{4.69}$$

or

$$\sigma\dot{\sigma} \leq \sigma\{\mathbf{S}^T[\mathbf{F}(\mathbf{X}) - \hat{\mathbf{F}}(\mathbf{X})]\} - \|\mathbf{S}\|\,\left\|\mathbf{F}(\mathbf{X}) - \hat{\mathbf{F}}(\mathbf{X})\right\|\,|\sigma| - \eta_0\,|\sigma| \tag{4.70}$$

Thus:

$$\sigma\dot{\sigma} \leq \left|\sigma\{\mathbf{S}^T[\mathbf{F}(\mathbf{X}) - \hat{\mathbf{F}}(\mathbf{X})]\}\right| - \|\mathbf{S}\|\,\left\|\mathbf{F}(\mathbf{X}) - \hat{\mathbf{F}}(\mathbf{X})\right\|\,|\sigma| - \eta_0\,|\sigma| \tag{4.71}$$

That implies Equation (4.65), regarding the following equation:

$$\left| \sigma\{\mathbf{S}^T[\mathbf{F}(\mathbf{X}) - \hat{\mathbf{F}}(\mathbf{X})]\} \right| \leq \|\mathbf{S}\| \left\| \mathbf{F}(\mathbf{X}) - \hat{\mathbf{F}}(\mathbf{X}) \right\| |\sigma| \tag{4.72}$$

By finding $\eta(t)$ based on Equation (4.68), U can be found by:

$$U = -\mathbf{K}^T\mathbf{X} + (\mathbf{S}^T\mathbf{B})^{-1}[-\mathbf{S}^T\hat{\mathbf{F}}(\mathbf{X}) - \eta sign(\sigma)] \tag{4.73}$$

In practice, the discontinuity in the control law by the function $sign(\sigma)$ may result in the chattering. Both a reduction of chattering and low-pass noise filtering can be achieved if a continuous function in a thin boundary layer, instead of the sign function, is considered:

$$U = -\mathbf{K}^T\mathbf{X} + (\mathbf{S}^T\mathbf{B})^{-1}[-\mathbf{S}^T\hat{\mathbf{F}}(\mathbf{X}) - \eta\tanh(\frac{\sigma}{\Phi})] \tag{4.74}$$

where Φ is the boundary layer thickness.

Note that the resulting control only assures the global bounded stability instead of the global asymptotic stability for the reaching condition. This is the case for the states of the system as well. Moreover, if the elimination of the chattering for all situations is required, the thickness of the boundary layer must be large enough; however, this may significantly deteriorate robustness and accuracy. To solve these problems, a boundary layer with varying thickness must be considered [73, 74]. The thickness can be changed based on a function of the norm of the states that shows the distance between the state trajectory and the origin. This function can be constructed by using the tuned fixed boundary layers for two different operating points, as shown later.

Variable Structure Control for Baseline Vehicle

The dynamic system of the baseline vehicle can be described as a combination of a nominal linear system and the parameter uncertainties:

$$\dot{\mathbf{X}} = \mathbf{A}_n\mathbf{X} + \mathbf{B}U + \mathbf{F}(t) \tag{4.75}$$

where $\mathbf{A}_n$ corresponds to a condition that the uncertain parameters take their average values. Regarding Equation (4.43), $\mathbf{A}_n$ can be described by the following equation:

$$\mathbf{A}_n = \mathbf{A}_0 + \mathbf{A}_1 \bar{C}_{\alpha f} + \mathbf{A}_2 \bar{C}_{\alpha r} + \mathbf{A}_3 \bar{C}_{Tf} + \mathbf{A}_4 \bar{C}_{Tr} \tag{4.76}$$

In this equation $\bar{C}_{\alpha f}$, $\bar{C}_{\alpha r}$, $\bar{C}_{Tf}$ and $\bar{C}_{Tr}$ are the average values of the uncertain parameters, which can be easily specified based on the maximum and minimum of these parameters. In addition, $\mathbf{F}(t)$ can be represented in terms of the change in these parameters:

$$\mathbf{F}(t) = \mathbf{\Delta A}(t)\mathbf{X}(t) \tag{4.77}$$

where:

$$\mathbf{\Delta A}(t) = \mathbf{A}_1 \Delta C_{\alpha f}(t) + \mathbf{A}_2 \Delta C_{\alpha r}(t) + \mathbf{A}_3 \Delta C_{Tf}(t) + \mathbf{A}_4 \Delta C_{Tr}(t) \tag{4.78}$$

In addition, $\Delta C_{\alpha f}(t)$, $\Delta C_{\alpha r}(t)$, $\Delta C_{Tf}(t)$ and $\Delta C_{Tr}(t)$ show the difference between the real values and the average values of the uncertain parameters. For the case $C_{\alpha f}(t)$, $C_{\alpha r}(t)$, $C_{Tf}(t)$ and $C_{Tr}(t)$ take their average values, the uncertainties are zero ($\hat{\mathbf{F}}(t) = \mathbf{0}$), therefore for any other case:

$$\left\| \mathbf{F}(\mathbf{X}) - \hat{\mathbf{F}}(\mathbf{X}) \right\| \le \|\mathbf{\Delta A}(t)\| \, \|\mathbf{X}(t)\| \tag{4.79}$$

where the norm on $\mathbf{\Delta A}(t)$ can be found by using the vehicle parameters, as follows:

$$\|\mathbf{\Delta A}(t)\| \le \|\mathbf{A}_1\| \left| \Delta \bar{C}_{\alpha f} \right| + \|\mathbf{A}_2\| \left| \Delta \bar{C}_{\alpha r} \right| + \|\mathbf{A}_3\| \left| \Delta \bar{C}_{Tf} \right| + \|\mathbf{A}_4\| \left| \Delta \bar{C}_{Tr} \right| \tag{4.80}$$

By using Equation (4.44) to Equation (4.47), $\Delta \bar{C}_{\alpha f}$, $\Delta \bar{C}_{\alpha r}$, $\Delta \bar{C}_{Tf}$ and $\Delta \bar{C}_{Tr}$ are computed (the half difference between the maximum and minimum of their values). The forward speed of the vehicle is set to its maximum value ($u = 60$ km/h or 16.7 m/s) and the torsional stiffness and damping are set at their minimum values ($K_R = 1 \times 10^5$ Nm/rad, $C_R = 0$). Also, the other parameters of the vehicle are the same as in previous cases. For these values, according to Equation (4.80):

$$\|\mathbf{\Delta A}(t)\| \le 58.36 \tag{4.81}$$

Equations (4.79) and (4.80) can also be used to find the switching gain $\eta(t)$ based on Equation (4.68) if $\mathbf{S}$ is also specified. To do this, the closed loop poles on the sliding surface are chosen

141

$\lambda_1 = -12$, $\lambda_2 = -8$, $\lambda_3 = -6$, $\lambda_{4,5} = -2.1 \pm 5.6i$, and the sixth eigenvalue is $\lambda_6 = 0$. As shown later, these choices of the eigenvalues result in an acceptable performance. By using the pole placement method, based on the above eigenvalues, the state feedback vector $\mathbf{K}$ can be calculated by MATLAB, as follows:

$$\mathbf{K}^T = 2 \times 10^5 [-0.0163 \ 1.4950 \ 0.3695 \ -0.0330 \ 0.6859 \ -0.1658] \tag{4.82}$$

Then, based on Equation (4.55), $\mathbf{A}_C$ can be found, and $\mathbf{S}$ is a normalized eigenvector of $\mathbf{A}_C^T$ corresponding to $\lambda_6 = 0$:

$$\mathbf{S}^T = [0.0105 \ -0.8976 \ -0.0888 \ 0.1409 \ -0.4028 \ 0.0658] \tag{4.83}$$

Finally, based on Equation (4.68), η is tuned based on the following to overcome the uncertainties:

$$\eta > 58.36 \, \|\mathbf{X}\| \tag{4.84}$$

A higher η can provide robustness against unmodeled disturbance or nonlinearity as well. The varying boundary layer Φ is related to the norm of the states based on the following equation, which results in a good trade-off between the robustness and chattering elimination:

$$0.05 < \|\mathbf{X}\| < 1.3 : \Phi = \|\mathbf{X}\| \, ; \|\mathbf{X}\| > 1.3 : \Phi = 1.3; \|\mathbf{X}\| < 0.05 : \Phi = 0.05 \tag{4.85}$$

Therefore, based on Equation (4.74), the control law is determined that in fact specifies the differential braking torque ΔT.

4.5.3   Evaluation of Controller Performance

By using the devised controller, stability can be achieved in different driving conditions. As shown previously (see Figure 4-13), the articulation angle will change according to an undamped oscillatory mode in response to a small perturbation in the articulation angle for $u = 12.5$ m/s. If the resulting differential braking system is activated after 9.7 seconds of this motion, the instability will be eliminated, as shown in Figure 4-27. As shown in Figure 4-16, for $u = 60$ km/h (16.7 m/s), the disturbed motion of the vehicle is again an undamped oscillatory mode. If

142

the resulting stability control system is activated after ten seconds of this motion, the instability will be prevented, as shown in Figure 4-28. For the motion with a long rear-mounted attachment at $u = 60$ km/h, a promoted instability occurs, as shown in Figure 4-19. If the developed system is activated after five seconds of this motion, the instability is removed, as shown in Figure 4-29. The required differential braking torque is also shown in Figure 4-30 for this case. The dynamic behavior after the controller operation is similar to that resulting from the activation of the torque vectoring device (see Figure 4-20). However, the required torque is about two times that as in the case of the torque vectoring device (see Figure 4-21). This is due to the fact that two rear wheels of the vehicle were used for that device. Moreover, the maximum longitudinal tire force resulting from the braking torque shown in Figure 4-30 is less than 10000 N, which is much smaller than the maximum tire force that can be produced on the highway surface (about 30000 N). Therefore, the required longitudinal tire force to stabilize the baseline vehicle in its most critical condition can be easily provided. Also, regarding the large mass of the vehicle (about 14500 kg), the decrease in the forward speed of the vehicle during the stabilization will be about 1.5 m/s. Therefore, even in the most critical condition for the stabilization of the vehicle, the change in the forward speed is not considerable.

The performance of the stability controller is also evaluated when the vehicle is traveling on another surface, such as a road covered with gravel. For this surface, the response is simulated at $u = 60$ km/h, as shown in Figure 4-31. The tire parameters for this surface are computed based on the Metz tire model. The response is an unstable snaking mode. Comparing Figures 4-16 and 4-31 shows that the snaking oscillations are stronger when the vehicle is traveling on highway surface. This is due to the higher lateral tire force produced at the wheels. If the resulting control system is activated after ten seconds of this motion, the instability is eliminated, as shown in Figure 4-32.

4.5.4   Simulation in ADAMS

To verify the results from analyzing the modified 7-DOF model, the motion of the virtual prototype of the baseline vehicle is simulated in ADAMS by incorporating the stability controller system to remove the instability. As shown in Figure 4-23, the response of the virtual prototype at $u = 12.5$ m/s, following a small perturbation, is the unstable snaking oscillations. If the
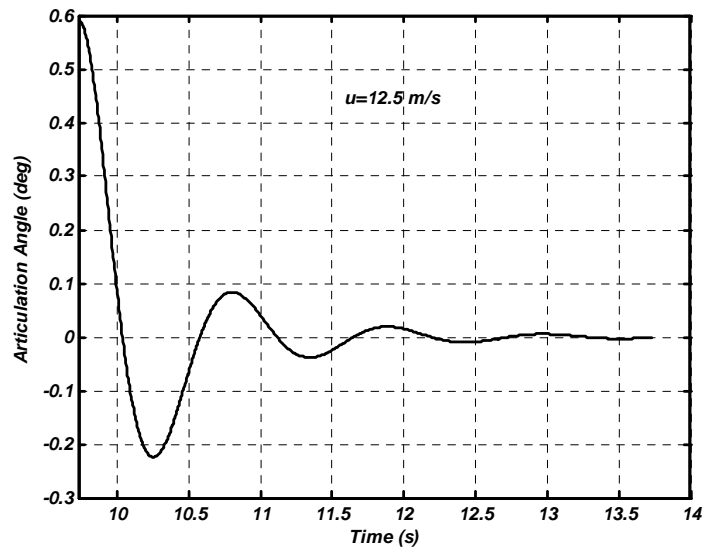
Figure 4-27: Stabilization of baseline vehicle at $u = 12.5$ m/s by differential braking.
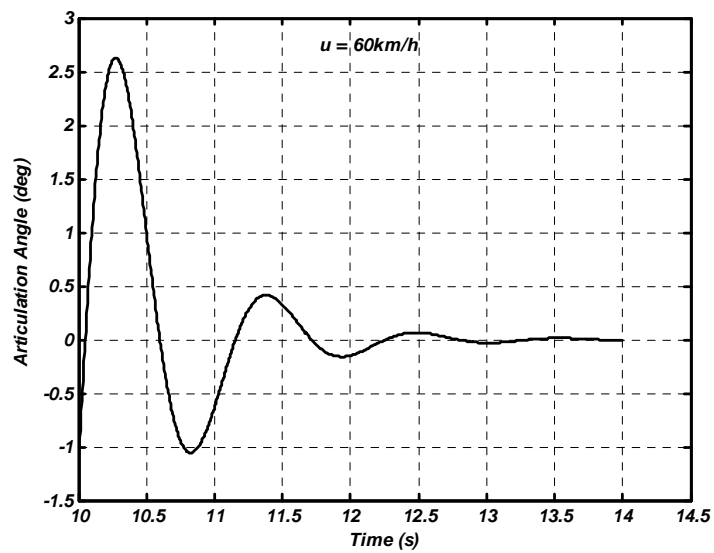
Figure 4-28: Stabilization of baseline vehicle at $u = 60$ km/h by differential braking.
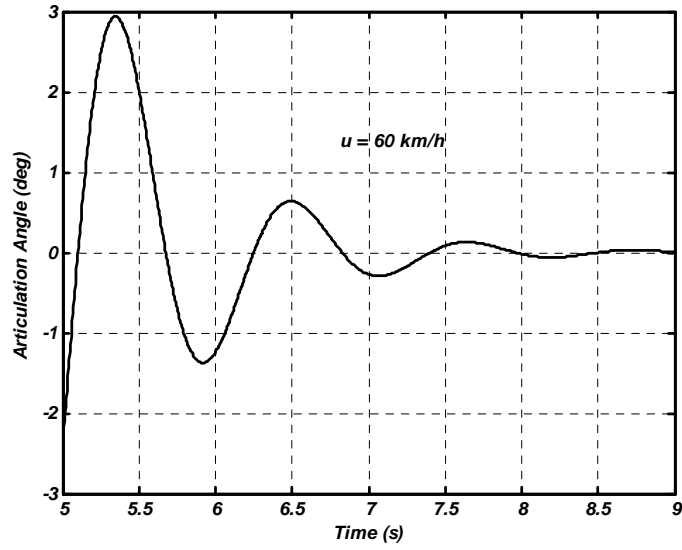
Figure 4-29: Stabilization of baseline vehicle with rear-mounted attachment by differential braking.
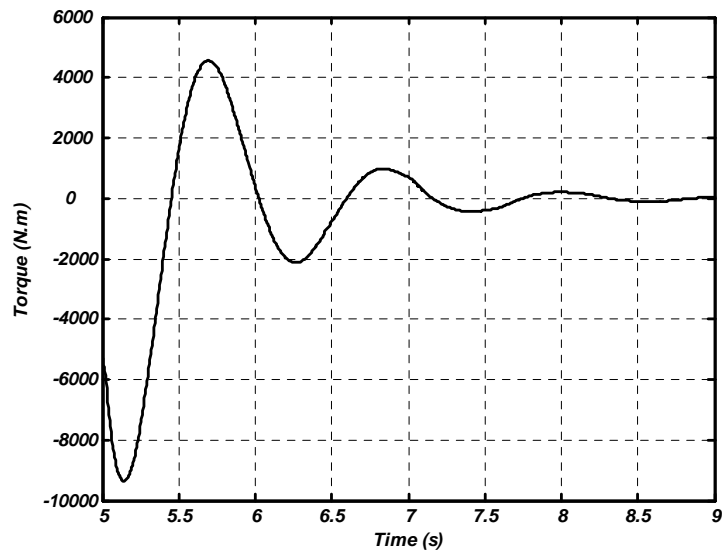
Figure 4-30: Differential braking torque for stabilization of baseline vehicle with rear-mounted attachment.

145
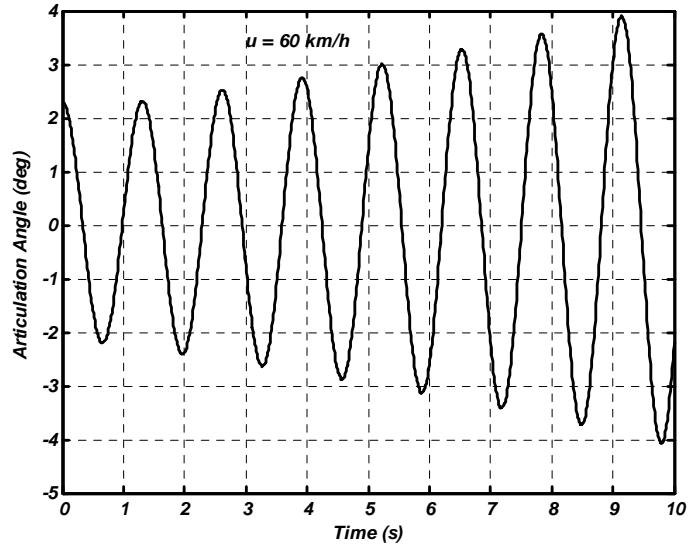
Figure 4-31: Instability of baseline vehicle at $u = 60$ km/h on gravel surface.
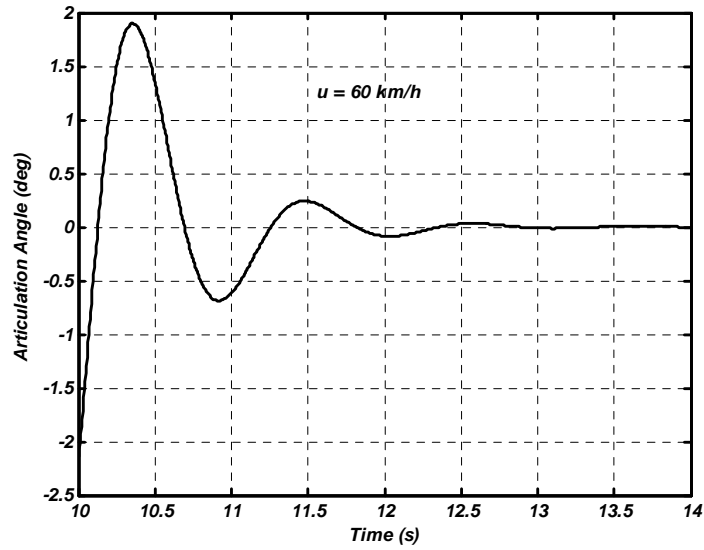

Figure 4-32: Stabilization of baseline vehicle on gravel surface by differential braking.

146
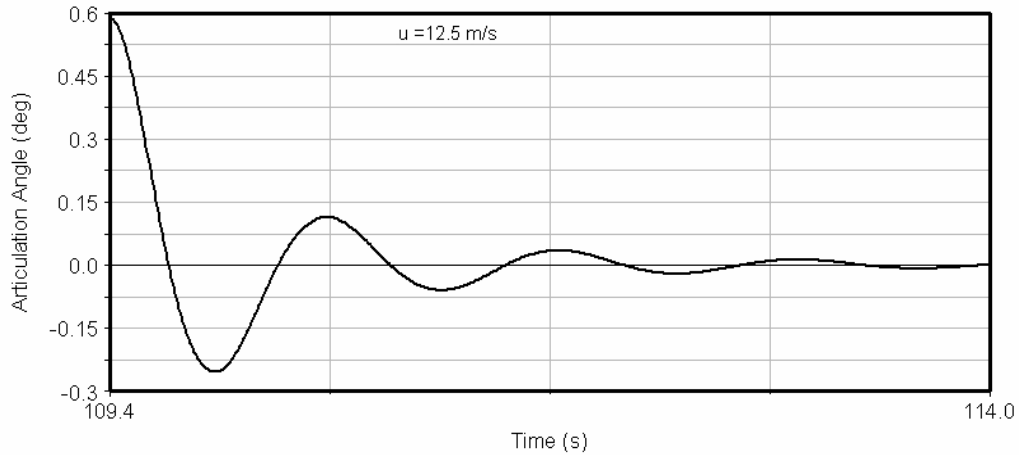
Figure 4-33: Stabilizing of baseline vehicle with differential braking in ADAMS.

stability controller is activated, the response will be as shown in Figure 4-33. For the modified 7-DOF model, the response of the vehicle after the control system activation at $u =$12.5 m/s was shown in Figure 4-27. Comparing Figures 4-33 and 4-27 indicates that the resulting dynamic behavior after starting the stabilization is similar for the both modified 7-DOF and virtual prototype. The braking torques applied to the left and right wheels of the rear axle are shown in Figure 4-34. Regarding the large mass of the vehicle, the change in the forward speed due to these braking torques is not considerable.

4.6   Summary

To indicate the shortcomings of passive methods to stabilize a conventional ASV, which are mainly based on changes in the steering system, a combined model of the vehicle with a hydraulic-mechanical steering system was developed based on a 3-DOF model. To do this, the pressure-flow equation of the steering system was added to the equations of motion for the 3-DOF model. The analysis of the resulting equations showed that the instability of a conventional ASV during the snaking mode can be alleviated by increasing friction at the articulation joint or introducing leakage flow across the cylinders. Although these methods can be used to alleviate the problem, they are not always practical and reliable methods for this purpose.

147
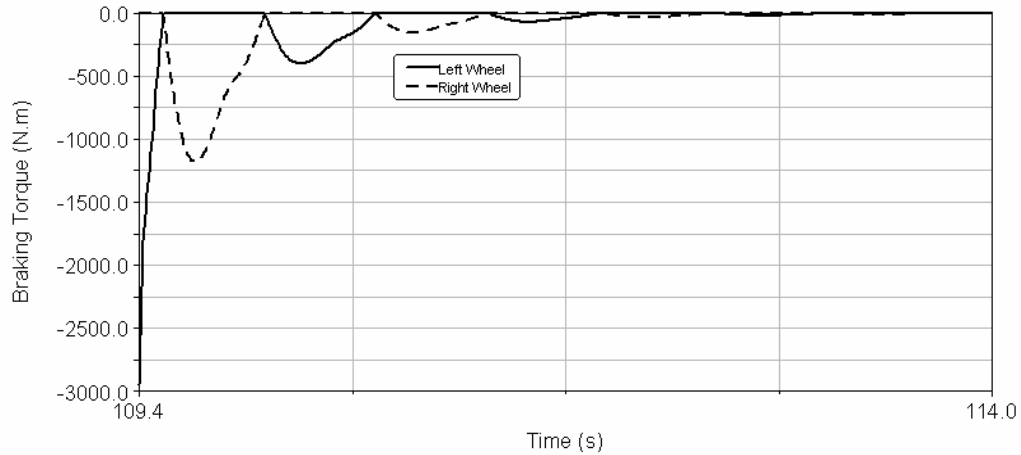
Figure 4-34: Braking torques at left and right rear wheels from ADAMS.

In addition, they result in loss of power and greater nonlinearity of the system. Therefore, other alternatives, including different types of stability control systems, were suggested. With regard to advantages of using longitudinal tire force at the rear wheels for the stabilization of the vehicle, the studies in this chapter were mostly concentrated on the use of torque vectoring and differential braking strategies.

First, an active steering system was proposed to remove the instability. This system not only prevented the instability, but also improved the steering response of the vehicle. For this system, a classical controller including PID element and notch filter was tuned for the on-highway travel of the baseline vehicle at a forward speed of 12 m/s. Although the performance of the resulting system was satisfactory and mainly insensitive to the parameter variations, it was highly conservative, owing to the high value of the required flow for the stabilization. Therefore, considering the many unknown factors affecting vehicle dynamics, owing to its operation with different attachments and on unpredictable and time-varying terrains, the design of robust controllers for the stabilization of the baseline vehicle was considered.

For doing this, an active torque vectoring device was investigated to remove the instability despite any uncertainty. This system can be used to remove the instability, and at the same time to improve the traction capabilities of a conventional ASV. For this device, a robust full state feedback controller was developed. The stabilization was done by controlling two equal

148

but opposite torques at the left and right rear wheels of the vehicle. Two longitudinal tire forces were generated by applying these opposite torques to the wheels of the rear axle through a torque vectoring device. To design the controller, first, the 3-DOF model was modified to include wheel rotational dynamics, resulting in a 7-DOF model. This model was examined to analyze the effects of uncertainty in the various tire parameters. The effective cornering stiffness and aligning stiffness for the rear and front axles were identified as the most important uncertain parameters for the stability during the snaking mode. Next, by using the resulting 7-DOF model, the equations of motion were represented in the form of a polytopic system, which depends affinely on the four above-mentioned uncertain parameters. Finally, some Linear Matrix Inequalities (LMIs) were solved using MATLAB to find both the Lyapunov and state feedback matrices for the robust stabilization of the resulting polytopic system of the vehicle. The simulations showed that the vehicle can be stabilized, and the snaking oscillations can be effectively prevented even if the vehicle is equipped with a long rear-mounted attachment. The stability control system was incorporated into the virtual prototype of the vehicle in ADAMS, and the motion was simulated. The results based on the analysis of 7-DOF model were reasonably consistent with those from the simulation in ADAMS.

As another solution, a stability control system based on differential braking to remove the instability of the baseline vehicle was developed. For this system, a robust variable structure control system was designed. The input matrix for the 7-DOF model was changed according to differential braking strategy. By using the equations of motion, the uncertainties of the parameters related to tire-road contact were introduced as some unknown and time-varying terms. These terms were considered as a norm-bounded disturbance vector based on the range of the uncertainties. Based on this description, the robust control system was designed to stabilize the vehicle during the snaking mode. The robustness of the resulting system was investigated for traveling on different surfaces, and for different driving conditions in terms of the forward speed and vehicle parameters, based on the modified 7-DOF model. The control system was also connected to the virtual prototype of the vehicle in ADAMS, and its operation was investigated. In general, the results from the modified 7-DOF model analysis and simulation in ADAMS were reasonably compatible. These results showed that the vehicle can be stabilized in different driving conditions and in traveling on different surfaces.

Chapter 5

Conclusions and Future Work

This study was undertaken to address the lack of research on effective stabilization of conventional ASVs at higher speeds by designing several stability control systems for a typical ASV, specifically, a forestry skidder. These systems were developed to stabilize the snaking oscillations by using various strategies, including active steering, torque vectoring and differential braking. These developments were based on a comprehensive study of the causes of the instability and the effects of the vehicle parameters and its operating conditions on the stability. In this chapter, a summary of the achievements is presented and some topics are introduced that can be considered as potential future studies in this area.

5.1   Dissertation Summary

First, to identify the causes of instability during the snaking mode for a conventional ASV (i.e. a forestry skidder) various analyses were presented. These analyses were mostly concentrated on examining the effects of forward speed and of two main subsystems of the vehicle, steering system and tire, which were determining factors on the stability. With regard to the importance of the tire and steering system, the modeling aspects of these systems were detailed. Several tire models, such as linear, off-road mobility number-based, Fiala and Metz model, were introduced. Typical steering systems of ASVs, including hydrostatic and hydraulic-mechanical, were also described. In view of the pressure-flow equation for these steering systems, a torsional spring and damper at the articulation joint were utilized to model the steering system characteristics.

Two simplified models of the vehicle, including a 1-DOF model and a 3-DOF model, were devised using models of the vehicle subsystems. The simplified models of the vehicle were used for the stability analysis of straight-line travel with different forward speeds. To do this, the roots (eigenvalues) of the characteristic equation of the system were used. Although the analysis of the 1-DOF model showed no instability, it implied that increasing the forward speed leads to an oscillatory yaw motion with lower damping ratio. The results of the 3-DOF model analysis were consistent with given results for an articulated steer tractor reported in [3]. An analysis was then conducted based on the 3-DOF model for the baseline vehicle, which indicated an unstable snaking mode for forward speeds higher than the so-called critical forward speed. Therefore, higher speeds significantly affect the lateral stability of conventional ASVs. The effects of torsional spring stiffness and damping at the articulation joint on the snaking were also examined. The investigations showed that an increase in torsional stiffness or torsional damping can alleviate the snaking oscillations. This means that the design of the articulated frame steering system that controls the articulation angle is more critical than the design of the steering system for front wheel steer vehicles. This is due to the fact that the steering system of an ASV has two different functions: ensuring both maneuverability and lateral stability, considering the instability of an ASV occurs only when the torsional spring and stiffness, which result from the steering system characteristics, are at low levels.

To verify the results predicted by the 3-DOF model, the motion of a virtual prototype of the vehicle in ADAMS was simulated for different conditions. The comparisons showed that the results from the simulations and the stability analyses using the 3-DOF model were reasonably consistent. In other words, the conducted analyses showed that the 3-DOF model can be used to obtain considerable insight into basic aspects of the lateral stability of a conventional ASV during the snaking mode for different conditions. Also, the effect of tire rolling resistance on stability was investigated using the virtual prototype. This effect was equivalent to increasing the torsional damping at the articulation joint. Moreover, the simulations by the virtual prototype showed that the interaction of the resultant lateral force at the front and rear dominated the response of the vehicle during the snaking mode. When the cornering stiffness of the tires at the front or rear changed, the response of the vehicle was affected. The results showed that when the cornering stiffness of the rear tires decreased, the snaking oscillations were also

alleviated. The effects of vehicle parameters and operating conditions on stability were also examined. These studies were mostly based on the minimum torsional stiffness required to stabilize the vehicle up to 20 m/s (i.e. critical torsional stiffness). The investigations suggested that the straight-line on-highway motion with constant forward speed was the most critical driving condition. The change in the mass and moment of inertia affected the critical torsional stiffness to some degree. The effects of the center of mass positions were so significant that they could change the order of magnitude of the critical torsional stiffness, although the front part center of mass position has less effect compared with that for the rear part. When the rear part center of mass was located well-rearward or the front part center of mass was located well-forward, the vehicle showed an unstable snaking mode. The instability for the well-forward front part center of mass happens at considerably high speeds (i.e. 60 km/h or higher).

Moreover, to identify the effects of locking differentials on the stability, the 3-DOF model was extended to a 5-DOF model, including two more degrees of freedom for the rotation of the front and rear tires. Based on the results, a significant reduction in the critical torsional stiffness can be achieved by locking both differentials. This powerful effect resulting from locking both differentials is enough to prevent the instability in normal driving conditions during the snaking mode. Locking only one of the differentials can also be used to stabilize the vehicle, but to a lower degree. The important effects of locking the differentials were explained based on a theoretical analysis. The analysis implied that the effect is similar to introducing a kind of damping, similar to the torsional damping at the articulation joint for wasting the energy, according to Equation (3.21). A more equivalent damping was provided by locking both the differentials, and thus, the effect on the snaking oscillations was more significant. To verify the results from the 5-DOF model, the motion of the virtual prototype with front differential locked was simulated in ADAMS. The result showed that the simplifying assumptions used in developing the 5-DOF model have no important effects. Note that the virtual prototype of the vehicle in ADAMS is a three dimensional nonlinear model, but the 5-DOF model is planar and linear. In brief, the studies based on the 5-DOF model suggested that locking the differentials can be used for stabilizing the snaking oscillations, even on-the-go. This simple and effective method overcomes a problem that makes some difficulties for the drivers during travel on roads and highways. Based on several simplifying assumptions, the 3-DOF model was then extended

to a 4-DOF model to analyze the effects of a rear-mounted load having interaction with the ground on stability. These assumptions include application of the tractive force only at the front wheels instead of the four wheels, and application of a constant normal force at the tires and load-ground contact area. A stability analysis based on the eigenvalues of the system showed that when the vehicle was carrying a rear-mounted load, unstable snaking oscillations occurred if the vehicle was moving on a relatively good off-road surface. Increasing the torsional stiffness or damping at the articulation joint resulted in a decrease in the snaking oscillations. The same result can be achieved by an increase in the torsional damping at the grapple joint. To verify the results from the above stability analysis, the motion of the virtual prototype was simulated for different conditions by linking the mobility number-based off-road tire model to the ADAMS solver. In general, the simulation results were consistent with the results from the stability analysis. In brief, the investigations on the stability of the vehicle with rear-mounted load indicated the important effects of the torsional damping at the grapple joint, in addition to the torsional stiffness and damping at the articulation joint.

To show the shortcomings of passive methods to stabilize the vehicle during the snaking mode, which are mostly based on some changes in the steering system, the 3-DOF model was changed to a combined model including both a model of the vehicle and its steering system. For the combined model, both the equations of motion of the 3-DOF model and the pressure-flow equation of the steering system were present. The combined model was analyzed to identify the relieving effects of increasing friction at the articulation joint or introducing leakage flow across the cylinders. The analyses showed that these passive methods may alleviate the snaking oscillations to some degree; however, they may not be suitable for all cases and lead to loss of power (described by Equation (3.20) for any equivalent torsional damping) and greater nonlinearity of the system. As a result, the investigations suggested using alternative solutions to stabilize the vehicle. Therefore, applications of different types of stability control systems were reviewed, with more focus on using longitudinal tire force for the stabilization. The use of an active steering system was initially studied as a stabilizing device. An extra feature of this system is an improvement in the steering response of the vehicle. A classical controller based on a PID element and a notch filter was tuned for a specific driving condition of the vehicle, on-highway travel with a forward speed of 12 m/s. Although the performance of the

controller was satisfactory for some conditions, the performance may not be suitable for the other situations due to the unknown factors that change the stability behavior during different operations. To prevent the instability, another alternative, the use of an active torque vectoring device, was also studied. The device was able to produce and control the values of two equal but opposite torques at the left and right rear wheels. Owing to the resulting opposite but similar longitudinal tire forces, the forward speed of the vehicle remains constant. An extra feature of this system is an improvement in the traction capabilities of the vehicle, in addition to removing the instability. To accommodate the uncertainties, this device was equipped with a robust full-state feedback controller. To include the effect of wheel rotational dynamics due to applying a torque, the 3-DOF model was extended to a 7-DOF model, with the rotation angles of the four wheels as four extra degrees of freedom. By using this model, the effects of uncertainty in the different tire parameters were studied to identify the most important uncertain parameters for the stability during the snaking mode. Based on the results, the front and rear effective cornering stiffness and aligning stiffness were determined to be the most significant uncertain parameters. Then, the 7-DOF model was used to represent the equations of motion in the form of a polytopic system that depends affinely on the most significant uncertain parameters. For the resulting polytopic system, several Linear Matrix Inequalities (LMIs) were developed and solved by MATLAB to detect the Lyapunov and state feedback matrices for the robust stabilization. Some simulations were conducted based on the 7-DOF model to reveal that the vehicle can be effectively stabilized during the snaking mode even if the vehicle was equipped with a long rear-mounted attachment. The stability control system was also connected to the virtual prototype of the vehicle and the motion was simulated. The results from the simulations based on both the 7-DOF model and the virtual prototype were reasonably compatible.

As another solution to prevent the instability, a stability control system based on differential braking was designed. Differential braking is a simple strategy, compared to torque vectoring, for stability control. By applying braking torque to a single wheel for producing the longitudinal tire force, the forward speed of the baseline vehicle was partially reduced. Compared with the torque vectoring strategy, more tire wear is introduced due to the large braking force produced at the wheels. For differential braking strategy, a robust variable structure controller was designed to accommodate the uncertainties. For this system, the input matrix of the 7-DOF

model was different from that for the torque vectoring device. The equations of motion for the 7-DOF model were written in a form such that the uncertainties of the above-mentioned parameters related to tire-road contact were introduced as some unknown and time-varying terms. Then, the bound on the norm of uncertain terms were found by using the range of the uncertainties. This allowed for the design of a robust variable structure control system to stabilize the vehicle during the snaking mode. The 7-DOF model was used to examine the robustness of the resulting stability controller for different conditions in terms of forward speed and vehicle parameters. Again, the control system was incorporated into the virtual prototype and the performance was evaluated. In general, the results implied that the developed system can effectively stabilize the vehicle in different driving conditions and when traveling on different surfaces.

5.2   Future Work

As mentioned previously, for load-carrying ASVs with an articulation joint in the front, the most common form of the lateral instability is jackknifing. Similar to the snaking instability, jackknifing is also promoted when the forward speed increases. In view of increasing forward speeds for ASVs, this instability should be addressed to increase on-highway safety during the travel of ASVs. Although some limited studies have been conducted to analyze this undesirable motion by the author [39, 75], a comprehensive examination is still required to investigate the effects of vehicle parameters and operating conditions. These investigations might be used to develop active safety devices that are capable of preventing or alleviating the instability.

Also, there is a new trend towards providing various suspension systems for ASVs to improve comfort. Obviously, the use of a suspension system introduces some changes in the dynamics of the vehicle, which affects both the roll and lateral stability of the vehicle. The resulting effects on the stability should be analyzed to identify any possible problem.

Bibliography

[1] D. A. Crolla, "An analysis of off-road vehicle steering behaviour," in *Proceedings of the 7th ISTVS Conference, Calgary*, pp. 1265–1290. 1981.

[2] I. C. Holm, "Articulated, wheeled off-the-road vehicles," *Journal of Terramechanics*, vol. 7, no. 1, pp. 19–54, 1970.

[3] D. A. Crolla and D. N. L. Horton, "The steering behaviour of articulated body steer vehicles," in *Paper C123/83. I. Mech. E. Conference on Road Vehicle Handling, MIRA, Nuneaton*. 1983.

[4] H. G. Gibson, K. C. Elliott, and S. P. E. Persson, "Side slope stability of articulated-frame logging tractors," *Journal of Terramechanics*, vol. 8, no. 2, pp. 65–79, 1971.

[5] P. A. Dudzinski, "Design characteristics of steering systems for mobile wheeled earthmoving equipment," *Journal of Terramechanics*, vol. 26, no. 1, pp. 25–82, 1989.

[6] H. G. Gibson and C. J. Biller, "Side-slope stability of logging tractors and forwarders," *Transactions of the ASAE*, vol. 17, no. 2, pp. 245–250, 1974.

[7] H. G. Gibson, B. C. Thorner, and J. W. Thomas, "Slope stability warning device for articulated tractors," *United States Patent 4284987*, 1981.

[8] G. Wray, J. Nazalewicz, and A. J. Kwitowski, "Stability indicators for front end loaders," in *Proceedings of the 8th International Conference ISTVS, Cambridge*, pp. 655–671. 1984.

[9] H. J. Cornett, "Steering of large articulated vehicles," *SAE Paper 831383*, 1983.

[10] D. N. L. Horton and D. A. Crolla, "Theoretical analysis of the steering behaviour of articulated frame steer vehicles," *Vehicle System Dynamics*, vol. 15, pp. 211–234, 1986.

[11] D. A. Crolla and D. N. L. Horton, "Factors affecting the dynamic behaviour of higher speed agricultural vehicles," *J. Agric. Engng Res.*, vol. 30, pp. 277–288, 1984.

[12] R. T. Bundorf, "Directional control dynamics of automobile-travel trailer combinations," *SAE Paper 670099*, 1967.

[13] R. S. Sharp and M. A. Alonso Fernandez, "Car-caravan snaking part 1: The influence of pintle pin friction," in *Proceedings of the Institution of Mechanical Engineers, Part C: Journal of Mechanical Engineering Science, V216, n7*, pp. 707–722. 1999.

[14] M. A. Alonso Fernandez and R. S. Sharp, "Caravan active braking system-effective stabilisation of snaking of combination vehicles," *SAE Paper 2001-01-3188*, 2002.

[15] R. S. Sharp and M. A. Alonso Fernandez, "Car-caravan snaking part 2: Active caravan braking," in *Proceedings of the Institution of Mechanical Engineers, Part C: Journal of Mechanical Engineering Science, V216, n7*, pp. 723–736. 2002.

[16] Y. He, A. Khajepour, J. McPhee, and X. Wang, "Dynamic modeling and stability analysis of articulated frame steer vehicles," *International Journal of Heavy Vehicle Systems*, vol. 12, no. 1, pp. 28–59, 2005.

[17] D. A. Crolla and A. S. A. El-razaz, "A review of the combined lateral force generation of tires on deformable surfaces," *Journal of Terramechanics*, vol. 24, no. 3, pp. 199–225, 1987.

[18] C. S. Liu, V. Monkaba, H. Tan, C. McKenzie, H. Lee, and S. Suo, "Driveline torque-bias-management modeling for vehicle stability control," *SAE Paper 2002-01-1584*, 2002.

[19] N. L. Azad, J. McPhee, and A. Khajepour, "The effects of front and rear tires characteristics on the snaking behavior of articulated steer vehicles," in *Proceedings of IEEE Vehicle Power and Propulsion (VPP) Conference, Chicago, Illinois, USA*, pp. 221–226. 2005.

[20] N. L. Azad, J. McPhee, and A. Khajepour, "Tire forces and moments and on-road lateral stability of articulated steer vehicles," *SAE Paper 2005-01-3597*, 2005.

[21] H. B. Pacejka, *Tire and Vehicle Dynamics, Second Edition*, Society of Automotive Engineers Inc., 2006.

[22] R. W. Allen and T. J. Rosenthal, "A vehicle dynamics tire model for both pavement and off-road conditions," *SAE Paper 970559*, 1997.

[23] J. Y. Wong, *Theory of Ground Vehicles, Second Edition*, John Wiley and Sons Inc., 1993.

[24] M. I. Lyasko, "The determination of deflection and contact characteristics of a pneumatic tire on a rigid surface," *Journal of Terramechanics*, vol. 31, no. 4, pp. 239–246, 1994.

[25] D. Gee-Clough and M. S. Sommer, "Steering forces on undriven, angled wheels," *Journal of Terramechanics*, vol. 18, no. 1, pp. 25–49, 1981.

[26] D. Gee-Clough, "Selection of tyre sizes for agricultural vehicles," *J. agric Engng Res.*, vol. 25, pp. 261–278, 1980.

[27] K. A. Abd El-Gawwad, D. A. Crolla, A. M. A. Soliman, and F. M. El-Sayed, "Prediction of the performance of off-road tyres," *Heavy Vehicle Systems, International Journal Vehicle Design*, vol. 5, no. 3/4, pp. 359–378, 1998.

[28] L. D. Metz, "Dynamics of four-wheel-steer off-highway vehicles," *SAE Paper 930765*, 1993.

[29] L. L. Charlson, "Controller for fluid pressure operated devices," *United States Patent Re25126*, 1962.

[30] M. Martyna, "Mathematical model of the articulated loader steering system," in *Modelling, Simulation and Control, B, ASME Press, Vol. 18, No.3*, pp. 51–64. 1988.

[31] H. E. Merritt, *Hydraulic Control Systems*, John Wiley and Sons Inc., 1967.

[32] Y. He, N. L. Azad, C. Urbaniak, A. Khajepour, and J. McPhee, "Lateral stability analysis and parameter estimation of articulated frame steer vehicles," in *Proceedings of CSME 2004, London, Ontario, Canada*, pp. 962–971. 2004.

[33] R. D. Scholl and R. E. Klein, "Stability analysis of an articulated vehicle steering system," *SAE Paper 710527*, 1971.

[34] R. Bell and A. de Pennington, "Active compensation of lightly damped electrohydraulic cylinder drives using derivative signals," in *Proc Instn Mech Engrs, Vol 184, Pt 1, No 4*, pp. 83–98. 1969-70.

[35] R. B. Rummer, "Designing forest machines for better ride with computer simulation," *SAE Paper 881306*, 1988.

[36] MSC. Software Corporation, *Using ADAMS/Solver 2005r2 (FORTRAN): Using Tire Statement*, 2005.

[37] J. C. Dixson, *Tires, Suspension and Handling*, Society of Automotive Engineers Inc., 1996.

[38] N. L. Azad, A. Khajepour, and J. McPhee, "The effects of locking differentials on the snaking mode of articulated steer vehicles," *International Journal of Vehicle Systems Modelling and Testing*, 2006 (in press).

[39] N. L. Azad, A. Khajepour, and J. McPhee, "The effects of drive configuration on undesirable behaviors of articulated steer vehicles," in *Proceedings of IEEE Vehicle Power and Propulsion (VPP) Conference, Chicago, Illinois, USA*, pp. 211–215. 2005.

[40] N. L. Azad, A. Khajepour, and J. McPhee, "Off-road lateral stability analysis of an articulated steer vehicle with a rear-mounted load," *International Journal of Vehicle Systems Modelling and Testing*, vol. 1, no. 1,2,3, pp. 106–130, 2005.

[41] F. Momiyama, K. Hoshikawa, J. Katou, and T. Hosoda, "Tractive torque steer for on-center stability/handling augmentation with controlling differential gear for large-sized vehicles - a comparision with passive rear-axle steer," *SAE Paper 912688*, 1991.

[42] M. McAllister, "Forces on undriven, angled wheels," in *Proceedings of the 8th International Conference ISTVS, Cambridge*, pp. 803–820. 1984.

[43] W. Harter, W. Pfeiffer, P. Dominke, G. Ruck, and P. Blessing, "Future electrical steering systems: Realizations with safety requirements," *SAE Paper 2000-01-0822*, 2000.

[44] J. He, D. A. Crolla, M. C. Levesley, and W. J. Manning, "Integrated active steering and variable torque distribution control for improving vehicle handling and stability," *SAE Paper 2004-01-1071*, 2004.

[45] Y. Zeyada, D. Karnopp, and S. El-Behiry M. El-Araby, "A combined active-steering differential-braking yaw rate control strategy for emergency maneuvers," *SAE Paper 980230*, 1998.

[46] N. L. Azad, A. Khajepour, and J. McPhee, "An active control device based on differential braking for articulated steer vehicles," *SAE Paper 2006-01-3568*, 2006.

[47] N. L. Azad, J. McPhee, and A. Khajepour, "Robust variable structure control for stabilization of articulated steer vehicles by torque vectoring," *International Journal of Heavy Vehicle Systems*, 2006 (in press).

[48] N. L. Azad, A. Khajepour, and J. McPhee, "Stability control of articulated steer vehicles by passive and active steering systems," *SAE Paper 2005-01-3573*, 2005.

[49] N. L. Azad, A. Khajepour, and J. McPhee, "Robust state feedback stabilization of articulated steer vehicles," *Journal of Vehicle System Dynamics*, 2006 (in press).

[50] N. L. Azad, A. Khajepour, and J. McPhee, "Robust stabilization of articulated steer vehicles by differential braking," in *Proceedings of CSME Forum, Symposium on Intelligent Vehicles and Transportation Systems, Calgary, Alberta, Canada.* 2006.

[51] D. Wu, Q. Zhang, and J. F. Reid, "Adaptive steering controller using a kalman estimator for wheel-type agricultural tractors," *Robotica*, vol. 19, pp. 527–533, 2001.

[52] B. G. Poorman, "Electro-hydraulic steering system for an articulated vehicle," *United States Statutory Invention Registration H1,846*, 2000.

[53] M. Ohba, H. Suzuki, T. Yamamoto, and H. Takuno, "Development of a new electronically controlled 4wd system: Toyota active torque control 4wd," *SAE Paper 1999-01-0744*, 1999.

[54] J. Kinsey, "The advantages of an electronically controlled limited slip differential," *SAE Paper 2004-01-0861*, 2004.

[55] M. J. Hancock, R. A. Williams, T. J. Gordon, and M. C. Best, "A comparison of braking and differential control of road vehicle yaw-sideslip dynamics," *Proceedings of the I MECH E. Part D. Journal of Automobile Engineering*, vol. 219, no. 3, pp. 309–327, 2005.

160

[56] K. Yi, T. Chung, J. Kim, and S. Yi, "An investigation into differential braking strategies for vehicle stability control," *Proceedings of the Institution of Mechanical Engineers, Part D, Journal of Automobile Engineering*, vol. 217, pp. 1081–1094, 2003.

[57] B. C. Kuo, *Automatic Control Systems*, John Wiley and Sons Inc., 1995.

[58] S. Hui and S. H. Zak, "Robust control synthesis for uncertain/nonlinear dynamical systems," *Automatica*, vol. 28, no. 2, pp. 289–298, 1992.

[59] Jr. R. E. Benton and D. Smith, "A non-iterative lmi-based algorithm for robust static-output-feedback stabilization," *INT. J. CONTROL*, vol. 72, no. 14, pp. 1322–1330, 1999.

[60] P. L. D. Peres, J. C. Geromel, and J. Bernussou, "Quadratic stabilizabiltiy of linear uncertain systems in convex-bounded domains," *Automatica*, vol. 29, no. 2, pp. 491–493, 1993.

[61] J. J. Slotine and W. Li, *Applied Nonlinear Control*, Prentice-Hall, New Jersey, 1991.

[62] S. Boyd, L. El Ghaoui, E. Feron, and V. Balakrishnan, *Linear Matrix Inequalities in System and Control Theory*, ser. SIAM Studies in Applied Mathematics. Philadelphia, PA: SIAM, Vol.15, 1994.

[63] P. Gahinet, A. Nemirovski, A. J. Laub, and M. Chilali, *User's Guide of LMI Toolbox for user with MATLAB*, the MATHWORKS Inc., 1995.

[64] C. Edwards and S. K. Spurgeon, *Sliding Mode Control: theory and applications*, Taylor and Francis, London, 1998.

[65] B. Drazenovic, "The invariance condition in variable structure systems," *Automatica*, vol. 5, pp. 287–295, 1969.

[66] S. K. Spurgeon and R. Davies, "A nonlinear control strategy for robust sliding mode performance in the presence of unmatched uncertainty," *Automatica*, vol. 28, no. 2, pp. 289–298, 1993.

[67] L. K. Wong, F. H. F. Leung, and P. K. S. Tam, "A chattering elimination algorithm for sliding mode control of uncertain non-linear systems," *Mechatronics*, vol. 8, pp. 765–775, 1998.

[68] R. Cristi, F. A. Papoulias, and A. J. Healey, "Adaptive sliding mode control of autonomous underwater vehicles in the dive plane," *IEEE Journal of Oceanic Engineering*, vol. 15, no. 3, pp. 152–160, 1990.

[69] A. J. Healey and D. Lienard, "Multivariable sliding mode control for autonomous diving and steering of unmanned underwater vehicles," *IEEE Journal of Oceanic Engineering*, vol. 18, no. 3, pp. 327–339, 1993.

[70] R. K. Lea, R. Allen, and S. L. Merry, "A comparative study of control techniques for an underwater flight vehicle," *International Journal of Systems Science*, vol. 30, no. 9, pp. 947–964, 1999.

[71] C. M. Kwan, "Sliding mode control of linear systems with mismatched uncertainties," *Automatica*, vol. 31, no. 2, pp. 303–307, 1995.

[72] J. J. E. Slotine and J. A. Coetsee, "Adaptive sliding controller synthesis for non-linear systems," *INT. J. CONTROL*, vol. 43, no. 6, pp. 1631–1651, 1986.

[73] J. Y. Hung and R. M. Nelms, "Using a boundary layer technique to reduce chatter in sliding mode controllers," in *Proceedings of 6th Annual IEEE Applied Power Electronics Conference, Dallas, TX*, pp. 195–201. 1991.

[74] H. M. Chen, J. C. Renn, and J. P. Su, "Sliding mode control with varying boundary layers for an electro-hydraulic position servo system," *International Journal of Advanced Manufacturing Technology*, vol. 26, no. 1-2, pp. 117–123, 2005.

[75] N. L. Azad, A. Khajepour, and J. McPhee, "Analysis of jackknifing in articulated steer vehicles," in *Proceedings of IEEE Vehicle Power and Propulsion (VPP) Conference, Chicago, Illinois, USA*, pp. 216–220. 2005.

Appendix A

Entries of Matrix A for 3-DOF Model

Entries of matrix $\mathbf{A}$ can be found by using the following equation:

$$\mathbf{A} = -\mathbf{M}^{-1}\mathbf{C} \tag{A.1}$$

where the entries of $\mathbf{M}$ and $\mathbf{C}$ are as follows:

$\mathbf{M}(1,1) = m_1 + m_2$

$\mathbf{M}(1,2) = -m_2(b+c)$

$\mathbf{M}(1,3) = m_2 c$

$\mathbf{M}(1,4) = 0$

$\mathbf{M}(2,1) = -bm_2$

$\mathbf{M}(2,2) = I_1 + m_2 b^2 + m_2 bc$

$\mathbf{M}(2,3) = -m_2 bc$

$\mathbf{M}(2,4) = 0$

$\mathbf{M}(3,1) = -m_2 c$

$\mathbf{M}(3,2) = I_2 + m_2 c^2 + m_2 bc$

$\mathbf{M}(3,3) = -(I_2 + m_2 c^2)$

$\mathbf{M}(3,4) = 0$

$\mathbf{M}(4,1) = 0$

$\mathbf{M}(4,2) = 0$

$\mathbf{M}(4,3) = 0$

$\mathbf{M}(4,4) = 1$

$\mathbf{C}(1,1) = \frac{N_1 C_{\alpha 1} + N_2 C_{\alpha 2}}{u}$

$\mathbf{C}(1,2) = \frac{N_1 C_{\alpha 1} a - N_2 C_{\alpha 2} b - N_2 C_{\alpha 2}(c+d)}{u} + (m_1 + m_2)u$

$\mathbf{C}(1,3) = \frac{N_2 C_{\alpha 2}(c+d)}{u}$

$\mathbf{C}(1,4) = N_2 C_{\alpha 2}$

$\mathbf{C}(2,1) = \frac{N_1 C_{\alpha 1} a - N_2 C_{\alpha 2} b - N_1 C_{M\alpha 1}}{u}$

$\mathbf{C}(2,2) = \frac{N_1 C_{\alpha 1} a^2 + N_2 C_{\alpha 2} b^2 + N_2 C_{\alpha 2}(c+d)b - N_1 C_{M\alpha 1} a}{u} - m_2 b u$

$\mathbf{C}(2,3) = C_R - \frac{N_2 C_{\alpha 2}(c+d)b}{u}$

$\mathbf{C}(2,4) = K_R - N_2 C_{\alpha 2} b$

$\mathbf{C}(3,1) = \frac{-N_2 C_{\alpha 2}(c+d) - N_2 C_{M\alpha 2}}{u}$

$\mathbf{C}(3,2) = \frac{N_2 C_{\alpha 2}(c+d)b + N_2 C_{\alpha 2}(c+d)^2 + N_2 C_{M\alpha 2}(b+c+d)}{u} - m_2 c u$

$\mathbf{C}(3,3) = -C_R - \frac{N_2 C_{\alpha 2}(c+d)^2 + N_2 C_{M\alpha 2}(c+d)}{u}$

$\mathbf{C}(3,4) = -N_2 C_{\alpha 2}(c+d) - K_R - N_2 C_{M\alpha 2}$

$\mathbf{C}(4,1) = 0$

$\mathbf{C}(4,2) = 0$

$\mathbf{C}(4,3) = -1$

$\mathbf{C}(4,4) = 0$

In the above entries:

$$C_{\alpha 1} = \frac{C_{\alpha f}}{N_1} \tag{A.2}$$

$$C_{\alpha 2} = \frac{C_{\alpha r}}{N_2} \tag{A.3}$$

$$C_{M\alpha 1} = \frac{C_{Tf}}{N_1} \tag{A.4}$$

$$C_{M\alpha 2} = \frac{C_{Tr}}{N_2} \tag{A.5}$$

Appendix B

Entries of Matrix A for 5-DOF Model

Entries of matrix $\mathbf{A}$ can be found by using the following equation:

$$\mathbf{A} = -\mathbf{M}^{-1}\mathbf{C} \tag{B.1}$$

where the entries of $\mathbf{M}$ and $\mathbf{C}$ are as follows:

$\mathbf{M}(1,1) = m_1 + m_2$

$\mathbf{M}(1,2) = -m_2(b + c)$

$\mathbf{M}(1,3) = m_2 c$

$\mathbf{M}(1,4) = 0$

$\mathbf{M}(2,1) = -bm_2$

$\mathbf{M}(2,2) = I_1 + m_2 b^2 + m_2 bc$

$\mathbf{M}(2,3) = -m_2 bc$

$\mathbf{M}(2,4) = 0$

$\mathbf{M}(3,1) = -m_2 c$

$\mathbf{M}(3,2) = I_2 + m_2 c^2 + m_2 bc$

$\mathbf{M}(3,3) = -(I_2 + m_2 c^2)$

$\mathbf{M}(3,4) = 0$

$\mathbf{M}(4,1) = 0$

$\mathbf{M}(4,2) = 0$

$\mathbf{M}(4,3) = 0$

$\mathbf{M}(4,4) = 1$

$\mathbf{C}(1,1) = \frac{N_1 C_{\alpha 1} + N_2 C_{\alpha 2}}{u}$

$\mathbf{C}(1,2) = \frac{N_1 C_{\alpha 1} a - N_2 C_{\alpha 2} b - N_2 C_{\alpha 2}(c+d)}{u} + (m_1 + m_2)u$

$\mathbf{C}(1,3) = \frac{N_2 C_{\alpha 2}(c+d)}{u}$

$\mathbf{C}(1,4) = N_2 C_{\alpha 2}$

$\mathbf{C}(2,1) = \frac{N_1 C_{\alpha 1} a - N_2 C_{\alpha 2} b - N_1 C_{M\alpha 1}}{u}$

$\mathbf{C}(2,2) = \frac{N_1 C_{\alpha 1} a^2 + N_2 C_{\alpha 2} b^2 + N_2 C_{\alpha 2}(c+d)b - N_1 C_{M\alpha 1} a}{u} - m_2 bu + \frac{N_1 C_{F1} w_t^2}{2u}$

$\mathbf{C}(2,3) = C_R - \frac{N_2 C_{\alpha 2}(c+d)b}{u}$

$\mathbf{C}(2,4) = K_R - N_2 C_{\alpha 2} b$

$\mathbf{C}(3,1) = \frac{-N_2 C_{\alpha 2}(c+d) - N_2 C_{M\alpha 2}}{u}$

$\mathbf{C}(3,2) = \frac{N_2 C_{\alpha 2}(c+d)b + N_2 C_{\alpha 2}(c+d)^2 + N_2 C_{M\alpha 2}(b+c+d)}{u} - m_2 cu + \frac{N_2 C_{F2} w_t^2}{2u}$

$\mathbf{C}(3,3) = -C_R - \frac{N_2 C_{\alpha 2}(c+d)^2 + N_2 C_{M\alpha 2}(c+d)}{u} - \frac{N_2 C_{F2} w_t^2}{2u}$

$\mathbf{C}(3,4) = -N_2 C_{\alpha 2}(c+d) - K_R - N_2 C_{M\alpha 2}$

$\mathbf{C}(4,1) = 0$

$\mathbf{C}(4,2) = 0$

$\mathbf{C}(4,3) = -1$

$\mathbf{C}(4,4) = 0$

In the above entries:

$$C_{\alpha 1} = \frac{C_{\alpha f}}{N_1} \tag{B.2}$$

$$C_{\alpha 2} = \frac{C_{\alpha r}}{N_2} \tag{B.3}$$

$$C_{M\alpha 1} = \frac{C_{Tf}}{N_1} \tag{B.4}$$

$$C_{M\alpha 2} = \frac{C_{Tr}}{N_2} \tag{B.5}$$

$$C_{F1} = \frac{2C_{sf}}{N_1} \tag{B.6}$$

$$C_{F2} = \frac{2C_{sr}}{N_2} \tag{B.7}$$

Appendix C

Entries of Matrix A for 4-DOF Model

Entries of matrix $\mathbf{A}$ can be found by using the following equation:

$$\mathbf{A} = -\mathbf{M}^{-1}\mathbf{C} \tag{C.1}$$

where the entries of $\mathbf{M}$ and $\mathbf{C}$ are as follows:

$\mathbf{M}(i,j) = 0$, $(i,j = 1 \text{ to } 6)$, except for:

$\mathbf{M}(1,1) = m_1 + m_2 + m_3$

$\mathbf{M}(1,2) = -m_2(b+c) - m_3(b+c+d+e+f)$

$\mathbf{M}(1,3) = m_2 c + m_3(c+d+e+f)$

$\mathbf{M}(1,4) = m_3 f$

$\mathbf{M}(2,1) = -b(m_2 + m_3)$

$\mathbf{M}(2,2) = I_1 + (m_2 + m_3)b^2 + m_2 bc + m_3 b(c+d+e+f)$

$\mathbf{M}(2,3) = -m_2 bc - m_3 b(c+d+e+f)$

$\mathbf{M}(2,4) = -m_3 bf$

$\mathbf{M}(3,1) = -m_2 c - m_3(c+d+e)$

$\mathbf{M}(3,2) = I_2 + m_2 c^2 + m_2 bc + m_3(c+d+e)^2 + m_3(c+d+e)(b+f)$

$\mathbf{M}(3,3) = -[I_2 + m_2 c^2 + m_3(c+d+e)^2] - m_3(c+d+e)f$

$\mathbf{M}(3,4) = -m_3(c+d+e)f$

168

$$\mathbf{M}(4,1) = -m_3 f$$

$$\mathbf{M}(4,2) = I_3 + m_3 f^2 + m_3 b f + m_3 (c+d+e) f$$

$$\mathbf{M}(4,3) = -[I_3 + m_3 f^2 + m_3 (c+d+e) f]$$

$$\mathbf{M}(4,4) = -[I_3 + m_3 f^2]$$

$$\mathbf{M}(5,5) = 1$$

$$\mathbf{M}(6,6) = 1$$

$\mathbf{C}(i,j) = 0$, $(i, j = 1 \text{ to } 6)$, except for

$$\mathbf{C}(1,1) = \frac{N_1 C_{\alpha 1} + N_2 C_{\alpha 2} + \mu N_3}{u}$$

$$\mathbf{C}(1,2) = \frac{N_1 C_{\alpha 1} a - N_2 C_{\alpha 2} b - N_2 C_{\alpha 2}(c+d) - \mu N_3 (b+c+d+e+f+h)}{u} + (m_1 + m_2 + m_3) u$$

$$\mathbf{C}(1,3) = \frac{N_2 C_{\alpha 2}(c+d) + \mu N_3 (c+d+e+f+h)}{u}$$

$$\mathbf{C}(1,4) = \frac{\mu N_3 (f+h)}{u}$$

$$\mathbf{C}(1,5) = N_2 C_{\alpha 2}$$

$$\mathbf{C}(2,1) = \frac{N_1 C_{\alpha 1} a - N_2 C_{\alpha 2} b - \mu N_3 b - N_1 C_{M\alpha 1}}{u}$$

$$\mathbf{C}(2,2) = \frac{N_1 C_{\alpha 1} a^2 + N_2 C_{\alpha 2} b^2 + N_2 C_{\alpha 2}(c+d) b + \mu N_3 b (b+c+d+e+f+h) - N_1 C_{M\alpha 1} a}{u} - (m_2 + m_3) b u$$

$$\mathbf{C}(2,3) = C_R - \frac{N_2 C_{\alpha 2}(c+d) b + \mu N_3 b (c+d+e+f+h)}{u}$$

$$\mathbf{C}(2,4) = -\frac{\mu N_3 b (f+h)}{u}$$

$$\mathbf{C}(2,5) = K_R - N_2 C_{\alpha 2} b$$

$$\mathbf{C}(3,1) = \frac{-N_2 C_{\alpha 2}(c+d) - N_2 C_{M\alpha 2} - \mu N_3 (c+d+e)}{u}$$

$$\mathbf{C}(3,2) = \frac{N_2 C_{\alpha 2}(c+d) b + N_2 C_{\alpha 2}(c+d)^2 + N_2 C_{M\alpha 2}(b+c+d) + \mu N_3 (c+d+e)(b+c+d+e+f+h)}{u} - [m_2 c + m_3 (c+d+e)] u$$

$$\mathbf{C}(3,3) = -C_R - \frac{N_2 C_{\alpha 2}(c+d)^2 + N_2 C_{M\alpha 2}(c+d) + \mu N_3 (c+d+e)(c+d+e+f+h)}{u}$$

$$\mathbf{C}(3,4) = C_g - \frac{\mu N_3 (c+d+e)(f+h)}{u}$$

$$\mathbf{C}(3,5) = -N_2 C_{\alpha 2}(c+d) - K_R - N_2 C_{M\alpha 2} - \mu N_3 (c+d+e+f+h)$$

$$\mathbf{C}(4,1) = -\frac{\mu N_3 (f+h)}{u}$$

$$\mathbf{C}(4,2) = \frac{\mu N_3 (f+h)(b+c+d+e+f+h)}{u} - m_3 f u$$

$$\mathbf{C}(4,3) = -\frac{\mu N_3 (f+h)(c+d+e+f+h)}{u}$$

$$\mathbf{C}(4,4) = -\frac{\mu N_3 (f+h)^2}{u} - C_g$$

$$\mathbf{C}(4,5) = -\mu N_3 (f+h)$$

$$\mathbf{C}(4,6) = -\mu N_3 (f+h)$$

$$\mathbf{C}(5,3) = -1$$

$\mathbf{C}(6, 4) = -1$

In the above entries:

$$C_{\alpha 1} = \frac{C_{\alpha f}}{N_1} \tag{C.2}$$

$$C_{\alpha 2} = \frac{C_{\alpha r}}{N_2} \tag{C.3}$$

$$C_{M\alpha 1} = \frac{C_{Tf}}{N_1} \tag{C.4}$$

$$C_{M\alpha 2} = \frac{C_{Tr}}{N_2} \tag{C.5}$$

Appendix D

Entries of Matrices A and B for Modified 3-DOF Model

Entries of matrix $\mathbf{A}$ can be found by using the following equation:

$$\mathbf{A} = -\mathbf{M}^{-1}\mathbf{C} \tag{D.1}$$

Also, entries of matrix $\mathbf{B}$ can be found by using the following equation:

$$\mathbf{B} = \mathbf{M}^{-1}\mathbf{W} \tag{D.2}$$

where the entries of $\mathbf{M}$, $\mathbf{C}$ and $\mathbf{W}$ are as follows:

$\mathbf{M}(1,1) = m_1 + m_2$

$\mathbf{M}(1,2) = -m_2(b+c)$

$\mathbf{M}(1,3) = m_2 c$

$\mathbf{M}(1,4) = 0$

$\mathbf{M}(1,5) = 0$

$\mathbf{M}(2,1) = -bm_2$

$\mathbf{M}(2,2) = I_1 + m_2 b^2 + m_2 bc$

$\mathbf{M}(2,3) = -m_2 bc$

$\mathbf{M}(2,4) = 0$

$\mathbf{M}(2,5) = 0$

$\mathbf{M}(3,1) = -m_2 c$

$\mathbf{M}(3,2) = I_2 + m_2 c^2 + m_2 bc$

$\mathbf{M}(3,3) = -(I_2 + m_2 c^2)$

$\mathbf{M}(3,4) = 0$

$\mathbf{M}(3,5) = 0$

$\mathbf{M}(4,1) = 0$

$\mathbf{M}(4,2) = 0$

$\mathbf{M}(4,3) = 0$

$\mathbf{M}(4,4) = 1$

$\mathbf{M}(4,5) = 0$

$\mathbf{M}(5,1) = 0$

$\mathbf{M}(5,2) = 0$

$\mathbf{M}(5,3) = 0$

$\mathbf{M}(5,4) = \frac{A_e d_j}{K_q}$

$\mathbf{M}(5,5) = \frac{V_t}{4K_q}$

$\mathbf{C}(1,1) = \frac{N_1 C_{\alpha 1} + N_2 C_{\alpha 2}}{u}$

$\mathbf{C}(1,2) = \frac{N_1 C_{\alpha 1} a - N_2 C_{\alpha 2} b - N_2 C_{\alpha 2}(c+d)}{u} + (m_1 + m_2)u$

$\mathbf{C}(1,3) = \frac{N_2 C_{\alpha 2}(c+d)}{u}$

$\mathbf{C}(1,4) = N_2 C_{\alpha 2}$

$\mathbf{C}(1,5) = 0$

$\mathbf{C}(2,1) = \frac{N_1 C_{\alpha 1} a - N_2 C_{\alpha 2} b - N_1 C_{M\alpha 1}}{u}$

$\mathbf{C}(2,2) = \frac{N_1 C_{\alpha 1} a^2 + N_2 C_{\alpha 2} b^2 + N_2 C_{\alpha 2}(c+d)b - N_1 C_{M\alpha 1} a}{u} - m_2 bu$

$\mathbf{C}(2,3) = C_R - \frac{N_2 C_{\alpha 2}(c+d)b}{u}$

$\mathbf{C}(2,4) = -N_2 C_{\alpha 2} b$

$\mathbf{C}(2,5) = -A_e d_j \beta_e$

$\mathbf{C}(3,1) = \frac{-N_2 C_{\alpha 2}(c+d) - N_2 C_{M\alpha 2}}{u}$

$\mathbf{C}(3,2) = \frac{N_2 C_{\alpha 2}(c+d)b + N_2 C_{\alpha 2}(c+d)^2 + N_2 C_{M\alpha 2}(b+c+d)}{u} - m_2 cu$

$\mathbf{C}(3,3) = -C_R - \frac{N_2 C_{\alpha 2}(c+d)^2 + N_2 C_{M\alpha 2}(c+d)}{u}$

$\mathbf{C}(3,4) = -N_2 C_{\alpha 2}(c+d) - N_2 C_{M\alpha 2}$

$\mathbf{C}(3,5) = A_e d_j \beta_e$

$\mathbf{C}(4,1) = 0$

$\mathbf{C}(4,2) = 0$

$\mathbf{C}(4,3) = -1$

$\mathbf{C}(4,4) = 0$

$\mathbf{C}(4,5) = 0$

$\mathbf{C}(5,1) = 0$

$\mathbf{C}(5,2) = 0$

$\mathbf{C}(5,3) = 0$

$\mathbf{C}(5,4) = 0$

$\mathbf{C}(5,5) = \frac{\beta_e K_e}{K_q}$

$\mathbf{W}(1,1) = 0$

$\mathbf{W}(2,1) = 0$

$\mathbf{W}(3,1) = 0$

$\mathbf{W}(4,1) = 0$

$\mathbf{W}(5,1) = x_v$

In the above entries:

$$C_{\alpha 1} = \frac{C_{\alpha f}}{N_1} \tag{D.3}$$

$$C_{\alpha 2} = \frac{C_{\alpha r}}{N_2} \tag{D.4}$$

$$C_{M\alpha 1} = \frac{C_{Tf}}{N_1} \tag{D.5}$$

$$C_{M\alpha 2} = \frac{C_{Tr}}{N_2} \tag{D.6}$$

Appendix E

Entries of Matrices A and B for 7-DOF Model

Entries of matrix $\mathbf{A}$ can be found by using the following equation:

$$\mathbf{A} = -\mathbf{M}^{-1}\mathbf{C} \qquad \text{(E.1)}$$

Also, entries of matrix $\mathbf{B}$ can be found by using the following equation:

$$\mathbf{B} = \mathbf{M}^{-1}\mathbf{W} \qquad \text{(E.2)}$$

where the entries of $\mathbf{M}$, $\mathbf{C}$ and $\mathbf{W}$ are as follows:

$\mathbf{M}(1,1) = m_1 + m_2$

$\mathbf{M}(1,2) = -m_2(b + c)$

$\mathbf{M}(1,3) = m_2 c$

$\mathbf{M}(1,4) = 0$

$\mathbf{M}(1,5) = 0$

$\mathbf{M}(1,6) = 0$

$\mathbf{M}(2,1) = -bm_2$

$\mathbf{M}(2,2) = I_1 + m_2 b^2 + m_2 bc$

$\mathbf{M}(2,3) = -m_2 bc$

$\mathbf{M}(2,4) = 0$

$\mathbf{M}(2,5) = 0$

$\mathbf{M}(2,6) = 0$

$\mathbf{M}(3,1) = -m_2c$

$\mathbf{M}(3,2) = I_2 + m_2c^2 + m_2bc$

$\mathbf{M}(3,3) = -(I_2 + m_2c^2)$

$\mathbf{M}(3,4) = 0$

$\mathbf{M}(3,5) = 0$

$\mathbf{M}(3,6) = 0$

$\mathbf{M}(4,1) = 0$

$\mathbf{M}(4,2) = 0$

$\mathbf{M}(4,3) = 0$

$\mathbf{M}(4,4) = 1$

$\mathbf{M}(4,5) = 0$

$\mathbf{M}(4,6) = 0$

$\mathbf{M}(5,1) = 0$

$\mathbf{M}(5,2) = 0$

$\mathbf{M}(5,3) = 0$

$\mathbf{M}(5,4) = 0$

$\mathbf{M}(5,5) = I_e$

$\mathbf{M}(5,6) = 0$

$\mathbf{M}(6,1) = 0$

$\mathbf{M}(6,2) = 0$

$\mathbf{M}(6,3) = 0$

$\mathbf{M}(6,4) = 0$

$\mathbf{M}(6,5) = 0$

$\mathbf{M}(6,6) = I_e$

$\mathbf{C}(1,1) = \frac{N_1 C_{\alpha 1} + N_2 C_{\alpha 2}}{u}$

$\mathbf{C}(1,2) = \frac{N_1 C_{\alpha 1} a - N_2 C_{\alpha 2} b - N_2 C_{\alpha 2}(c+d)}{u} + (m_1 + m_2)u$

$\mathbf{C}(1,3) = \frac{N_2 C_{\alpha 2}(c+d)}{u}$

175

$\mathbf{C}(1,4) = N_2 C_{\alpha 2}$

$\mathbf{C}(1,5) = 0$

$\mathbf{C}(1,6) = 0$

$\mathbf{C}(2,1) = \frac{N_1 C_{\alpha 1} a - N_2 C_{\alpha 2} b - N_1 C_{M\alpha 1}}{u}$

$\mathbf{C}(2,2) = \frac{N_1 C_{\alpha 1} a^2 + N_2 C_{\alpha 2} b^2 + N_2 C_{\alpha 2}(c+d)b - N_1 C_{M\alpha 1} a}{u} - m_2 b u + \frac{N_1 C_{F1} w_t^2}{2u}$

$\mathbf{C}(2,3) = C_R - \frac{N_2 C_{\alpha 2}(c+d)b}{u}$

$\mathbf{C}(2,4) = K_R - N_2 C_{\alpha 2} b$

$\mathbf{C}(2,5) = \frac{N_1 C_{F1} r_e w_t}{2u}$

$\mathbf{C}(2,6) = 0$

$\mathbf{C}(3,1) = \frac{-N_2 C_{\alpha 2}(c+d) - N_2 C_{M\alpha 2}}{u}$

$\mathbf{C}(3,2) = \frac{N_2 C_{\alpha 2}(c+d)b + N_2 C_{\alpha 2}(c+d)^2 + N_2 C_{M\alpha 2}(b+c+d)}{u} - m_2 c u + \frac{N_2 C_{F2} w_t^2}{2u}$

$\mathbf{C}(3,3) = -C_R - \frac{N_2 C_{\alpha 2}(c+d)^2 + N_2 C_{M\alpha 2}(c+d)}{u} - \frac{N_2 C_{F2} w_t^2}{2u}$

$\mathbf{C}(3,4) = -N_2 C_{\alpha 2}(c+d) - K_R - N_2 C_{M\alpha 2}$

$\mathbf{C}(3,5) = 0$

$\mathbf{C}(3,6) = \frac{N_2 C_{F2} r_e w_t}{2u}$

$\mathbf{C}(4,1) = 0$

$\mathbf{C}(4,2) = 0$

$\mathbf{C}(4,3) = -1$

$\mathbf{C}(4,4) = 0$

$\mathbf{C}(4,5) = 0$

$\mathbf{C}(4,6) = 0$

$\mathbf{C}(5,1) = 0$

$\mathbf{C}(5,2) = \frac{N_1 C_{F1} w_t r_e}{u}$

$\mathbf{C}(5,3) = 0$

$\mathbf{C}(5,4) = 0$

$\mathbf{C}(5,5) = \frac{N_1 C_{F1} r_e^2}{u}$

$\mathbf{C}(5,6) = 0$

$\mathbf{C}(6,1) = 0$

$\mathbf{C}(6,2) = \frac{N_2 C_{F2} w_t r_e}{u}$

$\mathbf{C}(6,3) = -\frac{N_2 C_{F2} w_t r_e}{u}$

$\mathbf{C}(6,4) = 0$

$\mathbf{C}(6,5) = 0$

$\mathbf{C}(6,6) = \frac{N_2 C_{F2} r_e^2}{u}$

$\mathbf{W}(1,1) = 0$

$\mathbf{W}(2,1) = 0$

$\mathbf{W}(3,1) = 0$

$\mathbf{W}(4,1) = 0$

$\mathbf{W}(5,1) = 0$

For torque vectoring device $\mathbf{W}(6,1) = 2$, and for differential braking $\mathbf{W}(6,1) = 1$.

In the above entries:

$$C_{\alpha 1} = \frac{C_{\alpha f}}{N_1} \tag{E.3}$$

$$C_{\alpha 2} = \frac{C_{\alpha r}}{N_2} \tag{E.4}$$

$$C_{M\alpha 1} = \frac{C_{Tf}}{N_1} \tag{E.5}$$

$$C_{M\alpha 2} = \frac{C_{Tr}}{N_2} \tag{E.6}$$

$$C_{F1} = \frac{2C_{sf}}{N_1} \tag{E.7}$$

$$C_{F2} = \frac{2C_{sr}}{N_2} \tag{E.8}$$